

A numerical study on the distortion of
magnetotelluric data from topography, near-surface
conductors and basins

Thesis submitted in accordance with the requirements of the University of Adelaide for
an Honours Degree in Geophysics.

Dennis Conway

November 2013



THE UNIVERSITY
of ADELAIDE

ABSTRACT

Magnetotelluric (MT) data may be distorted by a variety of structures, including near-surface inhomogeneities, topographic gradients and large conductive bodies. A synthetic study is undertaken to analyse these three factors in the Curnamona Province, South Australia. Firstly, the effect of topography in the northern Flinders Ranges is investigated by the use of forward models. The results show both a galvanic and an inductive distortion concentrated at high topographic gradients. The effect of near-surface conductors is also investigated with forward models, using data from Lake Frome as input. The models show a small area of galvanic distortion around the circumference of the lake, but no regional effect. These results are compared with distortion analyses of real data. Finally, thin-sheet modelling is used to determine the effect of a synthetically calculated conductance using data from the eastern Arrowie Basin. Results from the thin-sheet model show that the Arrowie Basin has the potential to inductively distort MT data on a regional scale. Using this result as motivation, two three-dimensional (3-D) inversions are undertaken on the Geoscience Australia "08GA-C1 MT" line; one incorporating the Arrowie Basin as a prior model and the other starting from a homogeneous half-space. The results of these inversions are overlain with interpretations from seismic data collected along the same line. The best agreement between the seismic and MT data is achieved with the prior-model inversion, supporting the hypothesis that basin scale conductivity structures distorts MT data and showing that this effect is alleviated by incorporating basin structure as a prior model during inversion.

KEYWORDS

Distortion, magnetotellurics, Curnamona Province, synthetic, topography, modelling

Table of Contents

Introduction	8
Theory	10
Synthetic studies	14
Background	14
Topography	16
Methods	16
Results	18
Near-surface conductors	21
Methods	21
Results	23
Basinal distortion	23
Methods	23
Results	29
Comparison to real data	29
Background	29
Methods	31
Results	34
Discussion	37
Topography	37
Near-surface conductors	38
Basinal distortion	41
Conclusion	42

A numerical study on the distortion of magnetotelluric data	5
Acknowledgements	43
References	43
Appendix: Model fit plots	47

List of Figures

1.	Map of the Curnamona Province	15
2.	Topographic map of the northern Flinders Ranges	18
3.	Results of topographic distortion modelling	19
4.	Input model used for modelling near-surface conductors	22
5.	Results of near-surface conductor modelling	24
6.	Depth to basement and conductance map	28
7.	Thin-sheet model results	30
8.	Station locations for 08GA-C1 MT line	32
9.	Mesh used for inversions	33
10.	WALDIM plot for 08GA-C1 MT line	35
11.	Inversions results	36

List of Tables

1.	Classification scheme for the WALDIM code.	14
2.	Basal model used in the thin-sheet forward model.	29
3.	Site locations for the 08GA-C1 MT line.	31

INTRODUCTION

In recent years magnetotelluric (MT) surveys have become an attractive option for deep mineral exploration due to the large penetration depth of the method (Tuncer et al., 2006; Farquharson & Craven, 2009). One of the major problems facing interpreters of MT data, however, is the effect of distortions on measured MT data by both local and regional structures (Garcia et al., 2003). Distortions may be broadly classified as either galvanic (frequency independent) or inductive (frequency dependent). Galvanic distortion is most commonly caused by near-surface heterogeneities, which cause charge accumulations at conductivity boundaries (Chave & Smith, 1994). On the other hand, inductive distortion is sourced from larger, deeper structures which are outside the spatial constraints of the survey (Lezaeta, 2003). The identification and removal of both of these distortions is essential for quality interpretations of MT data.

Galvanic distortion can be detected in MT data using dimensionality analysis tools, (e.g. Martí et al., 2009). Once identified, the distortion may either be removed in the processing stage, or accommodated for during modelling. The handling of galvanic distortion is fairly well understood when one-dimensional (1-D) or 2-D regional conductivity structures are present, with several established methods for its identification and removal (Groom & Bailey, 1991; Agarwal & Weaver, 2000; McNeice & Jones, 2001; Caldwell et al., 2004). The analysis becomes more difficult when 3-D structures are present as there are too many undetermined variables to retrieve the undistorted response (Utada et al., 2000). The best results in distorting settings with a 3-D conductivity structure have been realised by the simultaneous inversion of the impedance tensor and the electric distortion tensor (Miensopust et al., 2013). This idea was first proposed by (DeGroot-Hedlin, 1995) for dealing with 2-D data, and codes have been developed independently by Avdeeva et al. (2012) and Miensopust et al. (2013) for 3-D inversions. Another

method is to allow near-surface heterogeneities in the inversion model to accommodate for distortion, as suggested by Patro & Egbert (2011).

Inductive distortion of MT data is a much less discussed issue, with the majority of research focussing on distortion from coast effects. The early history of coast effects in land-side MT surveys is described in (Parkinson & Jones, 1979). Qualitative analysis of coast effects was undertaken by Santos & Nolasco (2001), who reported, using synthetic models, distortions to the impedance tensor for periods >100 s. These distortions are a result of the inductive coupling between the conductive ocean and resistive ocean floor (Key & Constable, 2011).

A final distorting factor to be considered is the effect of topography. Topography has the effect of concentrating fields into valleys and dispersing them at topographic highs (Fox et al., 1980). Nam et al. (2008) have shown that for a 3-D topographic anomaly there will be both galvanic and inductive distortions in any polarisation. They have also shown that galvanic topographic effects are more significant than inductive effects, and act to lower apparent resistivities, whereas inductive distortions increase apparent resistivities. Topographic effects are most significant for areas with a high topographic gradient (Fox et al., 1980), and the inductive effect is most prominent when the height of the topography is comparable to the skin-depth of the signal (Baba et al., 2013).

This thesis seeks to quantify these distortions by using synthetic models based on features in the Curnamona Province. Topographic effects from the nearby Flinders Ranges are first considered, followed by the impact of near-surface conductors (the playa lake, Lake Frome) and finally the effect of the conductive basins which flank the survey line is investigated. These results are compared with data collected along the Geoscience Australia 08GA-C1 MT line. Motivated by the synthetic results, a 3-D inversion of the profile line is undertaken using constraints from the synthetic studies, and a comparison is given between a constrained and unconstrained inversion.

THEORY

The magnetotelluric method is a passive technique, which involves the measurement of the Earth's time varying electromagnetic (EM) fields (Simpson & Bahr, 2005). These fields are sourced from naturally occurring processes, and propagate through the Earth diffusively (Chave & Jones, 2012). The electric and magnetic fields are both measured in two orthogonal directions, x and y , which lie in the plane of the Earth's surface, and an additional measurement of the magnetic field may be taken in the z direction. These measurements are made over a wide range of periods (T). The reciprocal of period is frequency (f or ω for angular frequency) which is also commonly used. Typical crustal surveys collect data from between 0.001 s and 1000 s.

At each of these periods the impedance tensor (\mathbf{Z}) is calculated. The impedance tensor relates the measured electric (\mathbf{E}) and magnetic flux (\mathbf{B}) fields in the frequency (ω) domain. \mathbf{Z} is a 2×2 complex valued matrix which satisfies the equation

$$\begin{pmatrix} E_x \\ E_y \end{pmatrix} = \begin{pmatrix} Z_{xx} & Z_{xy} \\ Z_{yx} & Z_{yy} \end{pmatrix} \begin{pmatrix} H_x \\ H_y \end{pmatrix}, \quad (1)$$

where E_i ($i \in x, y$) is the electric field in the i -th direction, each Z_{ij} is a component of \mathbf{Z} and H_i is the i -th component of \mathbf{H} , the magnetic field strength (Chave & Jones, 2012). \mathbf{H} is related to \mathbf{B} by the equation

$$\mathbf{H} = \frac{\mathbf{B}}{\mu}, \quad (2)$$

where μ is the magnetic permeability of the medium holding the magnetic field, commonly assumed to be equal to the permeability of free space, μ_0 . The interpretation of \mathbf{Z} is given in the following sections.

Due to the orthogonality of electric and magnetic fields in EM waves, the measured fields may be decoupled into two components (Simpson & Bahr, 2005). The \mathbf{E} and \mathbf{B} -

fields in one polarisation are perpendicular to the \mathbf{E} and \mathbf{B} -fields in the other polarisation. For a general case we arbitrarily assign these as the Z_{xy} and Z_{yx} polarisations. In this paper the Z_{xy} polarisation refers to a north-south polarisation of the \mathbf{E} -field. For a 1-D Earth the Z_{yx} and Z_{xy} elements are equal in magnitude and opposite in sign, and the Z_{xx} and Z_{yy} elements will be zero. For a 2-D Earth the MT data may be rotated parallel to the geoelectric strike, such that Z_{xx} and Z_{yy} equal zero. In this case the elements Z_{xy} and Z_{yx} are independent of each other and the Z_{xy} and Z_{yx} polarisations are called the transverse electric (TE) and transverse magnetic (TM) modes, respectively. For a 3-D Earth all elements in \mathbf{Z} are generally non-zero (Simpson & Bahr, 2005).

The impedance tensor represents how Earth's conductivity structure has altered the source fields. Conductivity (σ) and its reciprocal, resistivity (ρ), are measures of the ability of a material to conduct an electric current: a high conductivity indicates that a material is a good conductor of electric currents.

The apparent resistivity (ρ_a) can be calculated from \mathbf{Z} . It is interpreted as the resistivity of an equivalent uniform half space down to the signal's penetration depth. It can be calculated (Chave & Jones, 2012) in both the Z_{xy} and Z_{yx} polarisations via the equation

$$\rho_{a_{ij}} = \frac{|Z_{ij}|^2}{\mu\omega}. \quad (3)$$

Another quantity that we can extract from the impedance tensor is the impedance phase (ϕ) of the signal. The impedance phase measures the phase shift between the electric and magnetic fields, which is 45° for a uniform Earth. For a 1-D layered Earth we can interpret a phase angle above 45° to indicate that the EM-response is penetrating into a medium of higher conductivity, and conversely a phase angle below 45° to indicate the penetration into a medium of lower conductivity (Chave & Jones, 2012). Similar

to apparent resistivity, we can calculate a phase angle for both the Z_{xy} and Z_{yx} modes. These are given by the equation

$$\phi_{ij} = \tan^{-1} \left(\frac{\Im(Z_{ij})}{\Re(Z_{ij})} \right) \quad i, j \in \{x, y\}, \quad (4)$$

where \Re and \Im denote the real and imaginary parts of Z_{ij} , respectively (Simpson & Bahr, 2005).

Another important equation in the analysis of MT data is the skin depth equation. The skin depth (δ) of a period is defined as the depth at which the MT signal is attenuated to e^{-1} of its original value. It is approximated as

$$\delta \approx 500 \sqrt{\rho_a T}, \quad (5)$$

where T is in seconds, apparent resistivity is in Ωm and the resultant δ is in metres (Simpson & Bahr, 2005).

Other parameters which can be extracted of the impedance tensor include anisotropy and skew, both of which include information about the dimensionality of the Earth structure being sounded. The skew (S) is defined by the relation

$$S = \frac{|Z_{xx} + Z_{yy}|}{|Z_{xy} - Z_{yx}|}, \quad (6)$$

and is a measure of the EM coupling between the measured electric and magnetic fields (Naidu, 2012). The skew angle (θ_S), is defined as

$$\theta_S = \tan^{-1}(S). \quad (7)$$

For 1-D and 2-D structures, θ_S will be zero (this is not usually the case due to errors), and for 3-D structures values for the skew angle are typically greater than 3° .

Anisotropy (λ) is a measure of the degree of preferential flow may be defined in various ways. For this thesis the definition of

$$\lambda = \frac{\max \{\rho_{xy}, \rho_{yx}\}}{\min \{\rho_{xy}, \rho_{yx}\}}, \quad (8)$$

has been taken (Heise & Pous, 2003). A λ value of unity is expected for isotropic media, with values greater than 3 being considered large. As discussed in the introduction, MT measurements can be prone to distortions. In the case of galvanic distortion, we can try to quantify distortion to \mathbf{Z} by the introduction of a real, 2×2 distortion tensor, \mathbf{C} . The impedance tensor that we calculate from measurements (\mathbf{Z}_m) is a product of \mathbf{C} and the regional impedance tensor (\mathbf{Z}_r), i.e.

$$\mathbf{Z}_m = \mathbf{C} \cdot \mathbf{Z}_r. \quad (9)$$

This equation shows that for a 1-D and 2-D regional geology, where Z_{xx} and Z_{yy} are zero, the distortion will only affect ρ_a . The phase angle will be unaffected, as the real and imaginary parts of Z_{xy} and Z_{yx} are scaled by the same factor. For a 3-D regional geology, both the phase and apparent resistivity curves will be affected by galvanic distortion due to the non-zero Z_{xx} and Z_{yy} components (Ledo et al., 1998).

The distortion tensor may be factorised as the product

$$\mathbf{C} = g(\mathbf{T} \cdot \mathbf{S} \cdot \mathbf{A}), \quad (10)$$

where g is a scalar and the tensor factors \mathbf{T} , \mathbf{S} and \mathbf{A} are the twist, shear and anisotropy tensors, respectively (Groom & Bailey, 1989). Writing the factorised form of \mathbf{C} is useful as it elucidates the variables which contribute to galvanic distortion.

One of the methods for detecting galvanic distortion in real data is using the WALDIM code of Martí et al. (2009). This code is based on the work of Weaver et al. (2000) and

Martí et al. (2005) in determining dimensionality using the rotational invariants of the MT tensor. At each period, the code classifies the geoelectric dimensionality into one of seven groups. These groups are listed in Table 1.

As discussed in the Introduction, there are many different methods for dealing with the distortion in MT data, including inversion, approximation and calculation from a secondary dataset.

SYNTHETIC STUDIES

Background

The three synthetic studies which follow have been made using data from the Curnamona Province as a guideline. The Curnamona Province, shown in Figure 1, is a Proterozoic province which straddles the boundary between South Australia and New South Wales. The basement of the Curnamona Province is composed of Palaeoproterozoic metasedimentary and metavolcanic units as well as Mesoproterozoic granites and mafic intrusives (Fabris et al., 2009). These are overlain by younger sediments, the most extensive of which occur in the Moorowie and Yalkalpo sub-basins (Wade et al., 2012). In particular the Moorowie Sub-basin obscures part of the Benagerie Ridge Volcanics

Table 1: Classification scheme for the WALDIM code.

Type	Dimensionality	Distortion
1	1-D	none
2	2-D	none
3	2-D	twist only
4	2-D	general
5	3-D	indeterminable
6	2-D	diagonal regional tensor
7	2-D or 1-D	general

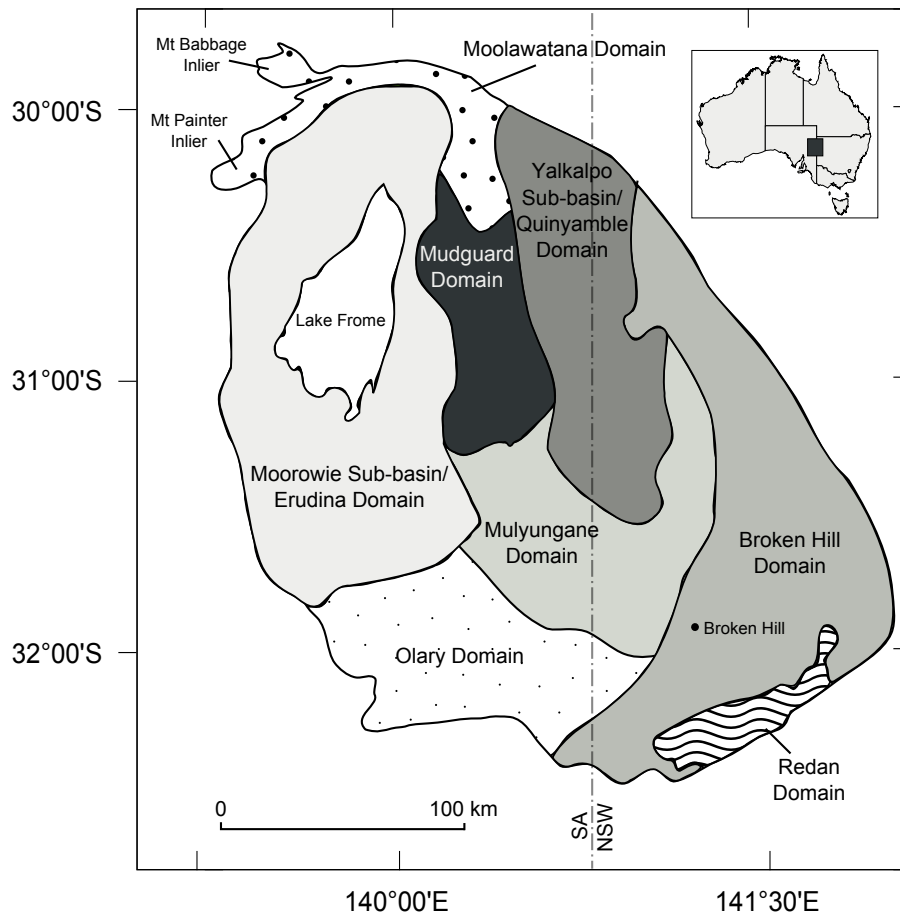


Figure 1: Map of the Curnamona Province, adapted from Conor & Preiss (2008). The map shows the 7 domains of Proterozoic basement that form the Curnamona Province. Also included are the Moorowie and Yalkalpo sub-basins, which cover the Erudina and Quinyamble domains, respectively. The landscape feature, Lake Frome, is also present. Inset: map of Australia showing location of the Curnamona Province (black box).

(BVR), a unit of economic interest which forms much of the Mudguard Domain (Wade et al., 2012). In addition to the mineral interests in the Curnamona Province, the region is also prospective for geothermal energy (Milligan & Lilley, 2010).

The first synthetic model is based on the eastern Arrowie Basin, which is the combination of the Moorowie and Yalkalpo sub-basins, shown in Figure 1. The Arrowie Basin is a rift basin which formed during the Cambrian period, controlled by Neoproterozoic and Cambrian rift structures and early Paleozoic and Tertiary reactivated basement

structures (Teasdale et al., 2001). A central basement ridge, shown in Figure 1 as the Mudguard Province, separates the two sub-basins.

The second model is based on the northern Flinders Ranges, which is where the most significant topography in the Curnamona Province occurs. The relief of the Flinders Ranges (usually above 300 m, but with peaks exceeding 1100 m) is primarily resultant of Plio-Quaternary tectonism (Teasdale et al., 2001). This has led to the exposure of the Proterozoic Mt Painter and Mt Babbage inliers (see Figure 1). The northern parts of the ranges are also composed of Adelaidean sediments (Quigley et al., 2006).

The third model area is the Lake Frome region, shown in Figure 1. Lake Frome is a playa lake which lies roughly 50 km east of the Flinders Ranges. Throughout Lake Frome's history its two main water sources have been tropically derived flood-waters and temperate westerlies (Cohen et al., 2011). The playa conditions at Lake Frome have been dominant from 5 ka to present day, with the exception of a short-lived lake-filling episode during the Medieval Climatic Anomaly (Cohen et al., 2011). The high salinity in Lake Frome has led to much higher conductivities when compared to the surrounding regolith, which can be seen in results of the 2010 Frome airborne electromagnetic (AEM) survey (Roach, 2012).

The motivation in choosing these three areas lies in the fact they are, respectively, the best examples of basins, topography and near-surface conductors in the Curnamona Province. These are the three distorting factors to be analysed in this study, and their locality allows for a convenient comparison with MT data collected in the Curnamona.

Topography

METHODS

To quantify the effects of topography on MT data, the 3-D forward modelling code of Mackie et al. (1994) is implemented. The Mackie et al. (1994) code is a finite differ-

ence algorithm which is based on the minimum residual relaxation method. An Earth resistivity structure in three dimensions is used as an input for the code. This requires l maps in the z -direction which specify $\rho(x, y)$ on an m by n grid.

An algorithm was created to convert digital elevation model (DEM) data, gridded as $E(x, y)$ on a regular grid, into a Mackie et al. (1994) compatible input file. At each layer a check was made on every point on the $E(x, y)$ grid. If the DEM value was greater than the height layer, the $\rho(x, y)$ value was assigned a resistivity of $100 \Omega m$. If else, the $\rho(x, y)$ was specified as air. This algorithm maps the $E(x, y)$ into a Mackie et al. (1994) compatible grid, subject to the discretisation into l layers. A trade-off between the dimensions of l , m and n must be made, as due to the limitations of the code the maximum number of grid cells is restricted by

$$(l + a) \times m \times n \approx 360000, \quad (11)$$

where a is the number of air layers ($a \approx 10$).

The Mackie et al. (1994) code can be run at a number of frequencies. In the output file, the E_x , E_y , H_x and H_y values are available for each frequency at each node in both the Z_{xy} and Z_{yx} polarisations. Thus, the full impedance tensor, \mathbf{Z} , may be calculated from equation 1 at each of the two polarisations.

For this study, a region of 1.25° latitude by 1.25° longitude in the northern Flinders Ranges has been selected for topography distortion analysis. The data were selected from the 9 arc second DEM data supplied by Geoscience Australia (Hutchinson et al., 2009). A grid of $75 \times 75 \times 53$ nodes was chosen as the dimensional extent of the model. This satisfies equation 11, and allows vertical layer l to have a thickness of 20 m, which is sufficiently small that the major topographic structures remain unaliased. A map of the 9 arc second DEM data, regridded onto 75×75 nodes, is shown in Figure 2.

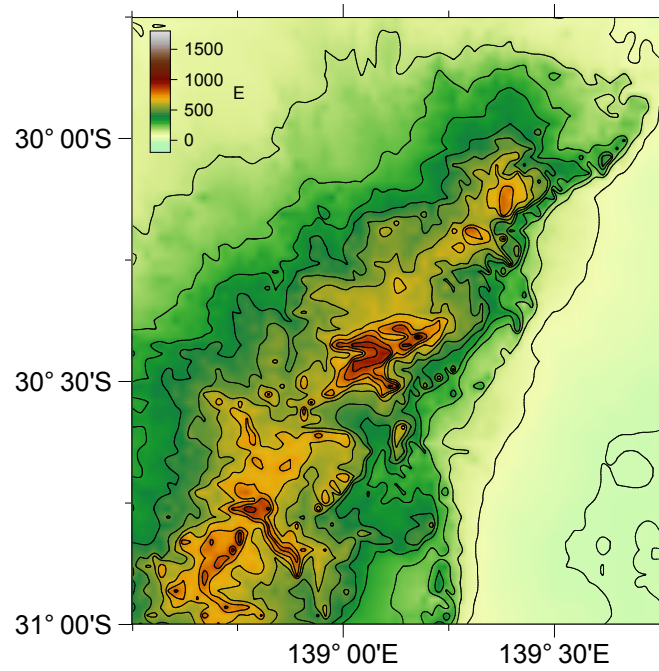


Figure 2: Topographic map of the northern Flinders Ranges, showing the input for the forward models. Overlain on the topographic data are topography contours (grey lines) spaced at 80 m. The actual topography model values are discretised into 20 m intervals during processing, which is 4 times more detailed than the 80 m contours shown in this map. No extra padding has been added.

A forward model was run on the resultant grid, including a basal model of a homogeneous $100 \Omega\text{m}$ half-space, using the Mackie et al. (1994) code. The code was run for periods of 0.1 s, 1 s, 10 s and 100 s, so that the effect of topography could be studied over a large range of periods. The apparent resistivity and phase angles of the model were calculated from the relations in equation 3 and equation 4.

RESULTS

The apparent resistivity and phase angle plots (Figure 3) show the effect of topography at periods of 0.1 s, 1 s, 10 s and 100 s.

The phase angle plots show that at 0.1 s the topography induces a change in the phase angle of $\pm 3^\circ$. Positive phase angle shifts (red) occur at topographic peaks, and negative

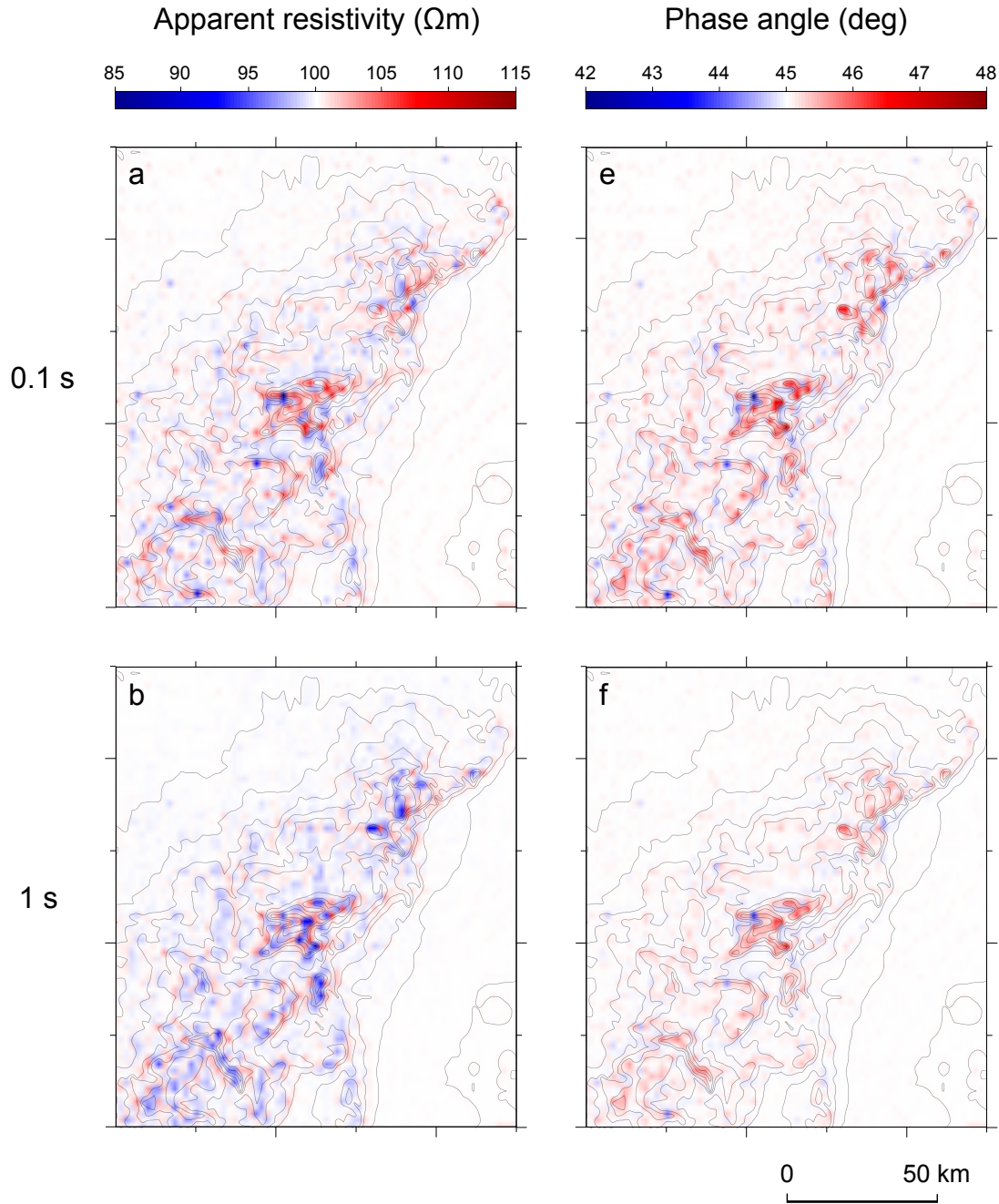


Figure 3: Results of the topographic distortion modelling. These show the Z_{xy} apparent resistivity (a-d) and phase angle (e-h) that would be measured at each point on the 75×75 grid due to topography alone. Each row of maps represents the response at different periods. Topographic contours have been overlain on the data to show the relationship between topographic gradient and the MT response. These are spaced at 80 m. Absolute values of the contours have been omitted for clarity. These may be found in Figure 2. Continued next page.

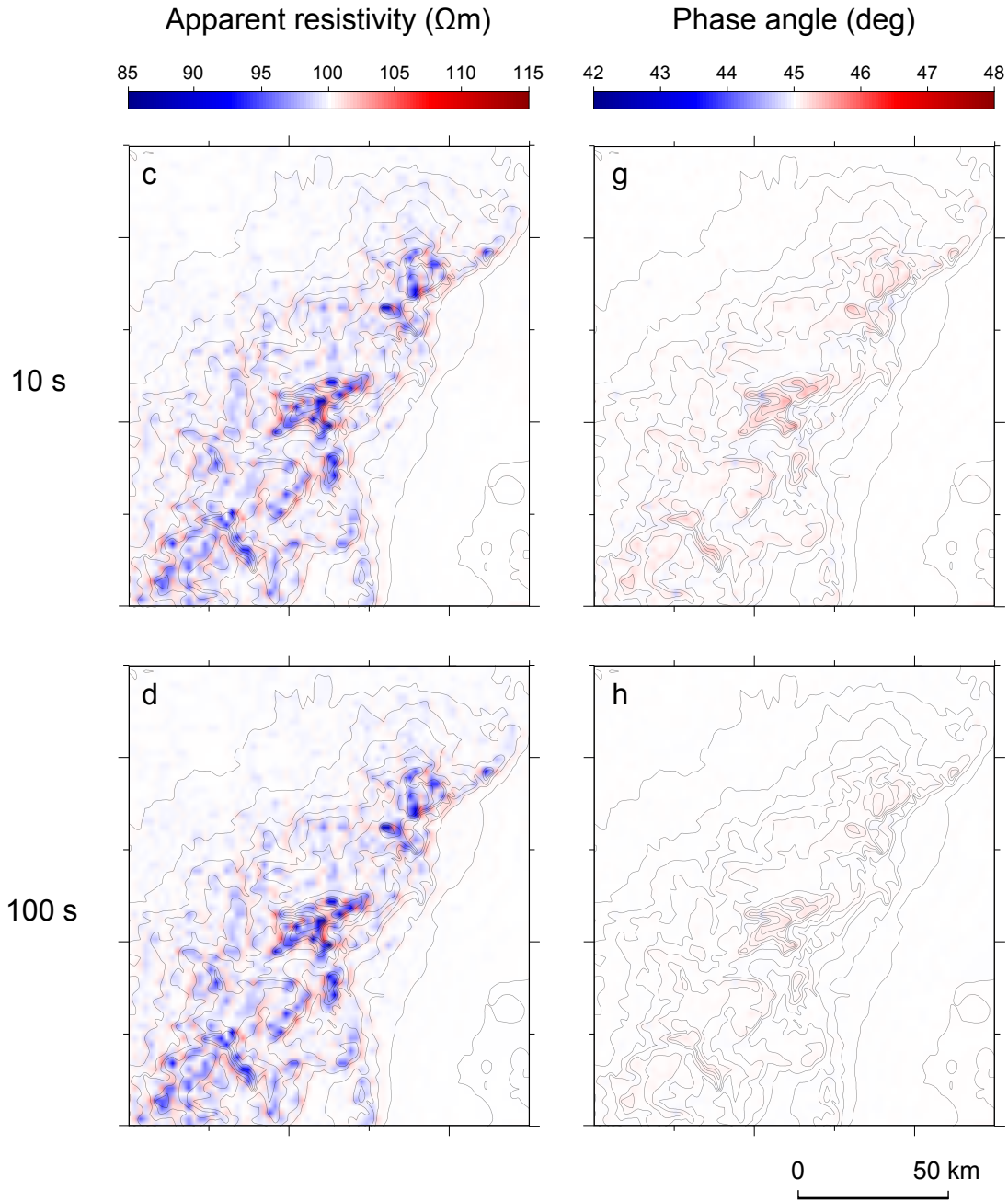


Figure 3: Continued from previous page. In the absence of topographic distortion a resistivity of $100 \Omega\text{m}$ and a phase angle of 45° is expected. For this reason these values are coloured white, with red and blue representing higher and lower than values, respectively. For reference, typical resistivity errors are 5% for resistivity and 2° for phase. The maps are geolocated in the same positions as Figure 2.

phase shifts (blue) occur in valleys. At 1 s the change in phase angle is below typical error values and by 100 s the inductive effects of topography have almost completely vanished.

The apparent resistivity plots show a similar period dependence. At 0.1 s, the change in apparent resistivity from the 100 Ωm background is predominately positive. At 1 s the change is mostly negative. The apparent resistivity maps for 10 s and 100 s are almost identical to the 1 s map. At all periods there are changes in the apparent resistivity of up to 15% at high gradients, which is higher than typical errors of 3-10%. There is no regional effect of topography on apparent resistivity.

Near-surface conductors

METHODS

The effects of near-surface conductors can be investigated by similar methods (utilising the 3-D code of Mackie et al. (1994) and DEM data) to those described in the topography modelling section. The current section focuses on near-surface conductors, e.g. the salty playa lakes of arid Australia (see Deckker, 1983), which are characterised by topographic lows relative to the surrounding area. Therefore, the algorithm described for topographic modelling changes such that a check is now made to test whether or not elevation ($E(x, y)$) is above or below some constant k (k will be dependent on the baseline topography in the area). If $E(x, y)$ is less than k , a low resistivity (ρ_l) is assigned to that point on the grid, and if else, a high resistivity (ρ_h) is assigned. This method produces a single conductivity layer of thickness l_c with a binary resistivity map. The remainder of the method is identical to the method described in the topography modelling section.

For this study, topographic data were extracted from 9-arc-second DEM data supplied by Geoscience Australia (Hutchinson et al., 2009) in an area of 1.5° by 1.5° centred on Lake Frome. The data were resampled to 150×150 points. For the algorithm above, a

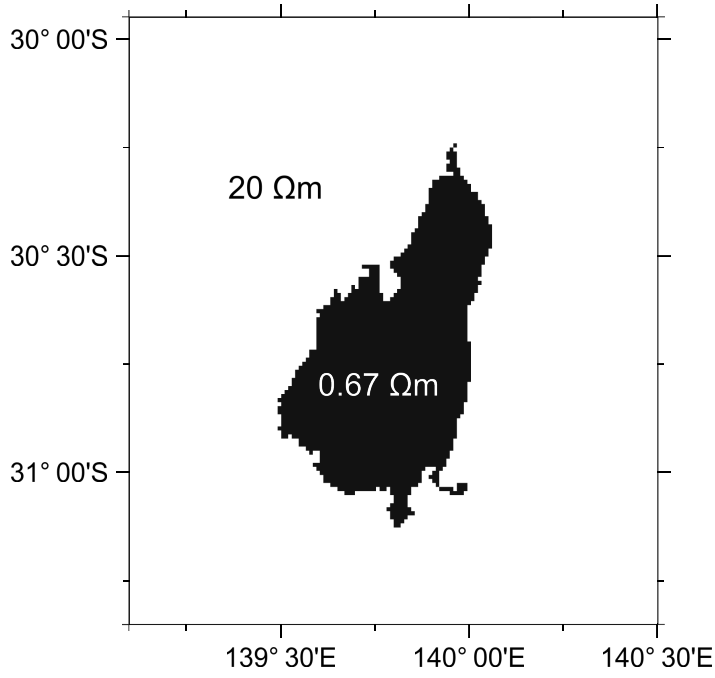


Figure 4: The input model used in the modelling of near-surface conductors. This slice extends from 0-60 m, with the remainder of the model being a 1000 km 100 Ωm half-space. There is no extra padding.

value of 4 m was given for k , which most accurately mapped Lake Frome when compared with satellite imagery. Manual edits were made to the map produced by this method to make Lake Frome a homogeneous body (there are several islands in Lake Frome which lie above the 4 m boundary – these are conductive due to a high gypsum concentration (Ullman & McLeod, 1986)). The resistivities ρ_l and ρ_h were chosen as 0.67 Ωm and 20 Ωm , respectively. The thickness (l_c) of the layer was 60 m. These three values were motivated by analysis of the Frome AEM survey (e.g. Roach, 2012). The input model is shown in Figure 4.

A forward model was run on the grid using the 3-D forward code of Mackie et al. (1994). A homogeneous basal model of 20 Ωm was specified down to 1000 km, such that any observed effects could be attributed solely to the conductivity structure. The model was run at periods of 0.1 s, 1 s, 10 s and 100 s.

RESULTS

The results for the apparent resistivity and phase calculations in the Z_{xy} polarisation are given in Figure 5.

At all periods there is a small region of elevated apparent resistivity surrounding Lake Frome. This has a thickness of 1 pixel (roughly equal to 1 km). The structure of this halo is period independent. At 0.1 s there is a small regional drop in apparent resistivity ($0.05 \Omega\text{m}$). This is not present at the other periods. There are different regional apparent resistivity structures at periods of 1 s, 10 s and 100 s, however. These structures have a small effect on the apparent resistivity ($\pm 0.05 \Omega\text{m}$). In these structures half-loops of continuous apparent resistivity form at the edges of Lake Frome, which close in on themselves at other edge points up to 100 km away.

The phase angle results (Figure 5) show the inductive effects of near-surface conductors. At a period of 0.1 s it is observed that Lake Frome produces a small (0.05°) regional increase change in phase. Larger increases (1°) in phase angle at east-west striking boundaries are also observed. The plots for 1 s, 10 s and 100 s phase data are mostly homogeneous, and do not differ in structure from the input model.

Basinal distortion

METHODS

To investigate the potential for inductive distortion from large basins, the thin-sheet method of McKirdy et al. (1985) is utilised. In this method a thin-sheet of thickness h , which has a local integrated conductance $\tau(x, y)$ at position (x, y) , overlies a layered conductivity structure (Heinson & Lilley, 1993). Although this method obscures any vertical changes in conductivity within the thin-sheet, the effects of any lateral changes in conductivity are well represented (Hermance, 1983). Thin-sheet modelling is particularly

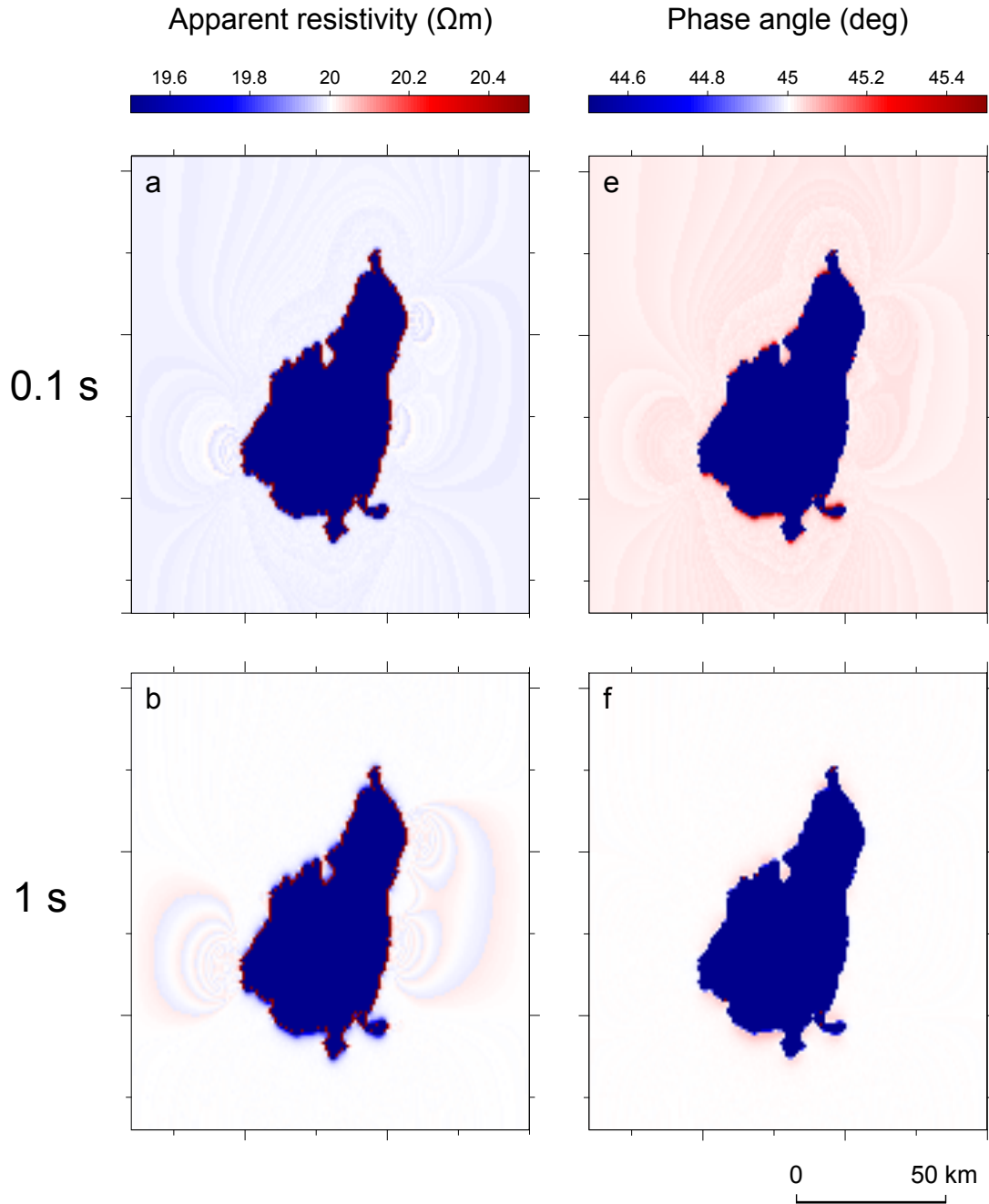


Figure 5: Results of the near-surface conductor modelling. These show the Z_{xy} apparent resistivity (a-d) and phase angle (e-h) that would be measured at each point on the 150×150 grid due to the Lake Frome conductivity anomaly (Figure 4). Each row of maps represents the response at different periods. The plots are geolocated in the same positions as Figure 4. Continued next page.

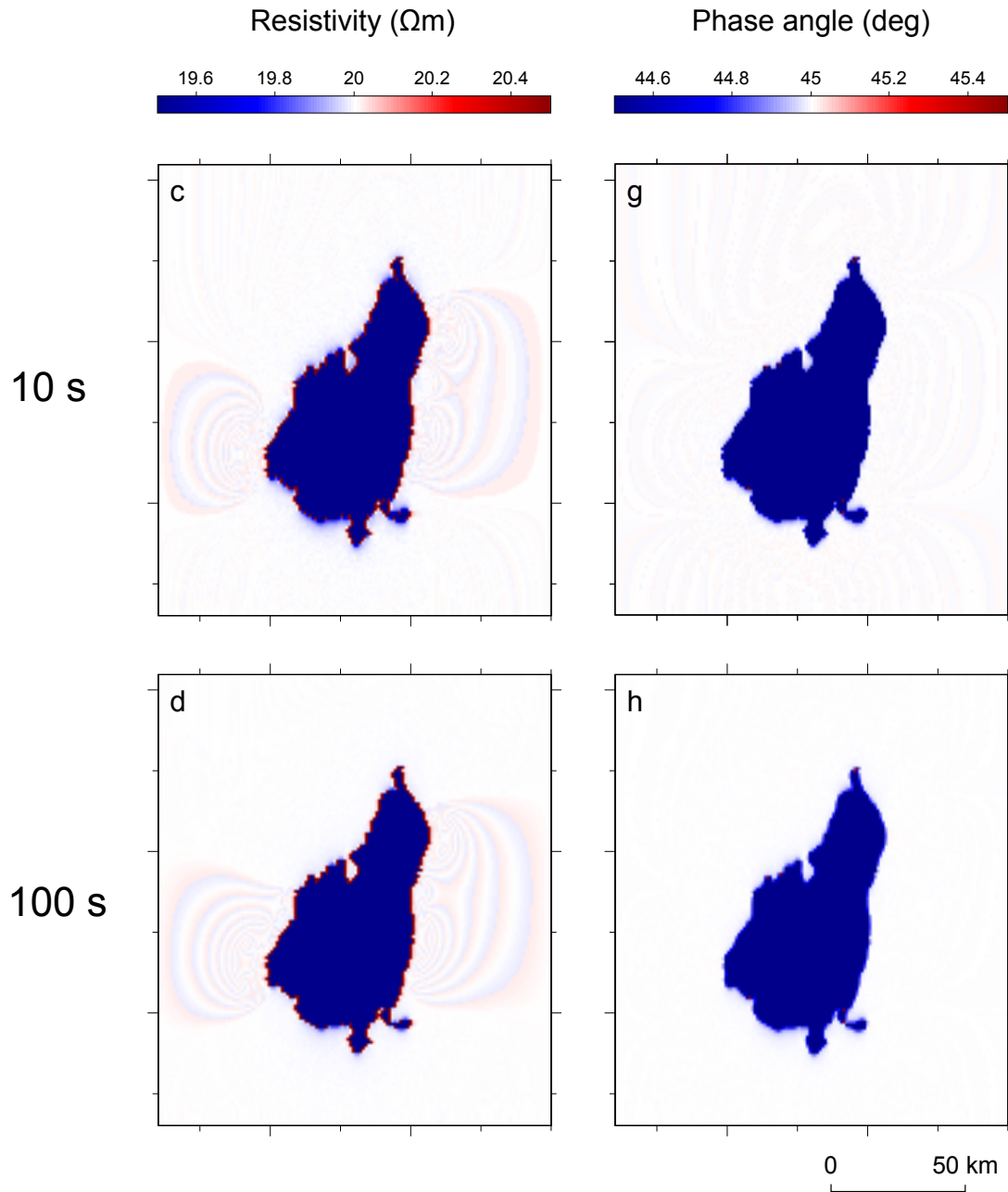


Figure 5: Continued from previous page. Apparent resistivities which differ from 20 Ωm and phase angles which differ from 45° can be attributed to the near-surface conductor. For this reason 20 Ωm and 45° are coloured white, with red and blue representing higher and lower than values, respectively. The dynamic range of the apparent resistivity and phase angle colourbars has been compressed considerably to bring out the regional effect. The apparent resistivity high which surrounds Lake Frome has a period independent resistivity of 70 Ωm . The apparent resistivity and phase angle minimums that occur inside Lake Frome are period dependent, however this effect has been suppressed by the colourbar.

useful for modelling long period responses, as the thin-sheet approximation is valid in the case of $\delta \gg h$.

In order to employ a thin-sheet model, $\tau(x, y)$ must be specified to a depth of h at each point (x, y) in a grid. To this end, a synthetic conductance model is created based on empirical relations between depth and conductivity in a sedimentary environment.

The first step is to take the definition of conductance over a distance (h) in the z direction,

$$\tau(x, y) = \int_0^h \sigma dz, \quad (12)$$

and divide the integral into sedimentary and basement components:

$$\int_0^h \sigma_t dz = \int_0^{d(x,y)} \sigma_s dz + \int_{d(x,y)}^h \sigma_b dz, \quad (13)$$

where the subscripts t , s and b refer to total, sedimentary and basement, respectively, and the variable $d(x, y)$ is the depth to basement. We assume that basement conductivity is constant through all depths. A relation between depth and conductivity is required for the sedimentary section, however. From Archie's Law for porous, water saturated rocks (Mullen & Kellett, 2007) we know that σ_s is related to porosity (φ) and water conductivity (σ_w) by the empirical relation

$$\sigma_s \approx \sigma_w \varphi^m, \quad (14)$$

where m is a shape factor, dependent on the on the shape and connections of the porosity.

In a basinal environment, a primary control on σ_w will be temperature. Temperature increases linearly with the regional geothermal gradient (G) such that the temperature at any depth is given by the product Gz . The conductivity of the pore water can be approximated by

$$\sigma_w \approx 3 + \frac{Gz}{10}, \quad (15)$$

where the units for σ_w , G and z are Sm^{-1} , Km^{-1} and m , respectively (Revil & Cathles, 1998).

Another empirical approximation is made to represent the exponential reduction of porosity with increasing depth:

$$\varphi \approx Ae^{-\lambda z}, \quad (16)$$

where λ is the lithology dependent *compaction factor* and A is a constant related to the initial conductivity (Bahr et al., 2001).

Equations 15 and 16 can now be substituted into equation 14, which, in turn, can be substituted into equation 13 to give

$$\tau(x, y) \approx \int_0^{d(x, y)} \left(3 + \frac{Gz}{10} \right) (Ae^{-\lambda z})^m dz + (h - d)\sigma_b, \quad (17)$$

where the units for τ are S. The integral in equation 17 is not directly solvable in general, with the exception of the case where $m=2$. It can be solved by numerical methods, however. A 2-D map for $\tau(x, y)$ is made over the entire grid by evaluating equation 17. Hence, gridded depth to basement data is required to attain the thin-sheet integrated conductance.

In this study, depth to basement data has been used from the Arrowie SEEBASE (Structurally Enhanced view of Economic Basement) project (Teasdale et al., 2001). The Arrowie SEEBASE project was initiated by Primary Industries and Resources South Australia (PIRSA) in 2001 to give insight into the structure, composition and depth of Proterozoic basement in the Arrowie Basin by making use of pre-existing gravity, magnetic, seismic, well and digital elevation data (Teasdale et al., 2001). From the wider dataset, a section of 1.5° latitude by 1.5° longitude, centred on the eastern Arrowie Basin was extracted. The data were down-sampled to a 200×200 regular grid, a plot of which can be found in Figure 6a.

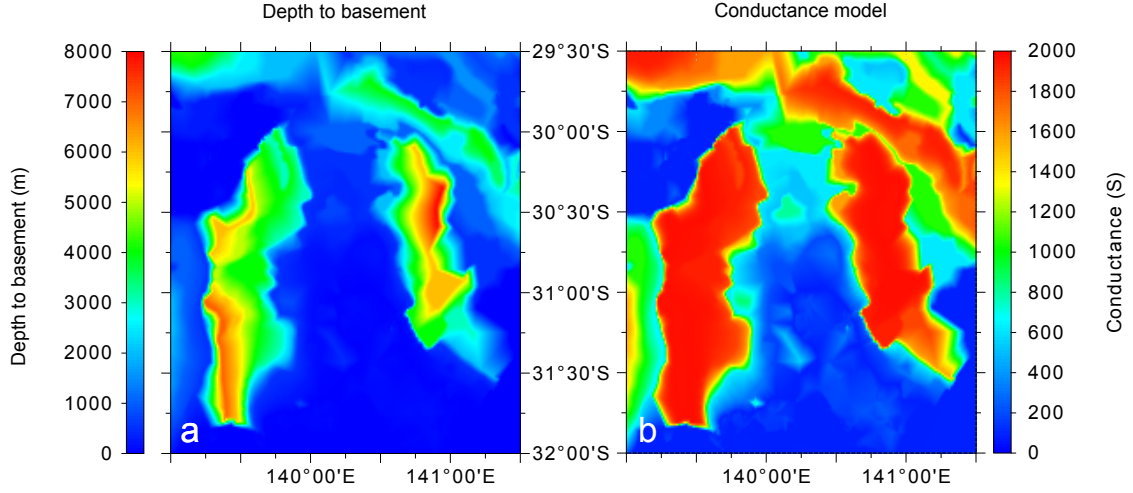


Figure 6: (a) Depth to basement data from the Arrowie SEEBASE project. (b) A synthetically calculated conductance map based on the data in (a).

The depth to basement data were utilised to construct a thin-sheet conductance map of the region, using the methods above. The thickness of the thin-sheet layer (h) was chosen to be 8 km, which is just above the maximum depth to basement in the area. The basement conductivity was chosen as $100 \Omega\text{m}$. Values for the constants m , λ , and A were chosen as 2, 1800 m^{-1} and $0.617 \Omega\text{m}$, respectively, as these values are typical for sandstones (Bahr et al., 2001). Although it is known that there is an unusually high geothermal gradient in the area (Brugger et al., 2005), a relatively normal G value of 30 Kkm^{-1} was chosen to ensure that the final distortion estimates were conservative.

The resultant $\tau(x, y)$ (Figure 6b) was utilised as the thin-sheet layer in the thin-sheet modelling algorithm of McKirdy et al. (1985). Each point on the $\tau(x, y)$ was used as a node. Nodes were spaced at 830 m in the x -direction and 720 m in the y -direction. A layered Earth basal model, given in Table 2, was specified, motivated by the regional lithospheric scale conductivity structures, e.g. Maier et al. (2007). The thin-sheet model was run for periods of 46 s, 100 s and 1000 s.

RESULTS

The results in Figure 7 show the skew angle and anisotropy at periods of 46 s, 100 s and 1000 s due to the conductance of the Arrowie Basin.

At 46 s, the skew angle is relatively low throughout the majority of the area, with high skew angles confined to the edges of the basin. The skew angle is especially high in the areas with low depth to basement which border the basin, such as the Benagerie Ridge and the Flinders Ranges. At 100 s skew angles greater than 5° occur along similar structures, however these areas of high skew angle are larger. At 1000 s the areas of high skew angle have fully developed, and there is a clear high-low duality. A similar phenomenon occurs with the anisotropy results, where at 46 s there is significant anisotropy along the edges of the Arrowie Basin, which further develops at 100 s until the majority of the area displays anisotropy at 1000 s.

COMPARISON TO REAL DATA

Background

In 2008 and 2009 MT data were acquired for Geoscience Australia in the Curnamona province. Broadband data were collected from 25 sites along a 240 km traverse (08GA-C1) which had previously been used to conduct a deep seismic survey. The site locations and names are given in Table 3. The aim of the survey was to image the crustal

Table 2: Basal model used in the thin-sheet forward model.

Depth to bottom (km)	Resistivity (Ωm)
1	1000
100	100
400	20
600	10

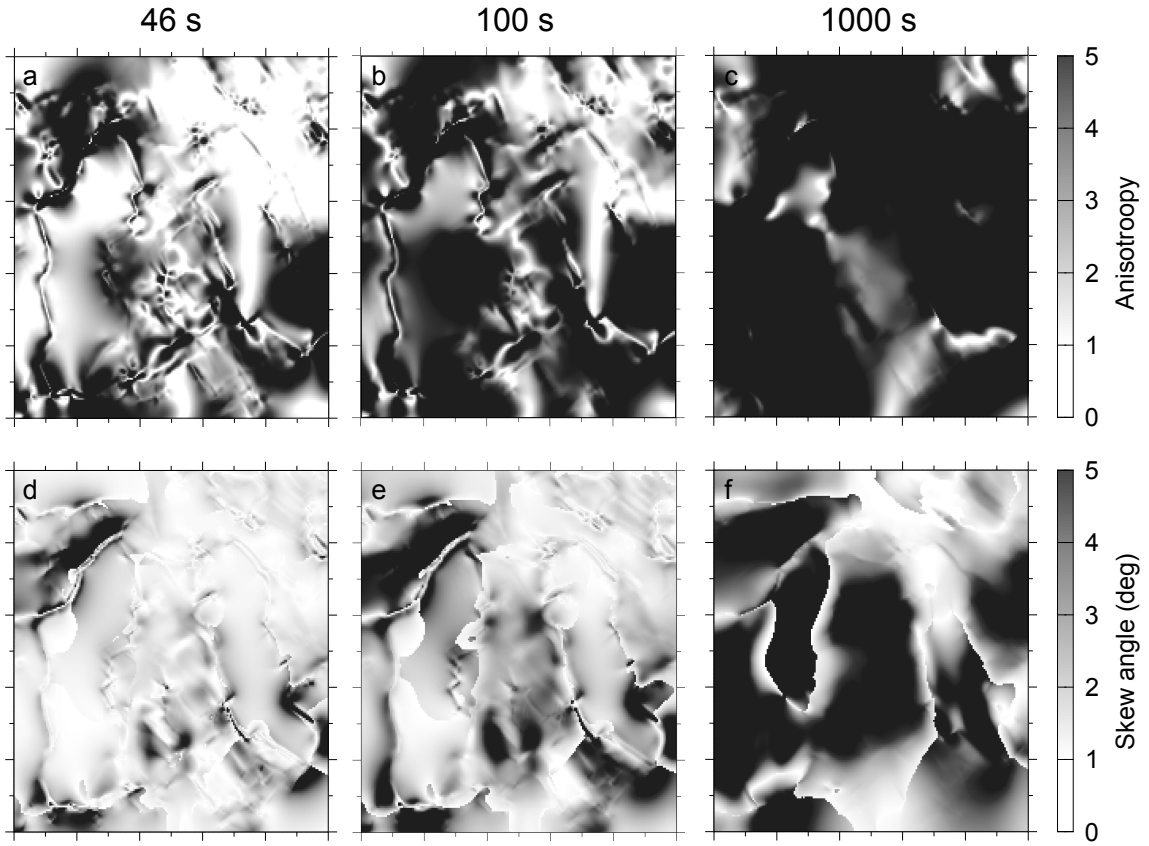


Figure 7: Results of thin-sheet modelling at periods 46 s, 100 s and 1000 s. Anisotropy is shown in (a-c) and the skew angle in (d-f). The colourbars for both anisotropy and the skew angle have been restricted to $\in [0,5]$. The plots have the same geolocation as Figure 6.

architecture of the Curnamona Province, which is an area with uranium and geothermal energy potential (Milligan & Lilley, 2010). A map of the survey area is shown in Figure 8, which also highlights the proximity of the survey to the Arrowie Basin, Flinders Ranges and Lake Frome.

As seen in Figure 8, the MT sites along the 08GA-C1 line are in close proximity to the study areas in the synthetic modelling section. The data from this survey can therefore be used to test the validity of the findings from the synthetic models.

Table 3: Site locations for the 08GA-C1 MT line.

Site number	Longitude	Latitude	Elevation (m)
1	140°19'40.49	-31°43'48.71	137
2	140°17'57.29	-31°38'43.85	117
3	140°15'39.06	-31°33'59.04	98
4	140°15'26.04	-31°28'39.30	83
5	140°15'15.12	-31°23'14.99	67
6	140°15'15.82	-31°17'50.51	47
7	140°15'16.13	-31°12'32.04	33
8	140°16'56.26	-31°07'50.34	32
9	140°15'35.50	-31°03'44.33	34
10	140°12'50.33	-31°00'47.81	23
11	140°12'02.53	-30°56'00.18	22
12	140°10'10.17	-30°50'17.17	27
13	140°09'16.94	-30°45'17.89	22
14	140°08'52.28	-30°40'12.90	37
15	140°06'58.16	-30°35'06.31	21
16	140°07'24.06	-30°30'09.54	23
17	140°07'12.55	-30°25'04.93	14
18	140°04'47.70	-30°20'15.72	19
19	139°57'48.96	-30°10'34.02	2
20	139°56'38.82	-30°07'18.02	14
21	139°53'59.06	-30°02'42.24	34
22	139°49'21.36	-29°59'54.54	46
23	139°45'19.37	-29°55'52.62	72
24	139°41'43.12	-29°52'04.33	104
25	139°35'08.24	-29°50'31.62	115

Methods

To test the results from the topography and near-surface conductor section, WALDIM (Martí et al., 2009) dimensionality analysis is undertaken on the 08GA-C1 MT data. The default WALDIM threshold settings were used, and the resulting dimensionality values (refer to Table 1) are plotted in Figure 10.

To investigate how we can better model off-array distortion in MT data, two inversions of the Curnamona MT line are undertaken using the 3-D inversion code of Siripunvara-

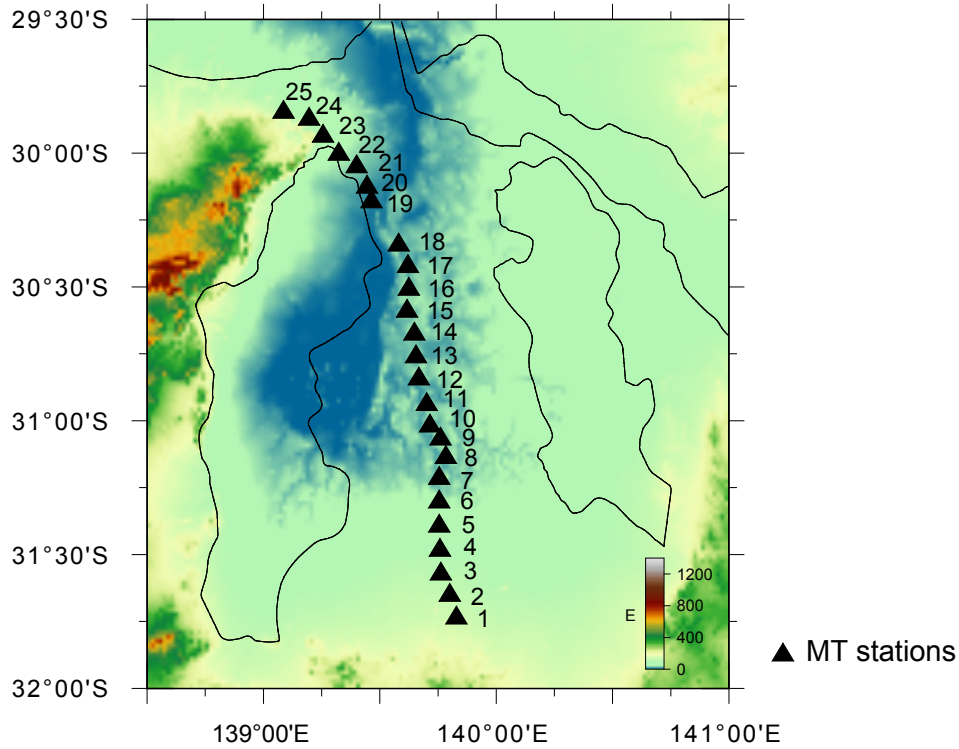


Figure 8: A map showing the Geoscience Australia 08GA-C1 MT line station locations. Overlain is a topographic map of the area, which highlights both the northern Flinders Ranges and Lake Frome. The 2 km depth to basement contour (white line) is included to highlight the proximity of the survey to the Arrowie Basin. This is sourced from the Arrowie SEEBASE project (Teasdale et al., 2001). Note that the northernmost station (Station 25) was not used in the inversion of this data.

porn et al. (2005). The first inversion uses a $100 \Omega\text{m}$ half-space as the starting model, and the second includes a conductive Arrowie Basin as locked information. The Arrowie Basin model (Figure 9) has a resistivity set at $4 \Omega\text{m}$ down to 4 km (at greater depths the porosity is too small to have significant conductivity). Both inversions are made on a $125 \times 32 \times 40$ mesh, which extends 200 km on each side of the line. The mesh is shown in Figure 9. Site 25 has not been included in the inversions, as its deviation from the line would have required a substantially larger mesh and longer computational time.

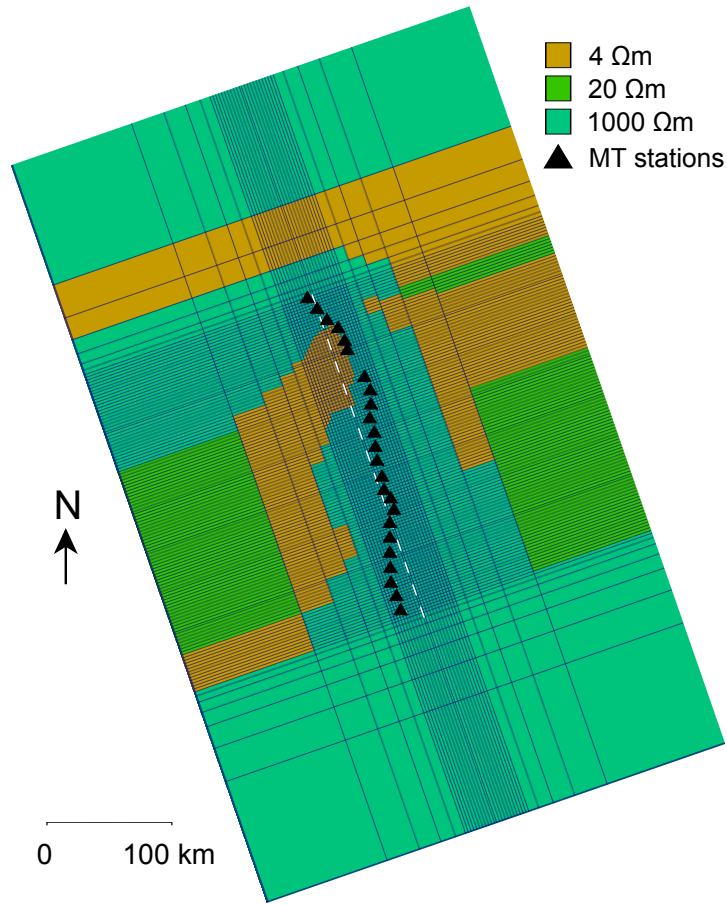


Figure 9: The prior model and mesh for the constrained inversion. This resistivity structure extends to 4 km depth, after which a 100 Ωm homogeneous half-space is used. The unconstrained inversion was made with the same mesh geometry, using a 100 Ωm homogeneous half-space over all depths. The dotted white line represents the slice from which the inversion results were taken.

The inversions were run on the full impedance tensor data using 16 periods over 7 decades. An error floor of 5% was chosen. This forces each measurement to have a minimum error of 5%. The inversions were allowed to run with smoothing parameters $\tau_i = 0.3$ in the x , y and z directions, until the root-mean-square error (RMS) was stable (did not decrease) between iterations. The inversion was restarted with $\tau_i = 0.1$ in all directions until the RMS stabilised. This added more structure into the model. For this second stage, the Arrowie Basin conductivity structure (Figure 9) was allowed to change (the lock was taken off). This was to allow a smoother inversion result.

Once the inversions had been completed, two cross-sections along the line specified in Figure 9 were taken from the final results and compared with deep seismic data taken along the same line (Korsch et al., 2010). This is shown in Figure 11.

Results

The WALDIM dimensionality test results (Figure 10) show the dimensionality and distortion of the MT data at different periods at each site. The green and blue colours represent an undistorted 1-D and 2-D geoelectric strike, the yellow a galvanically distorted 1-D or 2-D geoelectric strike, the red a 3-D geoelectric strike with undetermined distortion and the grey an undetermined dimensionality and distortion. Hence, sites which are dominated by green and blue points (e.g. Site 4 and Site 14) are less affected by galvanic distortion than sites with many yellow points (Site 1, Site 13, Site 25). Sites with many red and grey points (e.g. Site 10, Site 24) are difficult to interpret due to the ambiguity of the distortion in these cases.

The unconstrained (Model 1, Figure 11a) and constrained (Model 2, Figure 11b) inversion results provide two different interpretations of the 08GA-C1 MT data. These two inversions had final RMS values of 2.46 and 2.67, respectively.

There are two main differences between the results in Model 1 and Model 2. The first of these is the magnitude of the conductive structures. The dynamic range of resistivity in Model 1 is much higher than in Model 2, with resistivity varying over 7 orders of magnitude compared to 5. Additionally, there is a much greater distinction between conductive and resistive structures in Model 2. The second main difference is the nature of the conductivity structures which the two inversions have imaged.

At $x=-115$ km there is a conductor present from 10 km to 40 km depth in Model 1 which is absent in Model 2. The conductor appears to terminate at the $z=40$ km seismic boundary, which has been interpreted by (Korsch et al., 2010) as representing

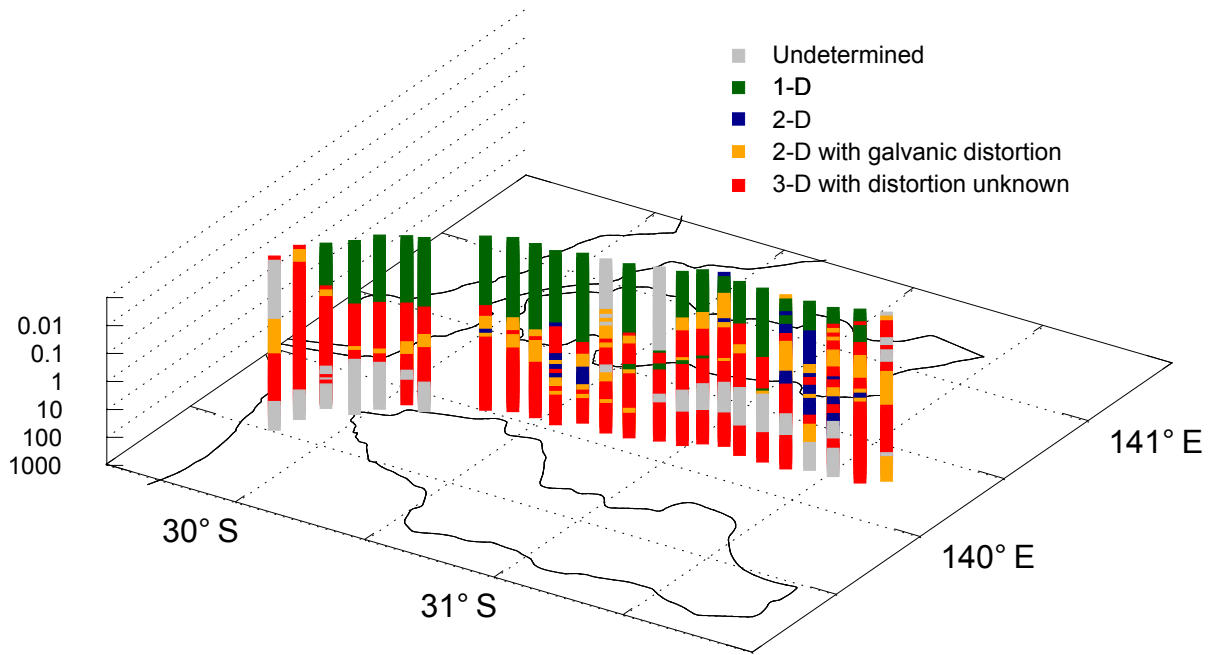


Figure 10: A plot showing the WALDIM dimensionality at each site along the Geoscience Australia 08GA-C1 MT line. The z -axis, period, has a rough correlation to depth. Green corresponds to type 1 in the WALDIM dimensionality test (Table 1), blue to type 2, red to type 5 and yellow to types 3, 4, 6 and 7. The 2 km depth to basement contour (black line) is included for orientation purposes (compare with Figure 8).

the Mohorovičić discontinuity (Moho). This conductor lies outside of the survey line and as such it is relatively unconstrained. Next to this conductor ($x=-105$ km) is a resistive body. Model 1 has this body terminating at the 20 km seismic reflector, and Model 2 has the body terminating at the 30 km seismic reflector. It is difficult to say which is more likely to be correct. Similarly the conductive body at $x=-65$ km reaches further up into the crust in Model 2 compared to Model 1, with the two bodies terminating at $z=20$ km and $z=30$ km respectively.

The two inversions image slightly different conductive structures at $x=-20$ km. Both structures agree fairly well with the seismic interpretation. Similarly, the two inversions both image resistive structures at $x=15$ km which are reasonably comparable.

One of the major differences between the inversions is the conductive body at $x=35$ km. In the constrained inversion this is the largest conductive structure of the profile, extend-

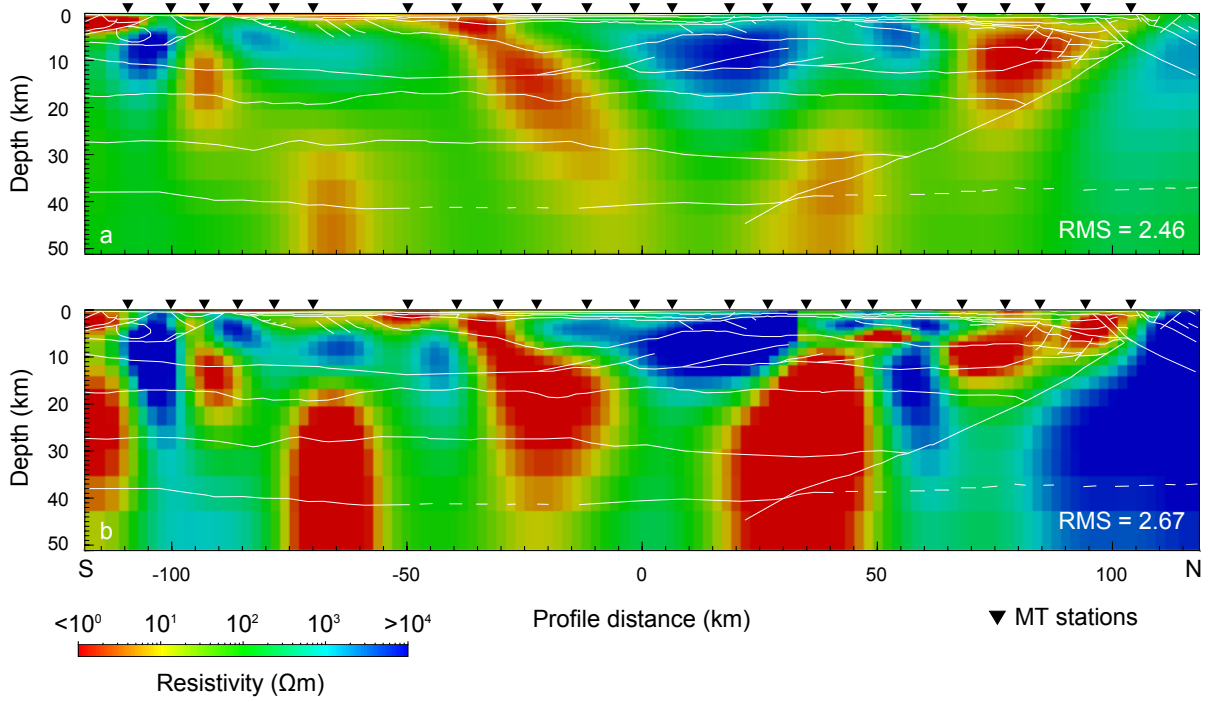


Figure 11: The results of the two inversions. The unconstrained inversion is shown in (a) and the constrained inversion in (b), using the same colourbar. The two slices of the 3-D inversion have been taken along the dotted white line in Figure 9 and clipped to 50 km depth. Overlain on both of the inversions is the seismic interpretation of Korsch et al. (2010) in white. Horizontal and vertical scales are equal.

ing from 10 km depth to below the interpreted Moho. In the unconstrained inversion this is a relatively minor body, which is smaller and more resistive than some of the other conductive structures. Other differences also occur in this region; in the constrained inversion, at $x=55$ km, there is a conductor at 10 km depth, whereas in the unconstrained inversion this is a resistive structure. Neither of these differences are supported one way or the other by comparison with the seismic data.

Further to the north ($x=75$ -100 km) the two inversions offer differing models of the near-surface ($z=0$ -15 km). Whereas this is imaged in Model 1 as a homogeneous conductive body, Model 2 segregates this area into three different conductivity structures. This agrees well with the seismic interpretation.

DISCUSSION

Topography

The results from the topography modelling (Figure 3) show both a galvanic and an inductive distortion.

At a period of 0.1 s a significant shift in phase angle occurs, which is of the same order of magnitude as typical errors in MT data. Positive and negative changes in phase angle are associated with positive and negative topographic gradients, respectively. Phase shifts become gradually less prominent with increase in period. These results indicate that topographic gradients affect the phase angle in MT data, and that this effect is particularly strong at low periods.

The apparent resistivity results indicate that large distortions ($\pm 15\%$) are possible purely due to topographic effects. In the 0.1 s results, apparent resistivities variations are predominately positive. At 1 s the variations are predominately negative. This is to be expected as there is less inductive influence in the response. The apparent resistivity results remain constant from 1 s to 100 s. This, coupled with the small phase angle response, indicates that the distortion has become purely galvanic at these higher periods. In high period data, positive and negative changes in apparent resistivity occur at negative and positive topographic gradients, respectively.

Both the phase angle and apparent resistivity changes are highly localised. In all of the plots we observe positive and negative changes occurring in close proximity to one another. Further modelling needs to be undertaken using meshes which more accurately represent topographic structures in order to better identify the scale on which topography will effect MT data. As these results are based on a homogeneous half-space conductivity model, it would also be worthwhile investigating the effect of conductivity heterogeneities

within the topography, due to the relationship between small scale topography features and lithology.

The results from the WALDIM dimensionality analysis of the 08GA-C1 MT line (Figure 10) are unable to test the results of the topography modelling section. We can see from Figure 8 that the highest topographic gradient occurs in the north of the survey line, despite the sites in the south having a higher elevation (Table 3). Comparing the locations of the three northernmost sites (Site 25, Site 24 and Site 23) with the results in Figure 3, we would expect there to be little topographic distortion in these sites. The WALDIM results show that the data are galvanically distorted in all three sites, however for the majority of the signal, distortion is indeterminable. It is most likely that this distortion is arising from near-surface conductors rather than topographic gradients. This could be investigated by accurate topography modelling in the area of the three sites.

In summary, these results show the importance of taking topography into account when processing a survey in an area with large slopes. Although there appears to be no regional effect of topography on MT soundings, there is great danger in ignoring topographic effects in areas with high topographic gradients. Due to the difficulty in accounting for topographic effects, it is recommended that surveys avoid regions with high topographic gradients where possible.

Near-surface conductors

Results of the near-surface conductor modelling (Figure 5) show both local and regional effects.

At each period, synthetic readings in Lake Frome have a much lower resistivity than the 20 Ωm resistivity of the homogeneous half-space. This is to be expected, as ρ_a senses the resistivity of the entire column of rock through which the signal passes, some

of which is the highly conductive Lake Frome layer. A similar effect is observed in the ϕ maps.

Of particular interest is the halo of elevated apparent resistivity which surrounds Lake Frome in the imaging of apparent resistivity. This structure is the same for all periods; it is a galvanic effect. A possible cause for these anomalous ρ_a values is the change of conductivity between the Lake Frome and background regions. In the presence of electric fields, charges will accumulate at conductivity boundaries. These charges produce their own, frequency independent, electric fields. These fields have the potential to modify the measured electric fields, which would lead to distorted ρ_a values. This effect is localised to the area immediately adjacent to the conductivity boundary, which is to be expected considering the inverse square relation between the electric field strength from a point charge and the distance from the same charge. Alternatively, this effect may simply be a numerical artefact.

The inductive effect of near-surface conductors can be observed in the phase angle plots of Figure 5. At a period of 0.1 s it is observed that Lake Frome produces a small regional change in phase. This is to be expected, as the skin depth of a 0.1 s period signal in a $0.67 \Omega\text{m}$ body is ~ 130 m, which is comparable to the depth of the modelled conductivity anomaly. An increase in phase angle at some of the Lake Frome boundaries is also observed. These increases appear to be focused in areas where the boundary runs perpendicular to the electric field polarisation.

The plots of the 1 s, 10 s and 100 s phase angle data are mostly homogeneous, and do not differ in structure from the input model. This shows that by 1 s, any effect of Lake Frome is purely galvanic.

The imaging of both the phase angle and apparent resistivity changes is limited by the large cell size in the model (1 km). More modelling, making use of finer meshes over smaller areas, is required to determine the nature of this distortion.

Another phenomenon that is observed is a small regional (outside of Lake Frome) effect seen at all frequencies in the ρ_a plots. Half-loops form at the edges of Lake Frome, which close in on themselves at other edge points up to 100 km away. This effect could possibly be explained by considering the nature of the charges which are forming at the lake boundary. For the Z_{xy} polarisation, the electric field is polarised in the north-south direction. When the field is incident on the bottom of Lake Frome there is a change in conductivity going from low to high resulting in the formation of a charge distribution. When the field is incident on the top of Lake Frome there is the same change in conductivity, but it is now a decrease in conductivity across the boundary. This results in a charge distribution of the opposite charge. It is possible that the two charge distributions are form a time-dependent electric dipole, which is causing a perturbation to the regional ρ_a values. It is also possible that this effect is a numerical artefact. The change in ρ_a ($\sim 0.25\%$) is small enough that it would not cause serious distortion to MT data, however more modelling is required to determine the cause of this effect. A synthetic study using embedded conductive objects with regular geometries (e.g. a triangle and a circle) could be used to further investigate the regional effect of near-surface conductors.

We can compare these findings to the results of the WALDIM dimensionality analysis of the 08GA-C1 MT line (Figure 10). Figure 8 shows the site locations along the 08GA-C1 MT line. The sites which are closest to Lake Frome are sites 17, 18 and 19, however these are among the least distorted sites on the line (although they show distortion at some periods, many more periods have been determined undistorted compared to the other sites). This supports the findings that the effect of a near-surface conductor has limited regional influence. It is also observed there is no correlation between low elevation sites (Site 7 to Site 21 are all below 40 m) and distortion. This is an interesting

result, as in this scenario sites with low elevation are near drainage systems, and these would be more likely to be affected by near-surface inhomogeneities.

Both the synthetic results and a comparison with real data show that near-surface conductors has a negligible impact on regional EM fields. However, the local effect is much stronger, and as such it would be unwise to conduct a survey along the boundary of the lake. The results also show that at sufficiently low periods there is an inductive response arising from near-surface conductive bodies.

Basinal distortion

The results of the thin-sheet modelling (Figure 7) indicate that the conductance contrast between the basinal sediments and the basement in the area has high distortion potential. A skew angle greater than 5 would usually be interpreted as representing a 3-D structure at depth, however in this study a layered Earth model is beneath the thin-sheet. Similarly, the high anisotropy values could be interpreted as indicating a structure at depth with a preferential flow direction, which is not the case in this synthetic example. By comparing the skew and anisotropy at different periods, we can conclude that the data is period dependent, with an increase in period leading to an increase in distortion. At periods much lower than 46 s it is expected that the effect becomes insignificant due to the small size of the skin depth with respect to the basin structures. This indicates that this distortion is largely a long period phenomenon. This basinal distortion particularly is problematic in the case where the survey array is not sufficiently large to image the basins.

Results of the constrained (Model 2) and unconstrained (Model 1) inversions (Figure 11) support the hypothesis that basin structures have the ability to distort MT signals. In the south of the profile Model 2 appears to give the best agreement with seismic interpretations, however for the most part it is inconclusive which inversion pro-

duced the better model. Nevertheless, the fact that the constrained and unconstrained inversions produced different models supports the findings that nearby basins have the potential to distort MT data. Although the results of our thin-sheet modelling predict that distortion from basins becomes more prevalent at longer periods, the major differences between Model 1 and Model 2 occur at relatively shallow depths (in the upper 30 km). As this is contrary to our expectations, it is recommended that further synthetic modelling of conductive basins is undertaken with different methods in order to give insight on the period dependence of basinal distortion. The constrained inversion was limited by the lack of information on the conductive structure of the Arrowie Basin, and further data collection would be required to provide a more accurate prior model. Better inversions could also be made by increasing the error floor on the diagonal data, as these were difficult to fit to the model (see Appendix). Furthermore, many of the data in the inversion had also been affected by galvanic distortion (Figure 10). It is therefore recommended that in order to provide the most accurate model, and hence allow better comparisons with seismic interpretations, the inversions should be remade using a code more suited to dealing with galvanic distortion (see Miensoopust et al., 2013).

The results from both thin-sheet modelling and inversion of real data show that large scale, conductive, off-axis basins have the potential to distort MT data. The results from the inversions show that using a constrained inversion can provide a more realistic fit to the data, or, at the very least, an alternative interpretation.

CONCLUSION

This study has considered the distortion of MT data from near-surface inhomogeneities, topographic gradients and basins. These three factors have been analysed by a combination of synthetic modelling and analysis of real data from the Curnamona Province, South Australia. Firstly, the effect of topography in the northern Flinders Ranges has

been investigated using forward models. The results show both a galvanic and an inductive distortion concentrated at high topographic gradients. The effect of near-surface conductors has also been investigated using forward models based on Lake Frome. These show a small area of galvanic distortion around the circumference of the lake, but no regional effect. The short range of these effects has been supported by distortion analysis of real data in the area. Finally, thin-sheet models have been used to determine the inductive distortion from conductive basins using data from the eastern Arrowie Basin. The results of these models show that basins have the potential to inductively distort MT data on a regional scale. This result has been supported by the comparison of constrained and unconstrained inversions of MT data from the Geoscience Australia 08GA-C1 MT line. The inversion results furthermore show that basinal distortion can be remedied by the inclusion of *a priori* conductivity models. Further work is required in quantifying the effects of topographic gradients and near-surface conductors over small scales, and a second synthetic model of distortion arising from basin structures should be pursued. This study has shown that topography, near-surface conductors and basins all have the potential to distort MT data, and this must be taken into consideration during MT survey design and processing.

ACKNOWLEDGEMENTS

I would like to thank my project supervisor Prof. Graham Heinson for his support, guidance and feedback throughout the Honours year. I would also like to thank Dr. Stephan Thiel, and Dr. Derrick Hasterok, Yohannes Lemma Didana and Kate Robertson, Theo Aravanis of Rio Tinto and Bob Smith, as well the Honours cohort for their insights and suggestions to my project. Finally, a special thanks to Dr. Lars Krieger for his advice on MT, programming and formatting throughout the year.

REFERENCES

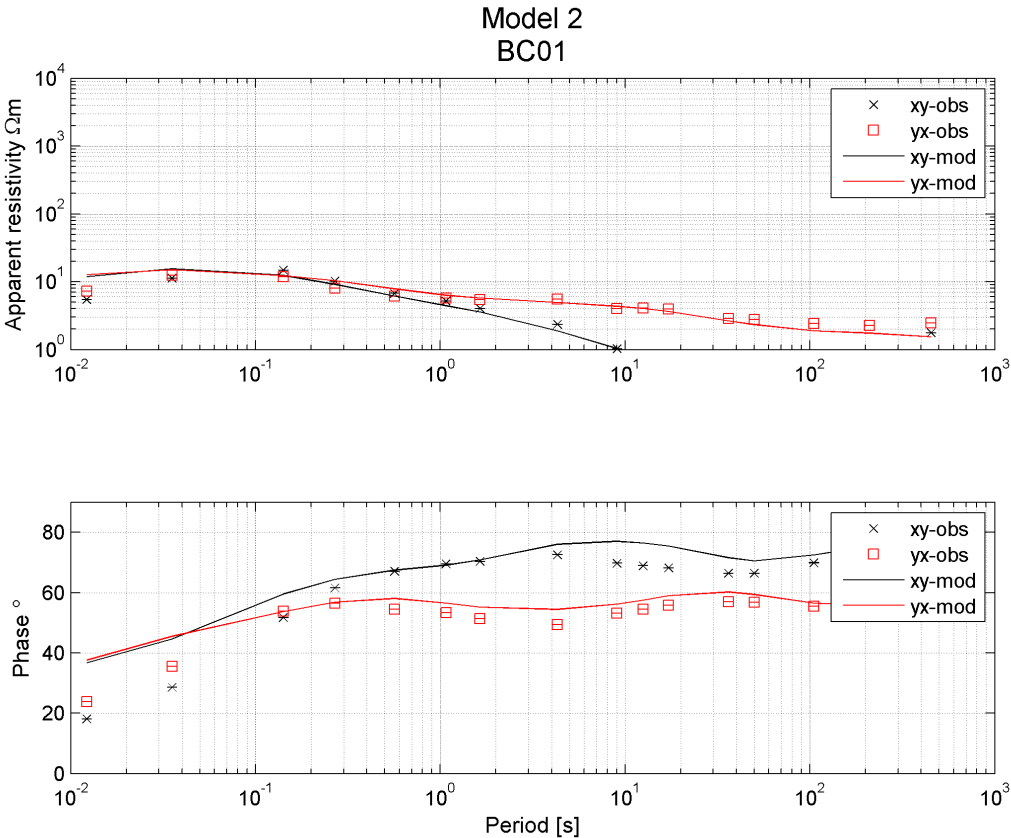
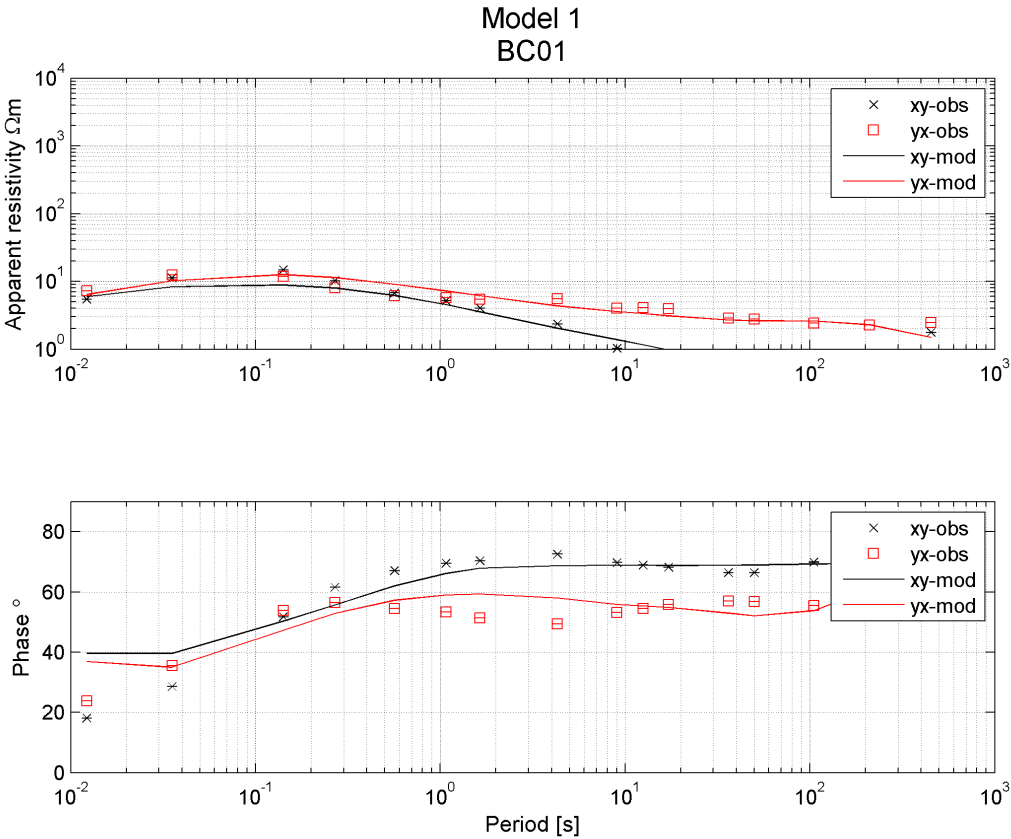
- Agarwal, A. & Weaver, J. (2000). Magnetic distortion of the magnetotelluric tensor: a numerical study, *Earth Planets Space* **52**(5): 347–353.
- Avdeeva, A., Moorkamp, M. & Avdeev, D. (2012). Three-dimensional joint inversion of magnetotelluric impedance tensor data and full distortion matrix, *21st EM Induction Workshop*.
- Baba, K., Tada, N., Utada, H. & Siripunvaraporn, W. (2013). Practical incorporation of local and regional topography in three-dimensional inversion of deep ocean magnetotelluric data, *Geophysical Journal International* **194**(1): 348–361.
- Bahr, D. B., Hutton, E. W., Syvitski, J. P. & Pratson, L. F. (2001). Exponential approximations to compacted sediment porosity profiles, *Computers & Geosciences* **27**(6): 691–700.
- Brugger, J., Long, N., McPhail, D. & Plimer, I. (2005). An active amagmatic hydrothermal system: The Paralana hot springs, Northern Flinders Ranges, South Australia, *Chemical Geology* **222**(1–2): 35–64.
- Caldwell, T. G., Bibby, H. M. & Brown, C. (2004). The magnetotelluric phase tensor, *Geophysical Journal International* **158**(2): 457–469.
- Chave, A. D. & Jones, A. G. (2012). *The magnetotelluric method: Theory and practice*, Cambridge University Press.
- Chave, A. & Smith, J. (1994). On electric and magnetic galvanic distortion tensor decompositions, *Journal of Geophysical Research* **99**(B3): 4669–4682.
- Cohen, T. J., Nanson, G. C., Jansen, J. D., Jones, B. G., Jacobs, Z., Treble, P., Price, D. M., May, J.-H., Smith, a. M., Ayliffe, L. K. & Hellstrom, J. C. (2011). Continental aridification and the vanishing of Australia’s megalakes, *Geology* **39**(2): 167–170.
- Conor, C. H. & Preiss, W. V. (2008). Understanding the 1720–1640 Ma Palaeoproterozoic Willyama Supergroup, Curnamona Province, Southeastern Australia: Implications for tectonics, basin evolution and ore genesis, *Precambrian Research* **166**(1–4): 297–317.
- Deckker, P. D. (1983). Australian salt lakes: their history, chemistry, and biota—a review, *Hydrobiologia* **105**(1): 231–244.
- DeGroot-Hedlin, C. (1995). Inversion for regional 2-D resistivity structure in the presence of galvanic scatterers, *Geophysical Journal International* **122**(1): 877–888.
- Fabris, A. J., Keeling, J. L. & Fidler, R. W. (2009). Surface geochemical expression of bedrock beneath thick sediment cover, Curnamona Province, South Australia, *Geochemistry: Exploration, Environment Analysis* **9**(3): 237–246.
- Farquharson, C. & Craven, J. (2009). Three-dimensional inversion of Magnetotelluric data for mineral exploration: an example from the McArthur River uranium deposit, Saskatchewan, Canada, *Journal of Applied Geophysics* **68**(4): 450–458.
- Fox, R., Hohmann, G., Killpack, T. & Rijo, L. (1980). Topographic effects in resistivity and induced-polarization surveys, *Geophysics* **45**(1): 75–93.
- Garcia, X., Boerner, D. & Pedersen, L. B. (2003). Electric and magnetic galvanic distortion decomposition of tensor CSAMT data. Application to data from the Buchans Mine (Newfoundland, Canada), *Geophysical Journal International* **154**(3): 957–969.
- Groom, R. & Bailey, R. (1989). Decomposition of magnetotelluric impedance tensors in the presence of local three-dimensional galvanic distortion, *Journal of Geophysical Research* **94**(B2): 1913–1925.
- Groom, R. & Bailey, R. (1991). Analytic investigations of the effects of near-surface three-dimensional galvanic scatterers on MT tensor decompositions, *Geophysics* **56**(4): 496–518.

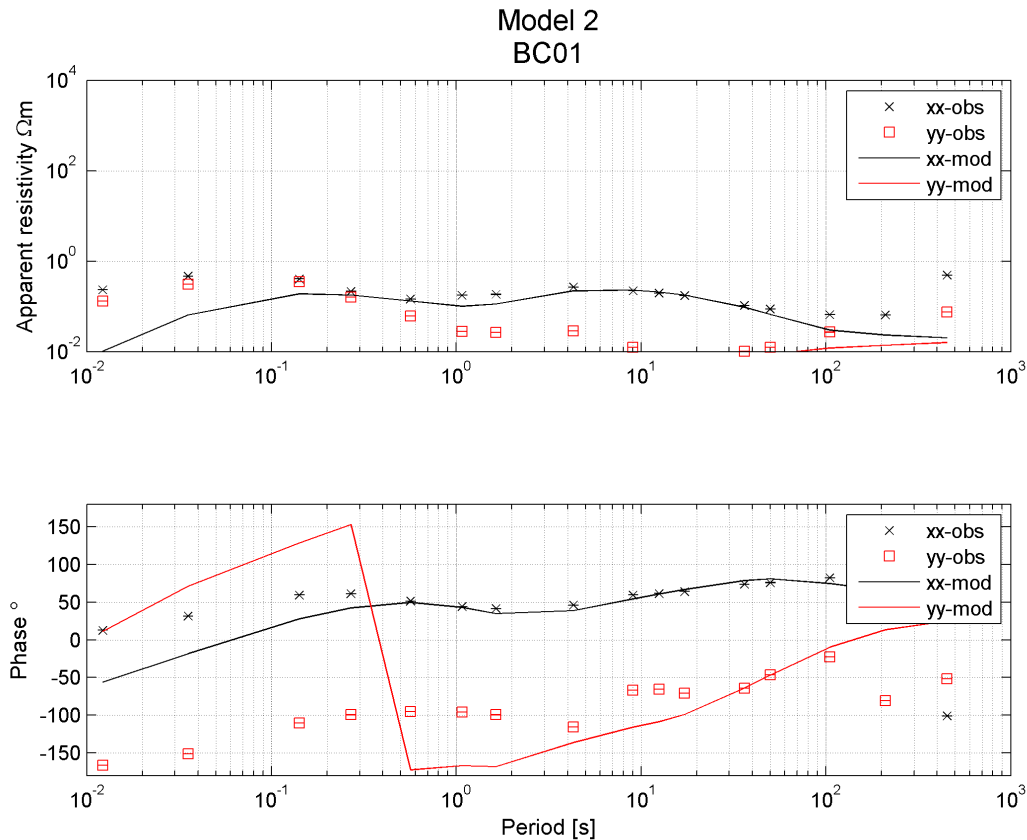
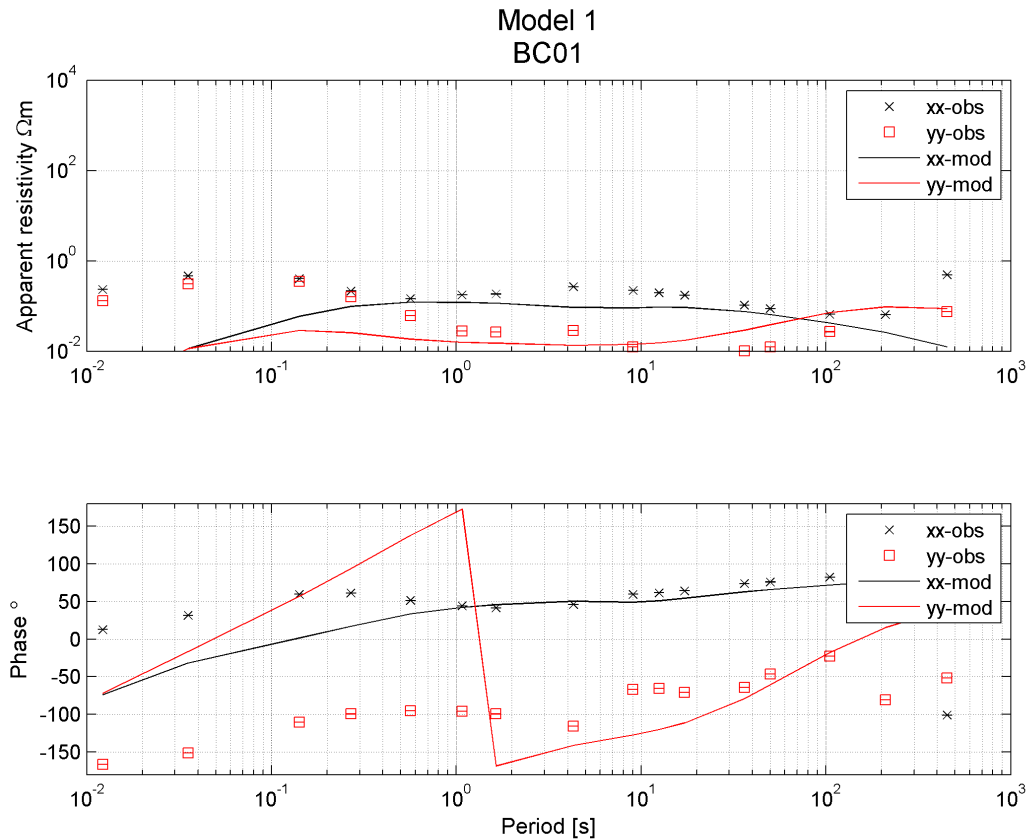
- Heinson, G. & Lilley, F. (1993). An application of thin-sheet electromagnetic modelling to the Tasman Sea, *Physics of the Earth and Planetary Interiors* **81**(1): 231–251.
- Heise, W. & Pous, J. (2003). Anomalous phases exceeding 90° in magnetotellurics: anisotropic model studies and a field example, *Geophysical Journal International* **155**(1): 308–318.
- Hermance, J. F. (1983). DC telluric fields in three dimensions: A refined finite-difference simulation using local integral forms, *Geophysics* **48**(3): 331–340.
- Hutchinson, M. F., Stein, J. A. & Stein, J. L. (2009). GEODATA 9 second digital elevation model (DEM-9S) version 3, *Online at* <http://www.ga.gov.au>.
- Key, K. & Constable, S. (2011). Coast effect distortion of marine magnetotelluric data: Insights from a pilot study offshore northeastern Japan, *Physics of the Earth and Planetary Interiors* **184**(3–4): 194–207.
- Korsch, R., Preiss, W. & Blewett, R. (2010). Geological interpretation of deep seismic reflection and magnetotelluric line 08GA-C1: Curnamona Province, South Australia, *South Australian Seismic and MT Workshop*, number May, p. 30.
- Ledo, J., Queralt, P. & Pous, J. (1998). Effects of galvanic distortion on magnetotelluric data over a three-dimensional regional structure, *Geophysical Journal International* **132**: 295–301.
- Lezaeta, P. (2003). Beyond magnetotelluric decomposition: Induction, current channeling, and magnetotelluric phases over 90° , *Journal of Geophysical Research* **108**(B6): 1–20.
- Mackie, R., Smith, J. & Madden, T. (1994). Three-dimensional electromagnetic modeling using finite difference equations: The magnetotelluric example, *Radio Science* **29**(4): 923–935.
- Maier, R., Heinson, G., Thiel, S., Selway, K., Gill, R. & Scroggs, M. (2007). A 3D lithospheric electrical resistivity model of the Gawler Craton, Southern Australia, *Applied Earth Science: IMM Transactions section B* **116**(1): 13–21.
- Martí, A., Queralt, P., Jones, A. G. & Ledo, J. (2005). Improving Bahr’s invariant parameters using the WAL approach, *Geophysical Journal International* **163**(1): 38–41.
- Martí, A., Queralt, P. & Ledo, J. (2009). WALDIM: A code for the dimensionality analysis of magnetotelluric data using the rotational invariants of the magnetotelluric tensor, *Computers & Geosciences* **35**(12): 2295–2303.
- McKirdy, D., Weaver, J. & Dawson, T. (1985). Induction in a thin sheet of variable conductance at the surface of a stratified earth—II. Three-dimensional theory, *Geophysical Journal International* **80**(1): 177–194.
- McNeice, G. W. & Jones, A. G. (2001). Multisite, multifrequency tensor decomposition of magnetotelluric data, *Geophysics* **66**(1): 158–173.
- Miensopust, M. P., Queralt, P. & Jones, A. G. (2013). Magnetotelluric 3-D inversion—a review of two successful workshops on forward and inversion code testing and comparison, *Geophysical Journal International* **193**(3): 1216–1238.
- Milligan, P. & Lilley, F. (2010). Magnetotelluric results along the NS Curnamona seismic traverse to the east of Lake Frome, South Australia, *ASEG Extended Abstracts* **1**(1): 1–4.
- Mullen, I. & Kellett, J. (2007). Groundwater salinity mapping using airborne electromagnetics and borehole data within the lower Balonne catchment, Queensland, Australia, *International Journal of Applied Earth Observation and Geoinformation* **9**(2): 116–123.
- Naidu, G. D. (2012). *Deep Crustal Structure of the Son-Narmada-Tapti Lineament, Central India*, Springer Theses, Springer Berlin Heidelberg, Berlin, Heidelberg.

- Nam, M. J., Kim, H. J., Song, Y., Lee, T. J. & Suh, J. H. (2008). Three-dimensional topography corrections of magnetotelluric data, *Geophysical Journal International* **174**(2): 464–474.
- Parkinson, W. & Jones, F. (1979). The geomagnetic coast effect, *Reviews of Geophysics* **17**(8): 1999–2015.
- Patro, P. K. & Egbert, G. D. (2011). Application of 3D inversion to magnetotelluric profile data from the Deccan Volcanic Province of Western India, *Physics of the Earth and Planetary Interiors* **187**(1-2): 33–46.
- Quigley, M. C., Cupper, M. L. & Sandiford, M. (2006). Quaternary faults of south-central Australia: Palaeoseismicity, slip rates and origin, *Australian Journal of Earth Sciences* **53**(2): 285–301.
- Revil, A. & Cathles, L. (1998). Electrical conductivity in shaly sands with geophysical applications, *Journal of Geophysical Research* **103**(10): 23925–23936.
- Roach, I. (2012). The Frome airborne electromagnetic survey, South Australia, *ASEG Extended Abstracts* **1**(1): 2011–2013.
- Santos, F. M. & Nolasco, M. (2001). Coast effects on magnetic and magnetotelluric transfer functions and their correction: application to MT soundings carried out in SW Iberia, *Earth and Planetary Science Letters* **186**(1): 283–295.
- Simpson, F. & Bahr, K. (2005). *Practical Magnetotellurics*, Cambridge University Press.
- Siripunvaraporn, W., Egbert, G., Lenbury, Y. & Uyeshima, M. (2005). Three-dimensional magnetotelluric inversion: data-space method, *Physics of the Earth and Planetary Interiors* **150**: 3–14.
- Teasdale, J., Stuart-Smith, P. & Henley, P. (2001). Eastern Arrowie Basin SEEBASE Project, *Technical Report May*.
- Tuncer, V., Unsworth, M., Siripunvaraporn, W. & Craven, J. (2006). Exploration for unconformity-type uranium deposits with audiomagnetotelluric data: A case study from the McArthur River mine, Saskatchewan, Canada, *Geophysics* **71**(6): 201–209.
- Ullman, W. & McLeod, L. (1986). The late-quaternary salinity record of lake Frome, South Australia: evidence from Na⁺ in stratigraphically-preserved gypsum, *Palaeogeography, Palaeoclimatology, Palaeoecology* **54**(1): 153–169.
- Utada, H., Munekane, H. & Tokyo, B.-k. (2000). On galvanic distortion of regional three-dimensional magnetotelluric impedances, *Geophysical Journal International* **140**(1): 385–398.
- Wade, C. E., Reid, A. J., Wingate, M. T., Jagodzinski, E. a. & Barovich, K. (2012). Geochemistry and geochronology of the c. 1585 Ma Benagerie Volcanic Suite, southern Australia: Relationship to the Gawler Range Volcanics and implications for the petrogenesis of a Mesoproterozoic silicic large igneous province, *Precambrian Research* **206-207**(1): 17–35.
- Weaver, J. T., Agarwal, A. K. & Lilley, F. E. M. (2000). Characterization of the magnetotelluric tensor in terms of its invariants, *Geophysical Journal International* **141**(2): 321–336.

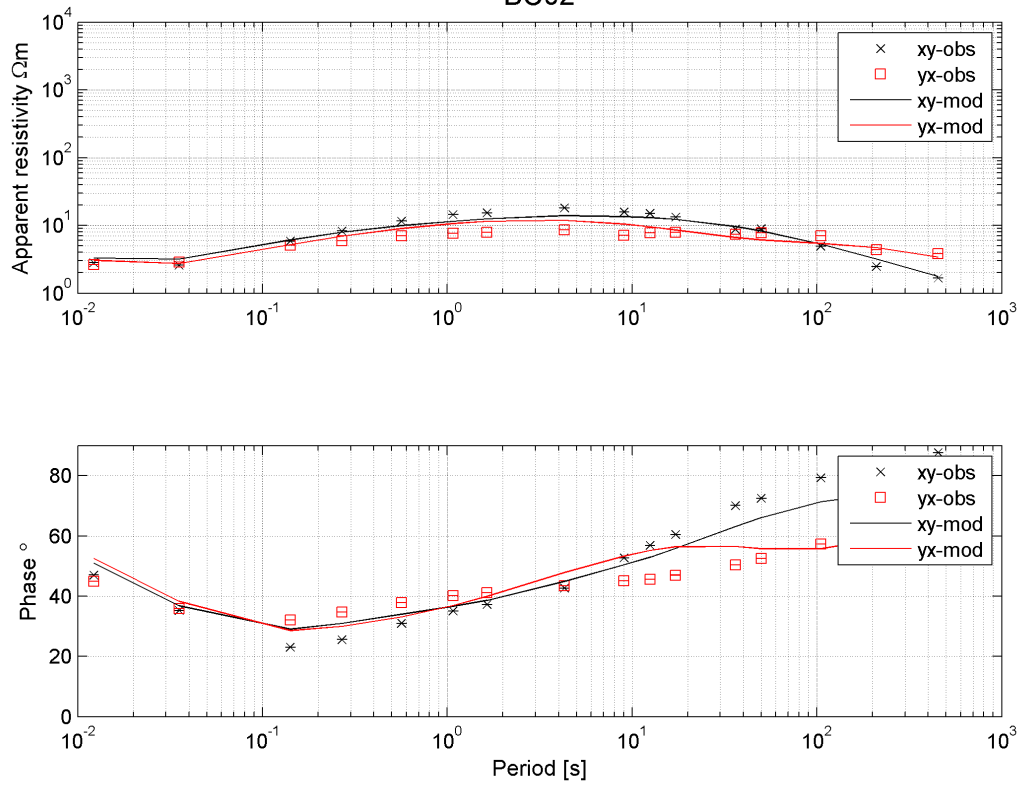
APPENDIX: MODEL FIT PLOTS

The graphs on the following pages show the model fit plots for the inversions undertaken in this study. For each site the off-diagonal fits are given for Model 1 and Model 2, with the diagonal fits on the subsequent page.

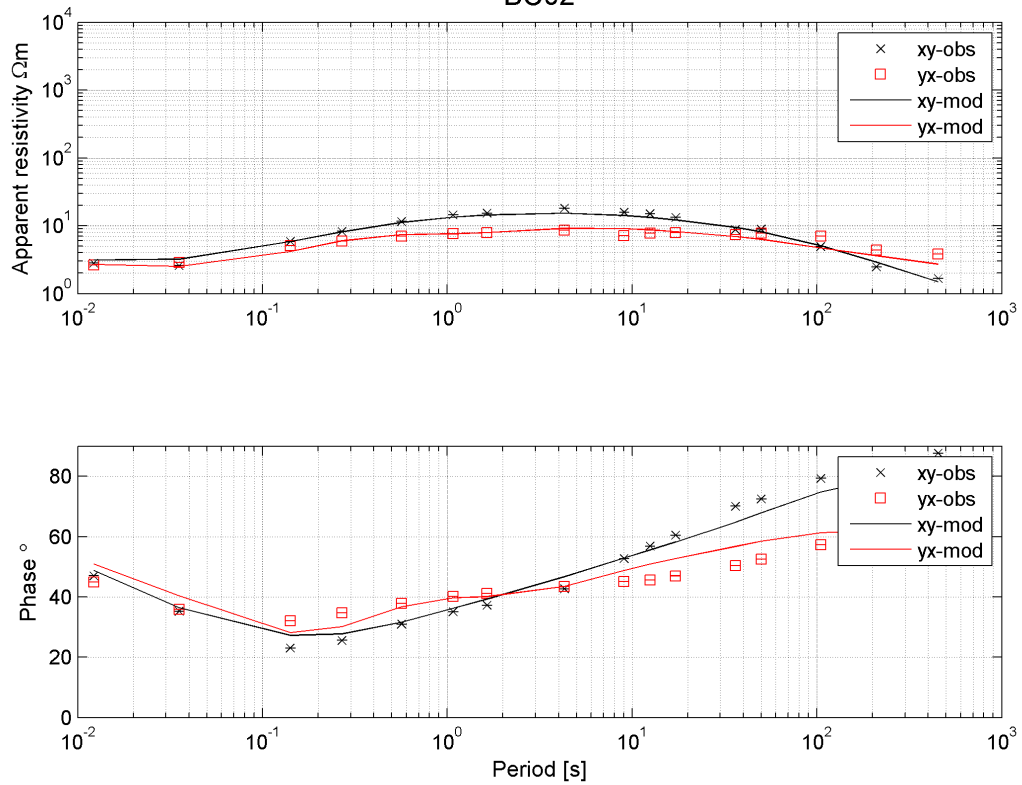


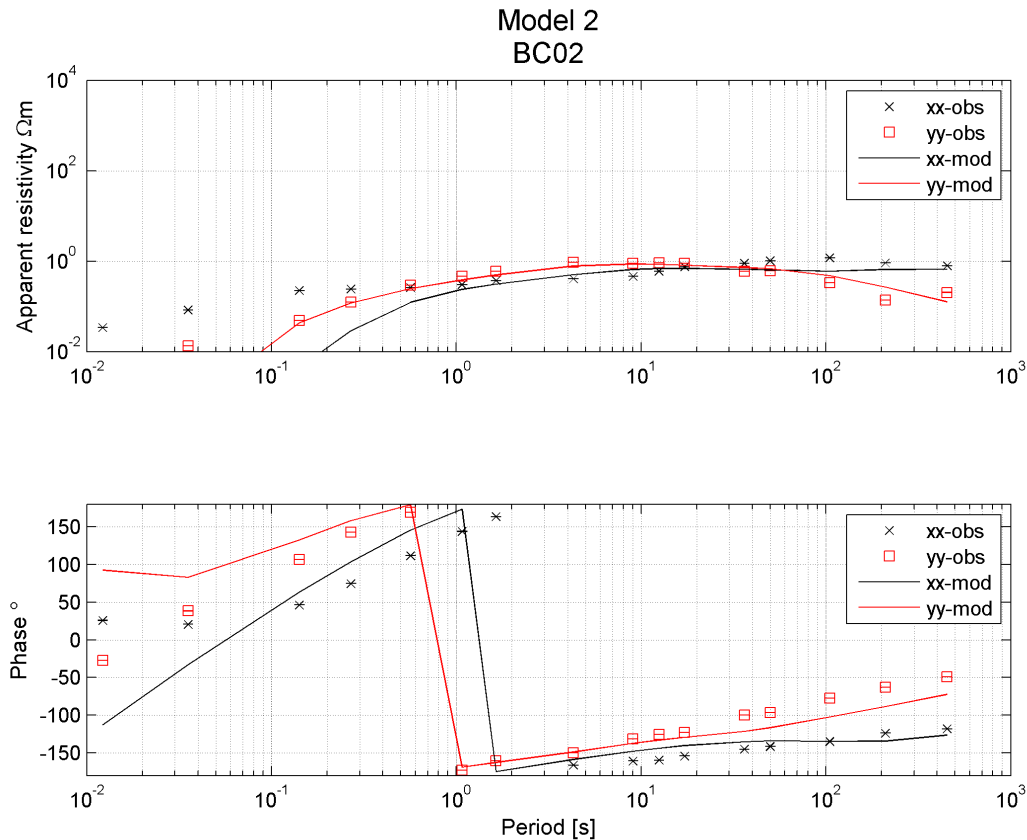
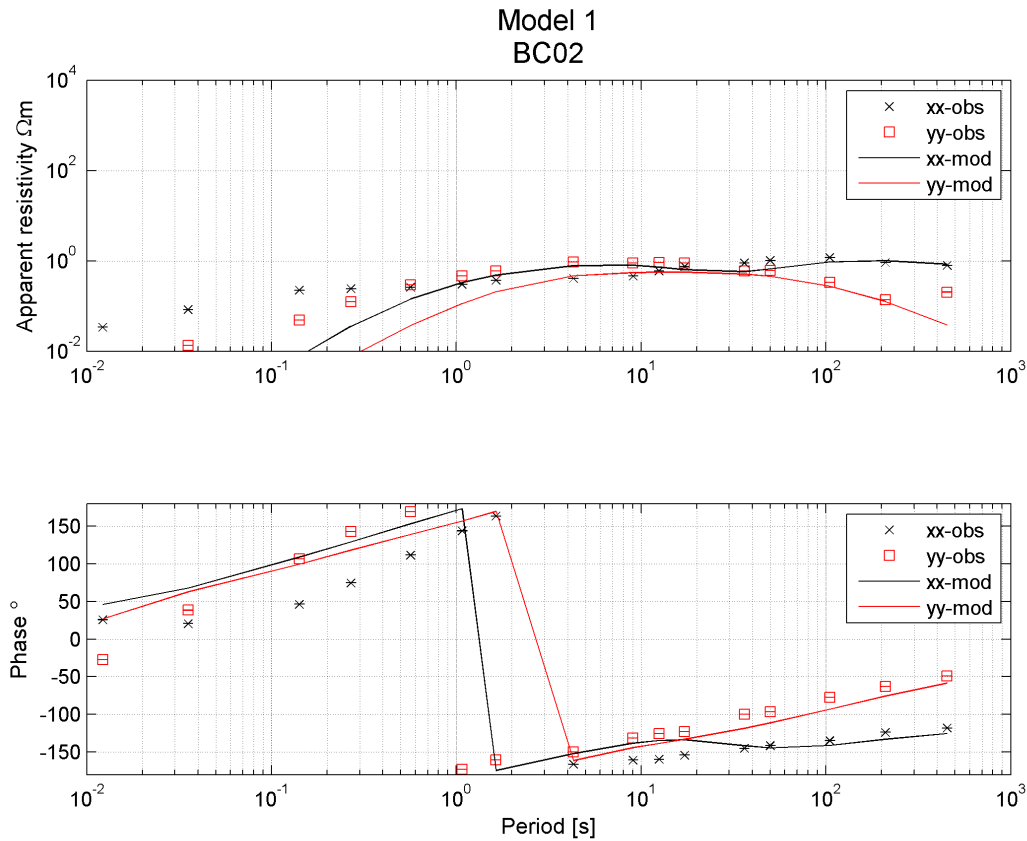


Model 1
BC02

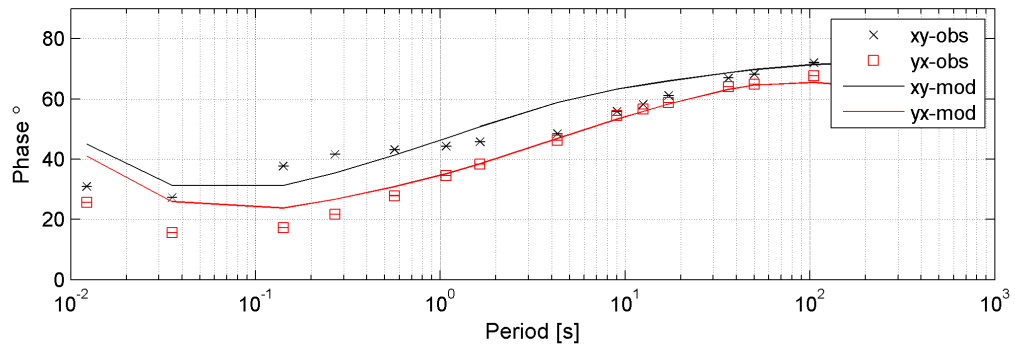
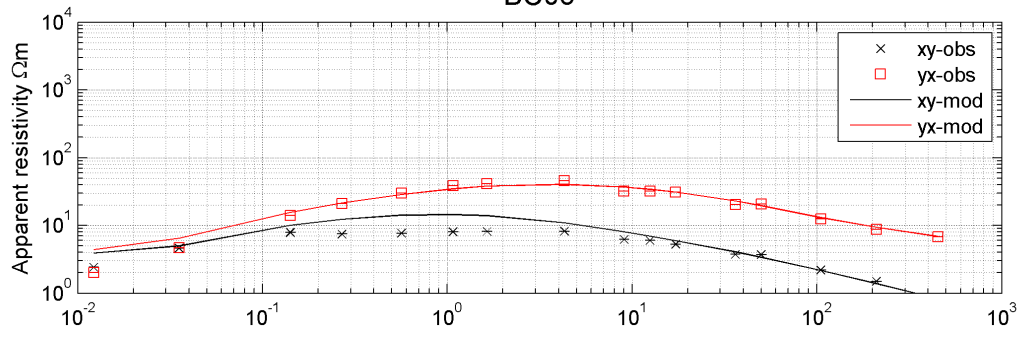


Model 2
BC02

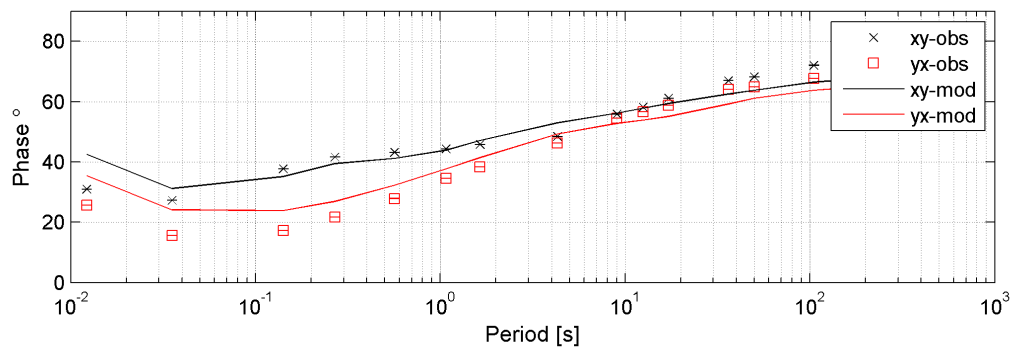
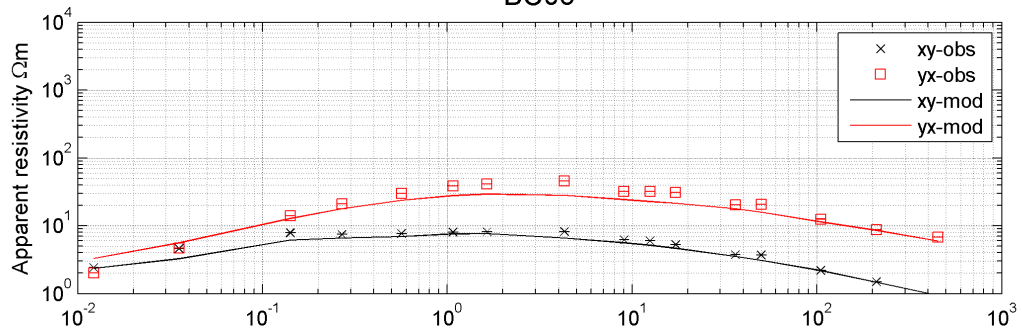


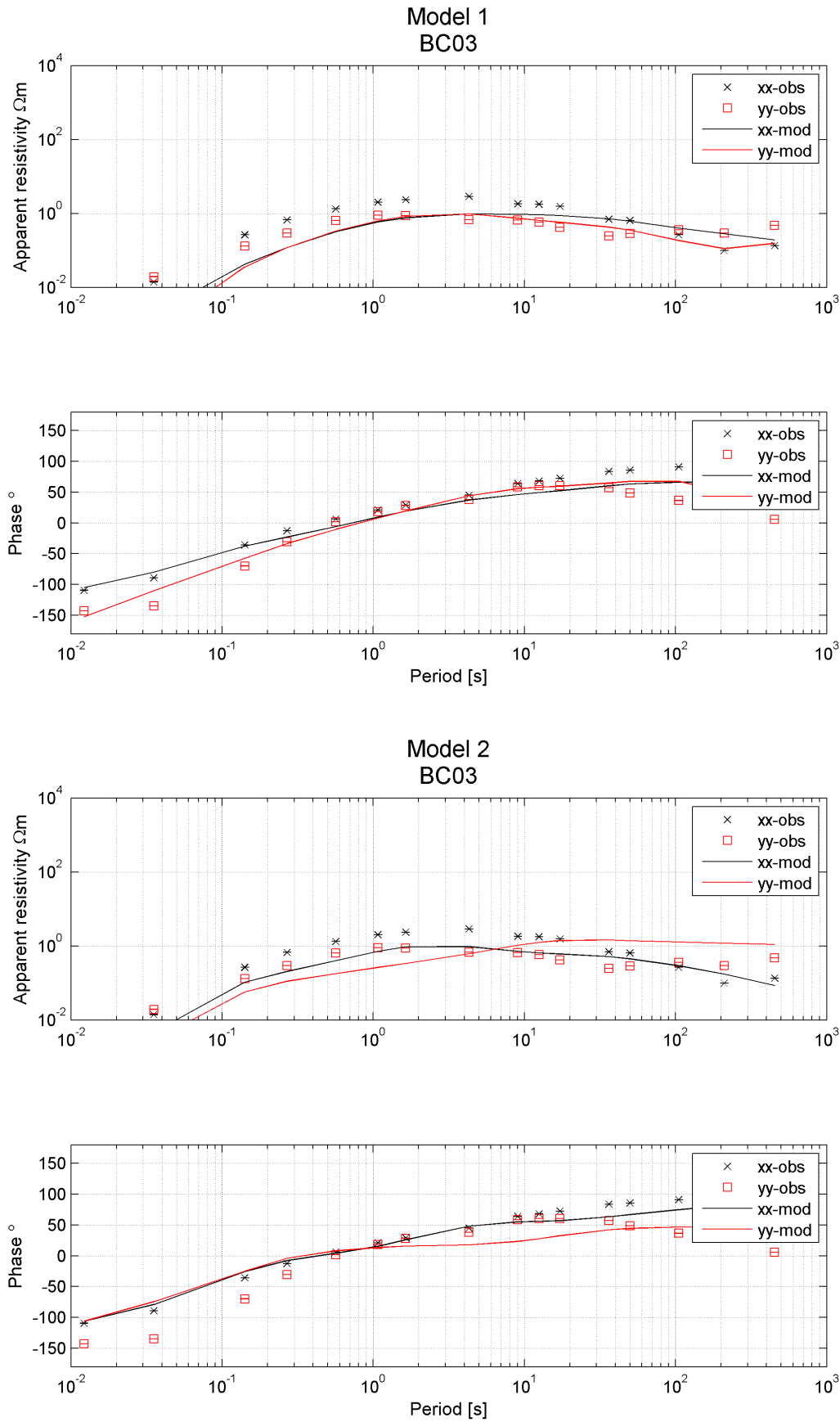


Model 1
BC03

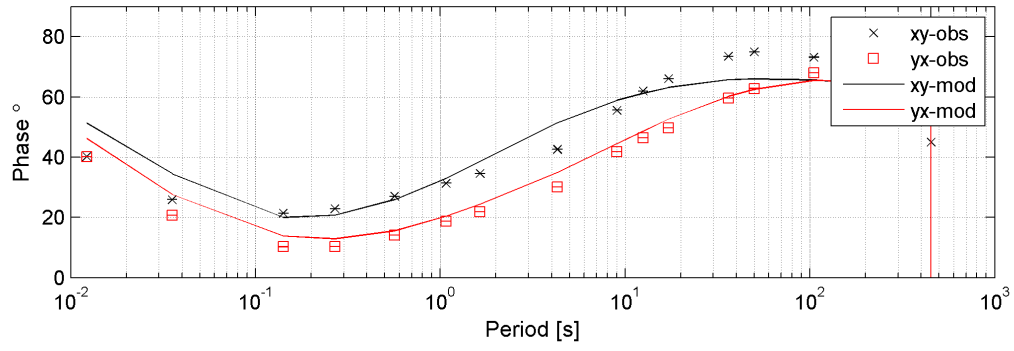
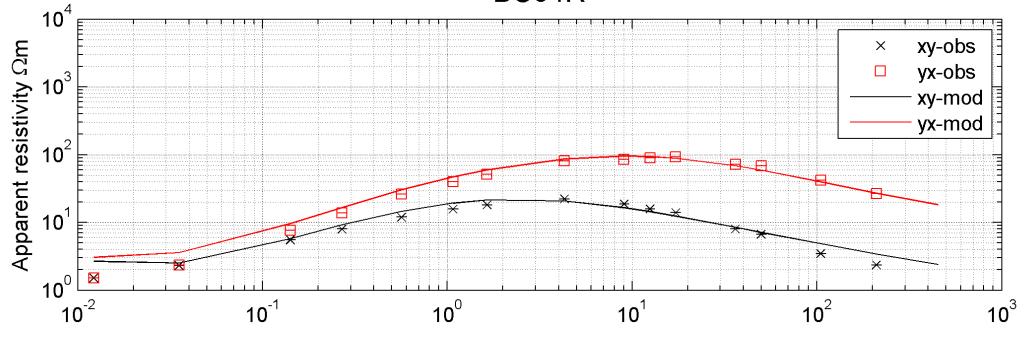


Model 2
BC03

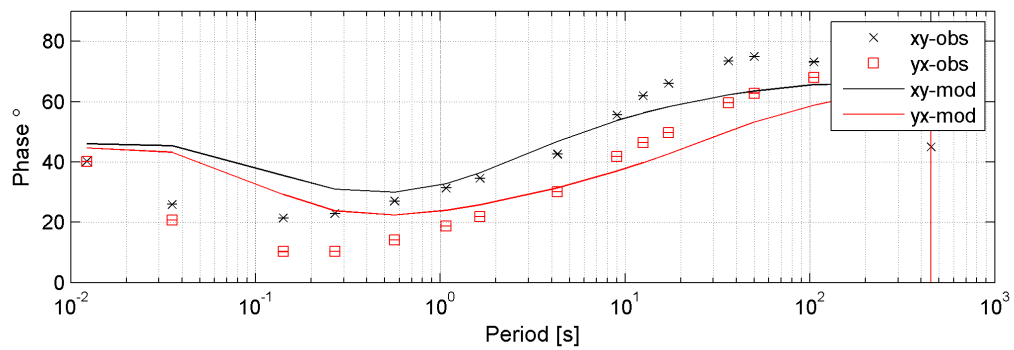
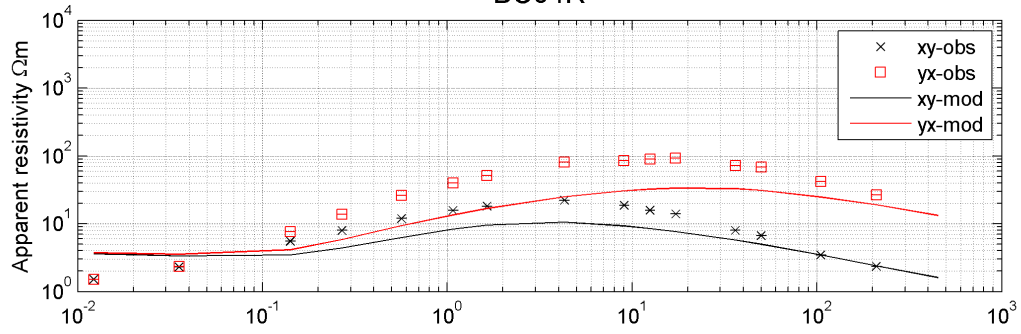


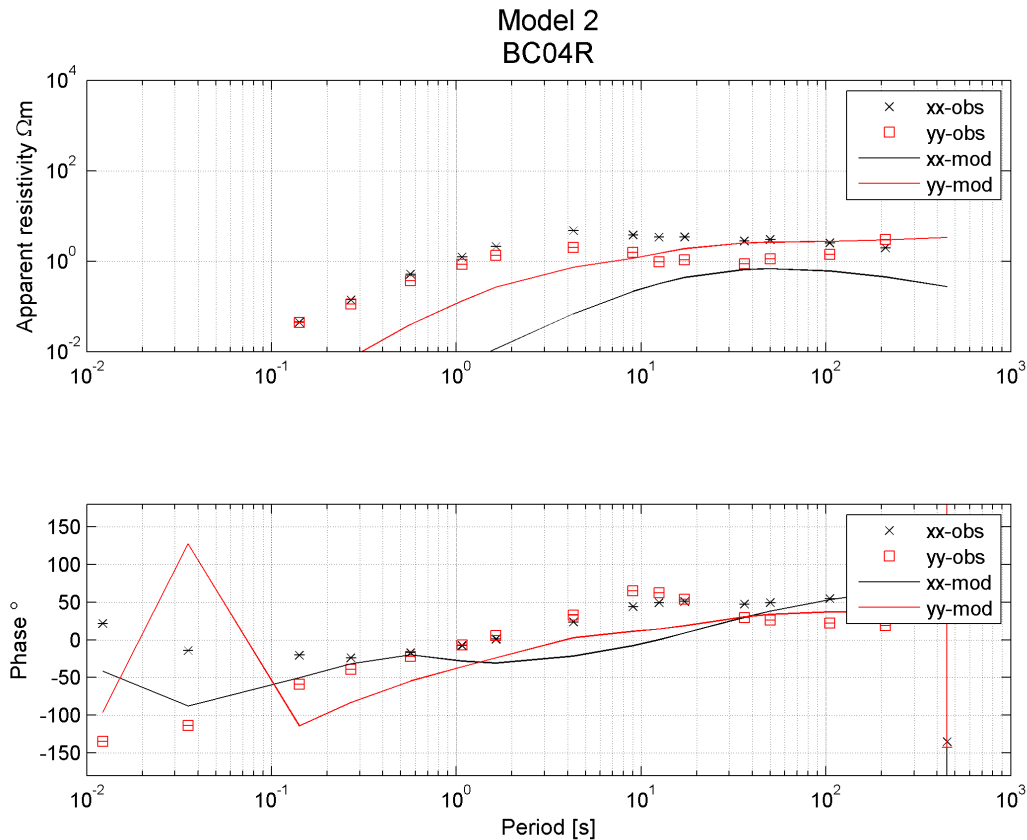
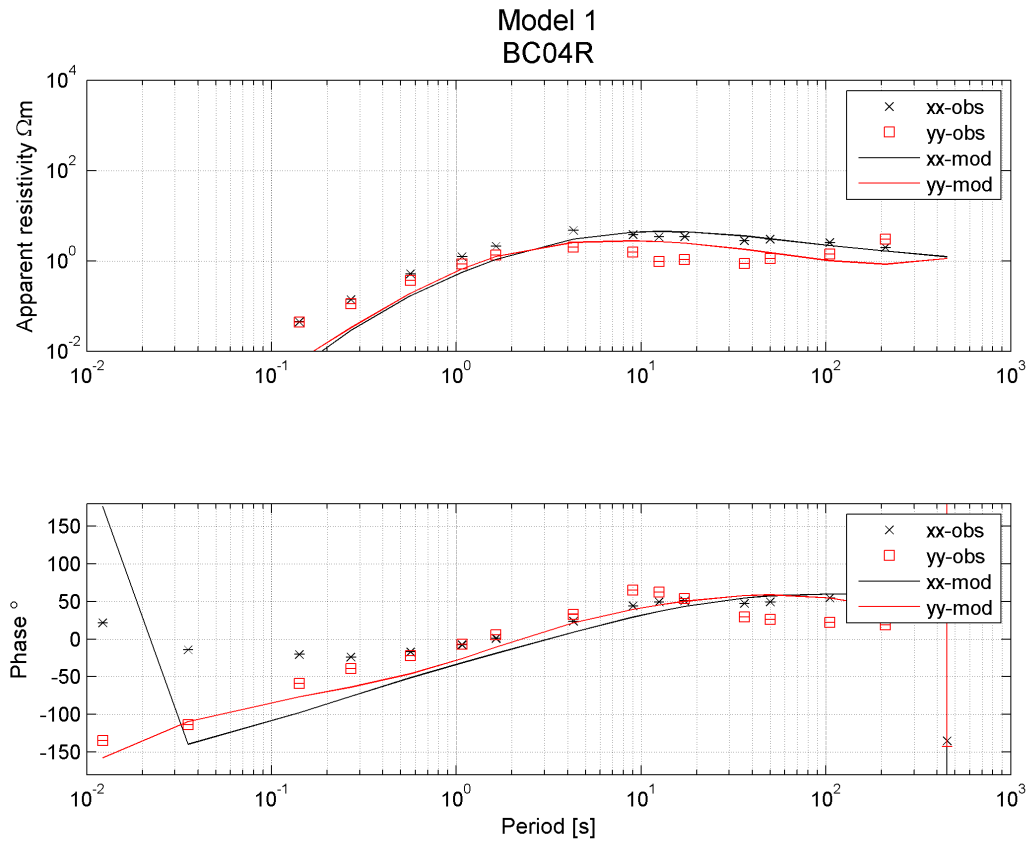


Model 1
BC04R

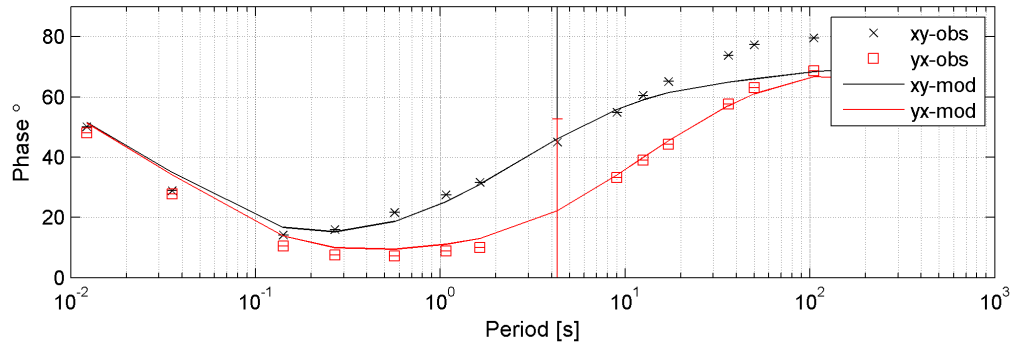
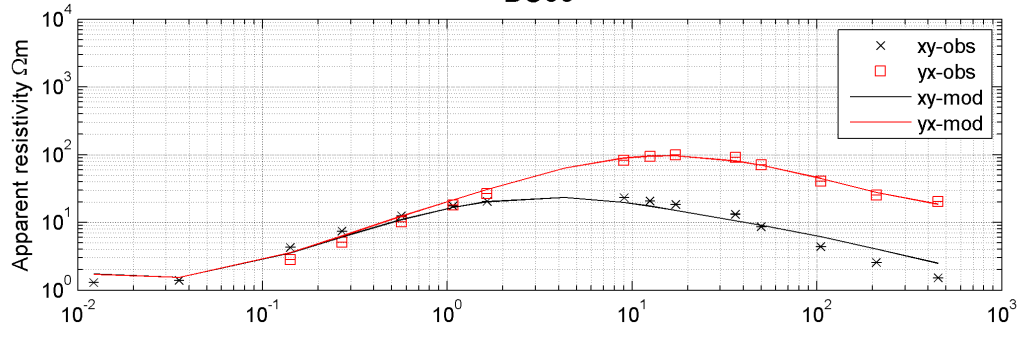


Model 2
BC04R

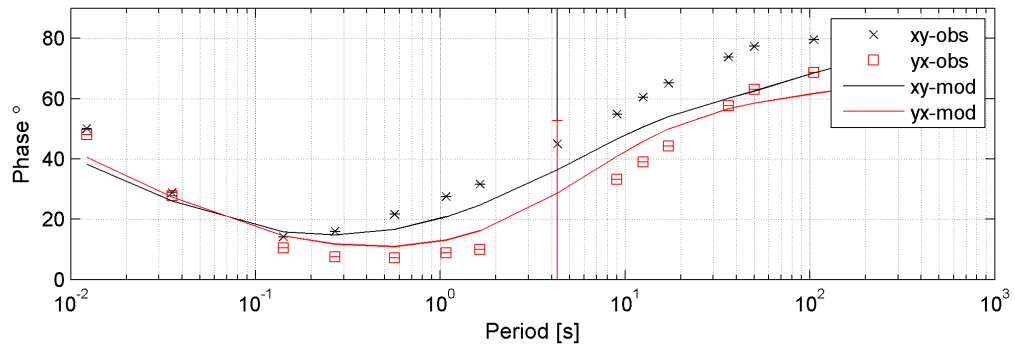
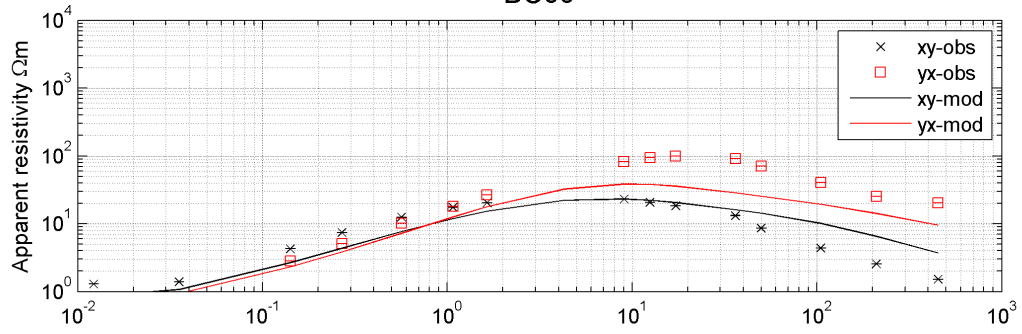


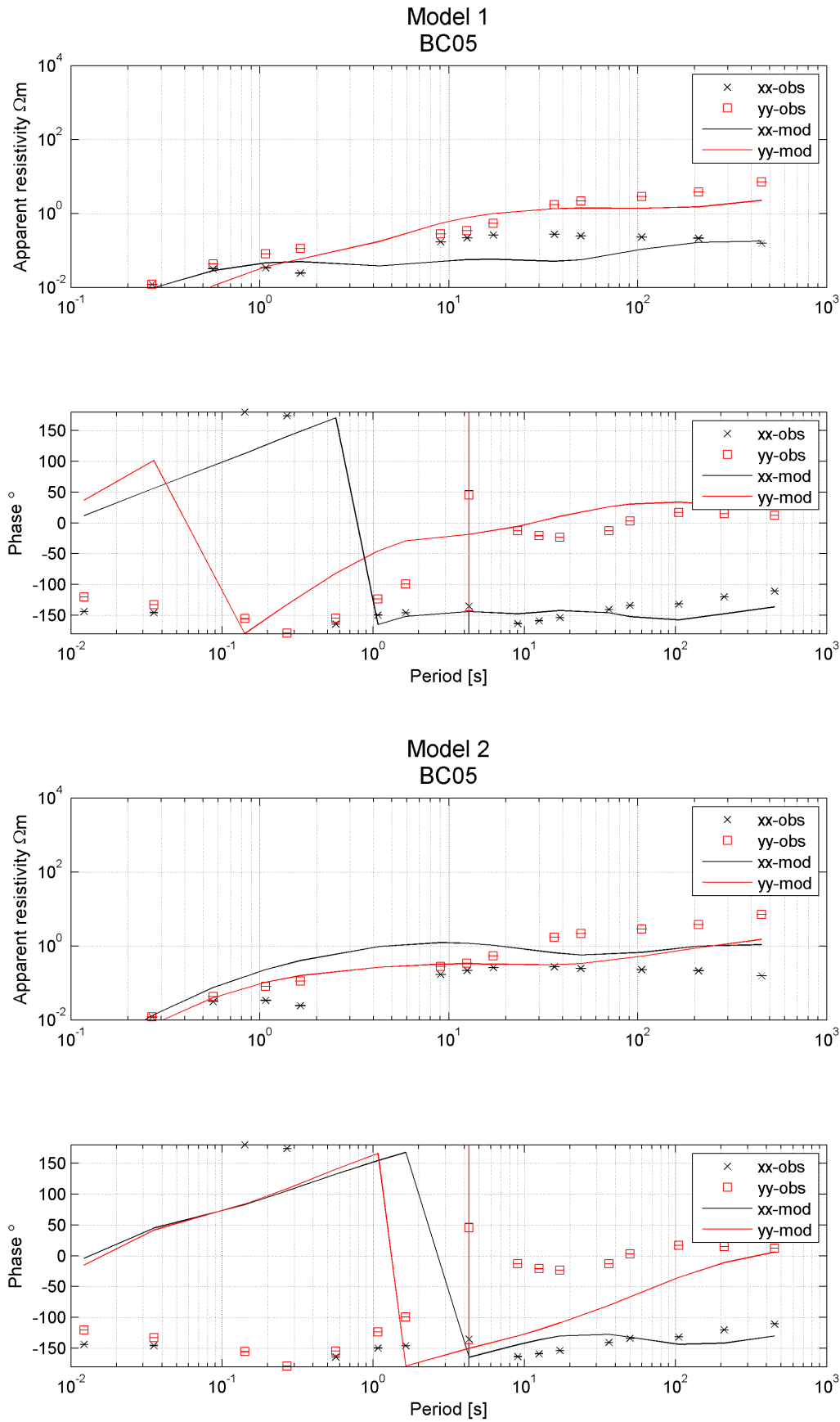


Model 1
BC05

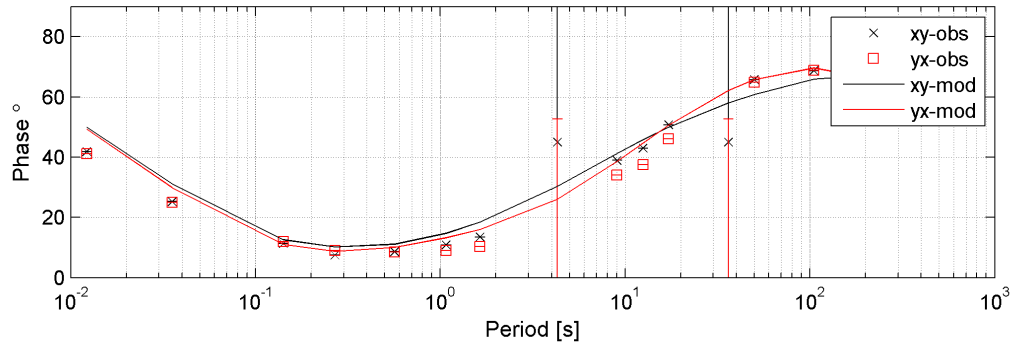
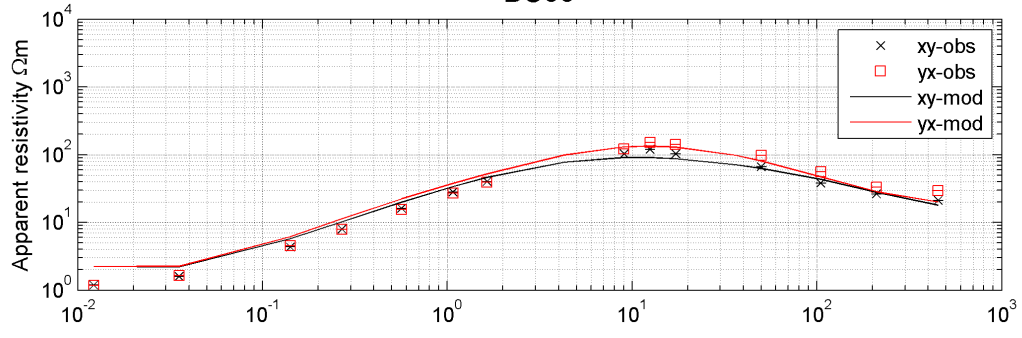


Model 2
BC05

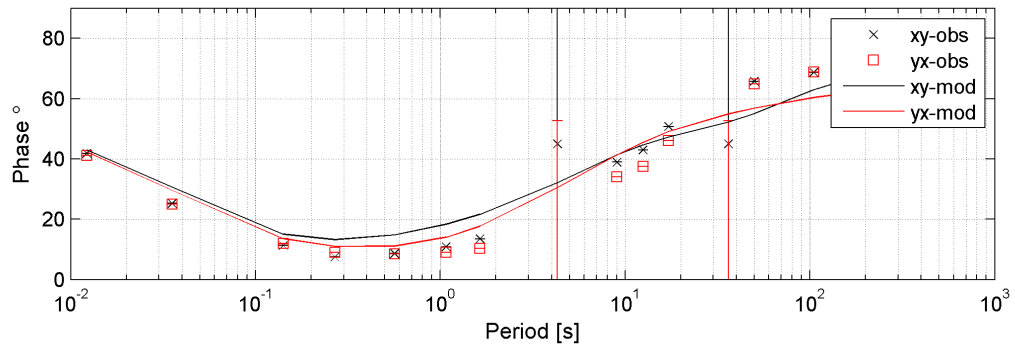
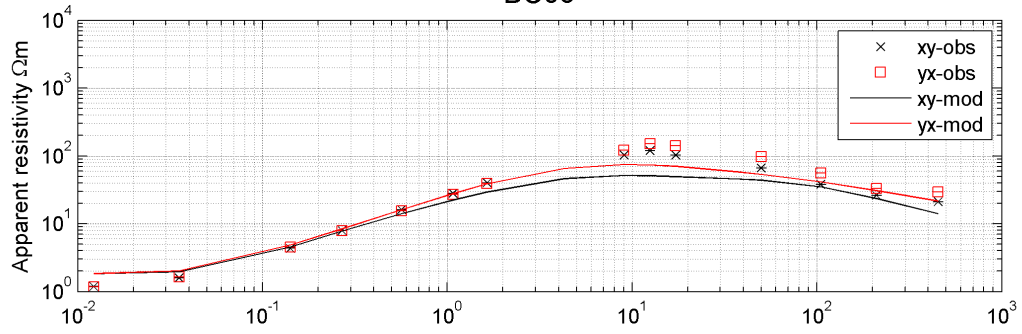


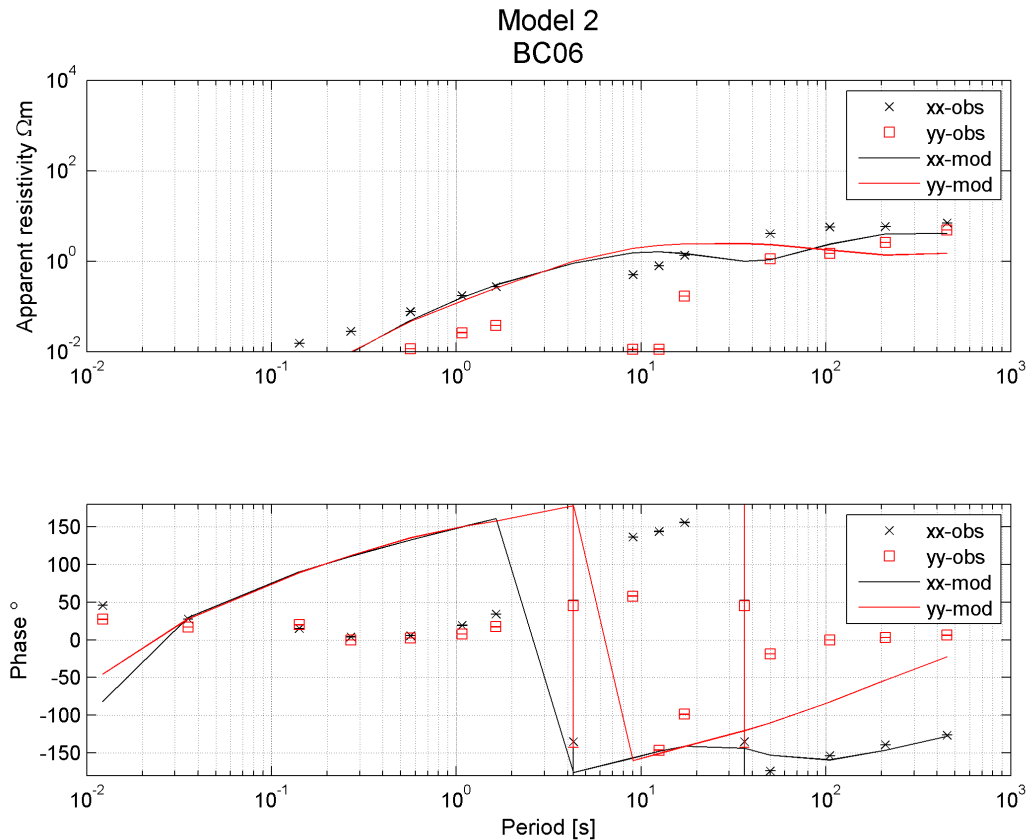
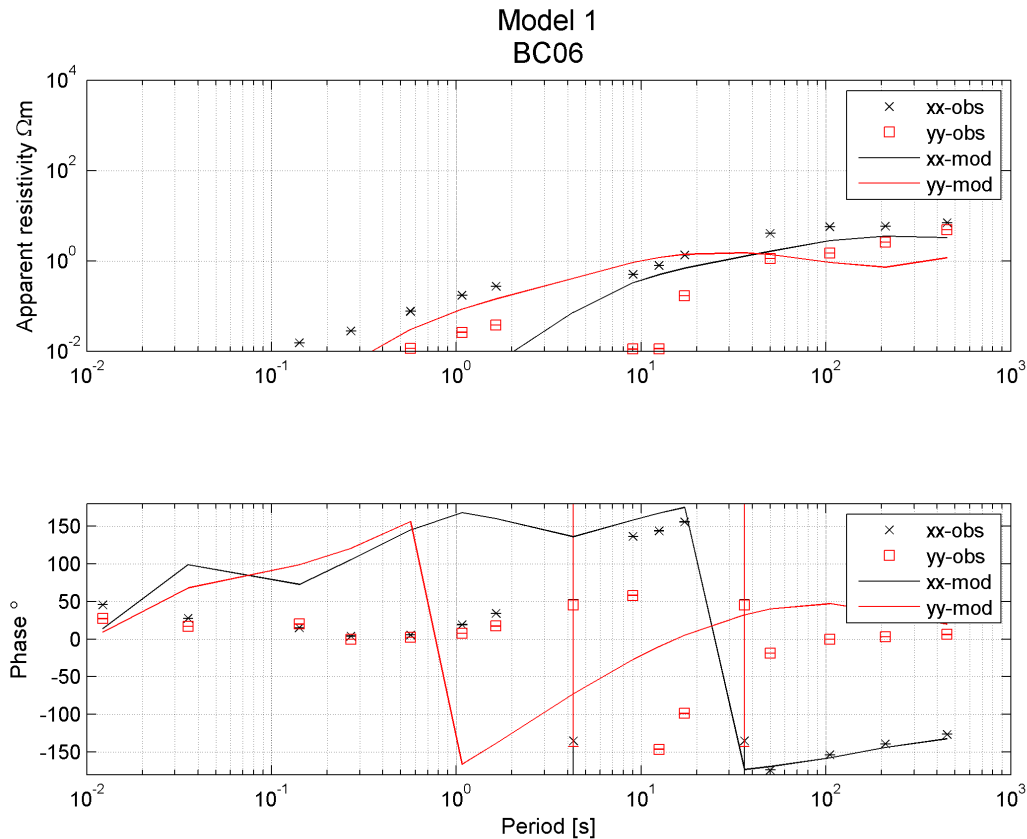


Model 1
BC06

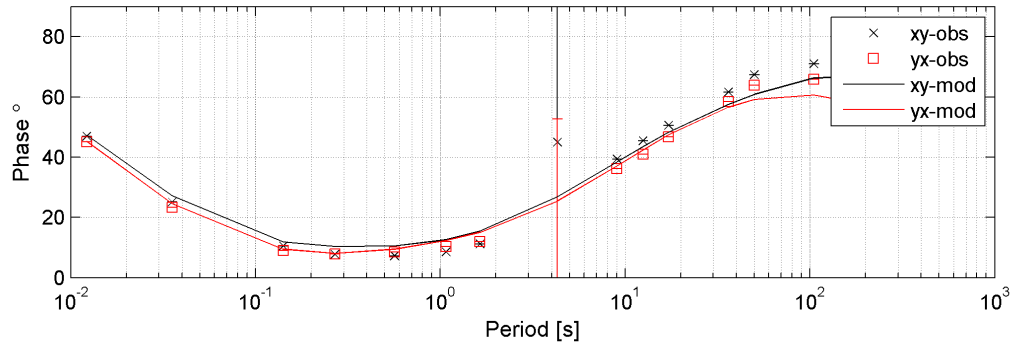
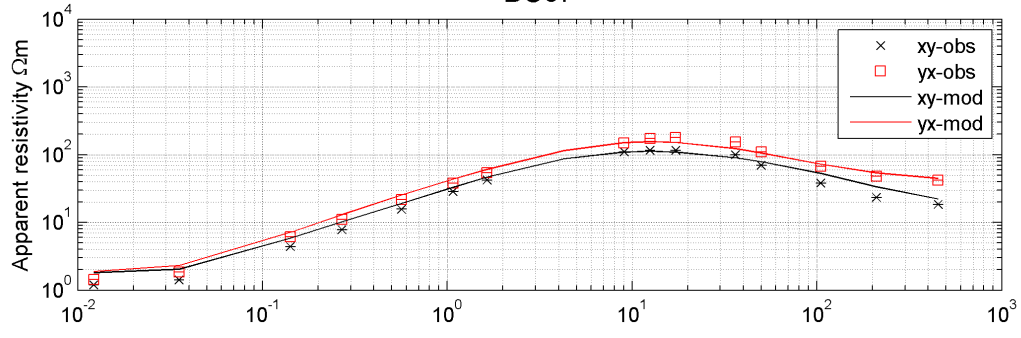


Model 2
BC06

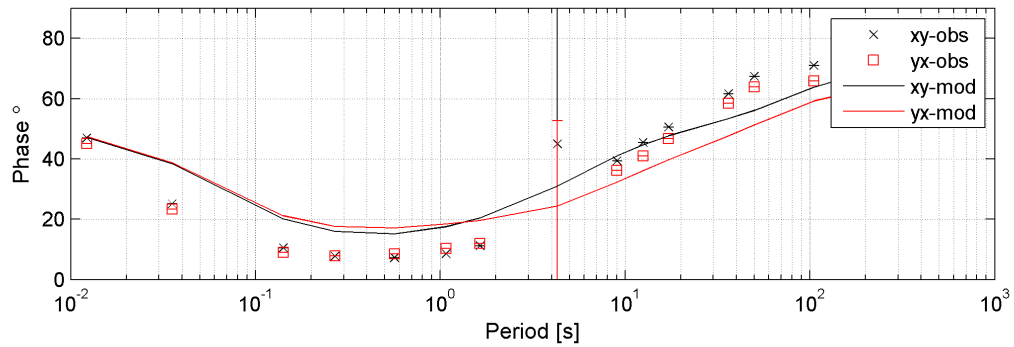
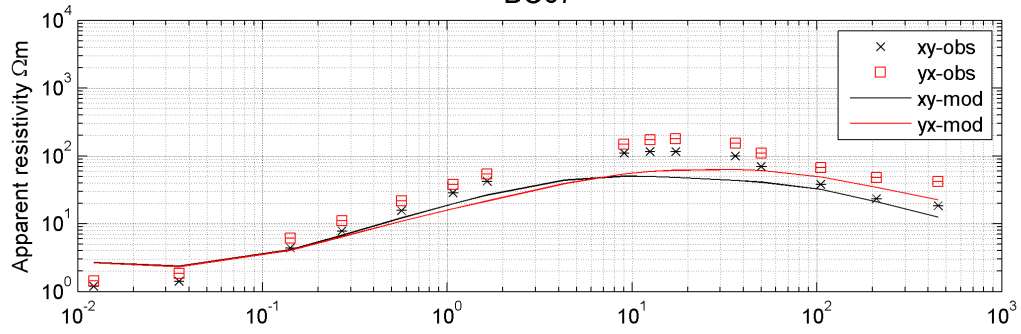


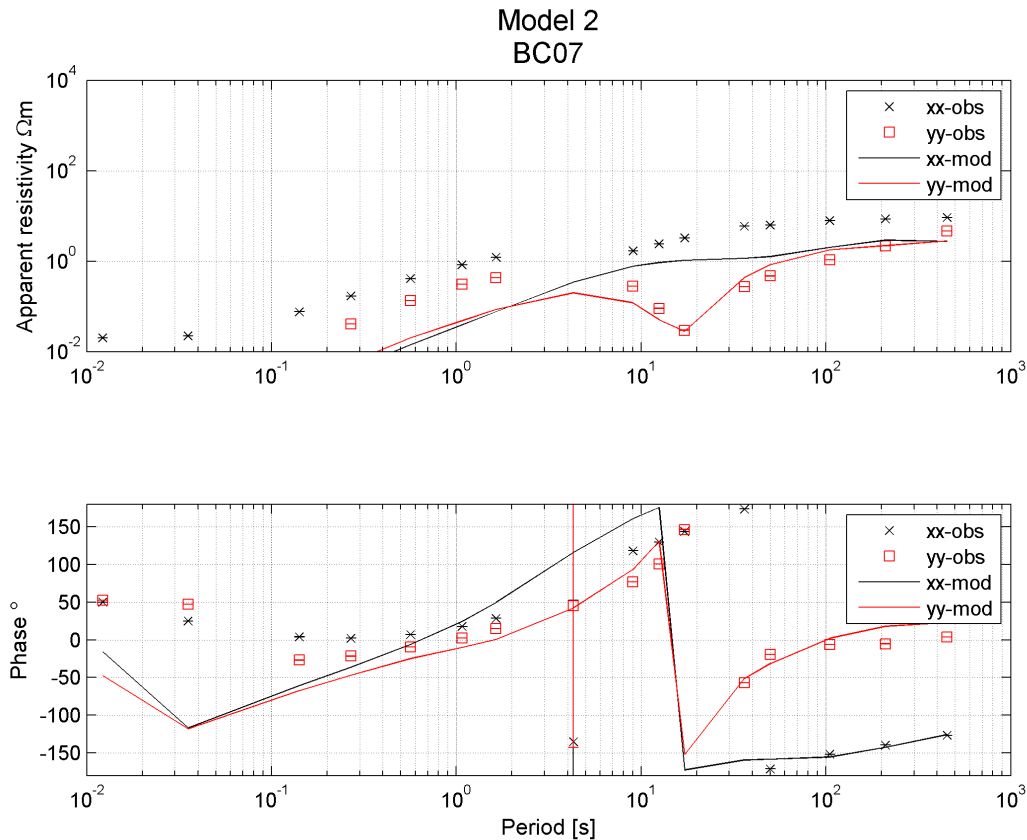
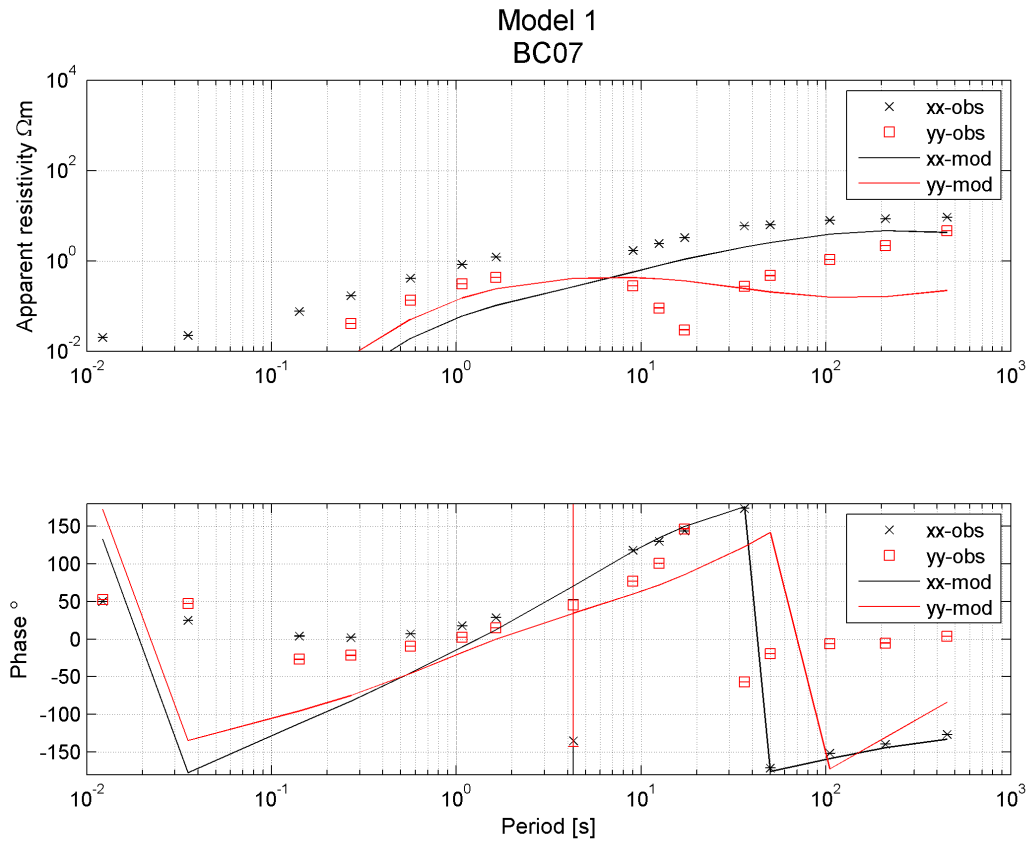


Model 1
BC07

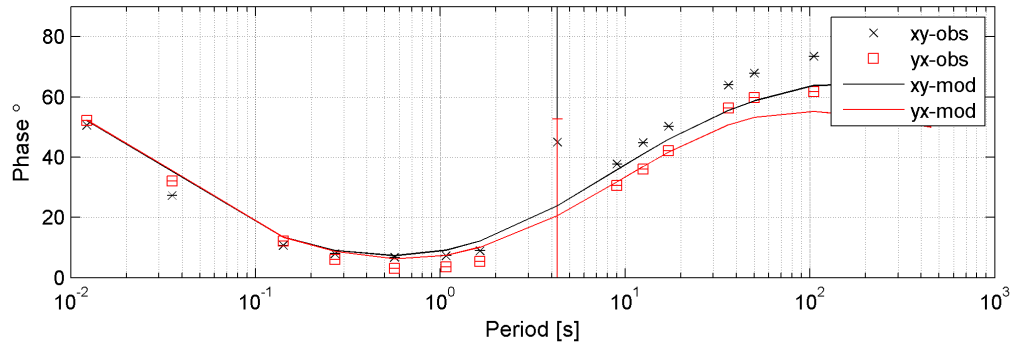
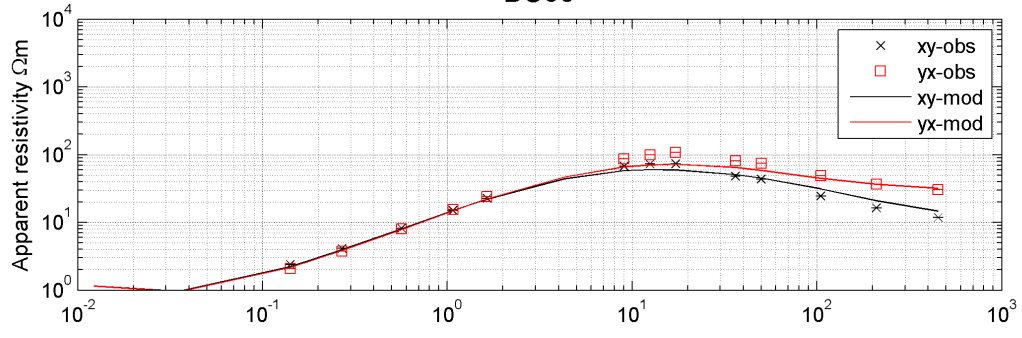


Model 2
BC07

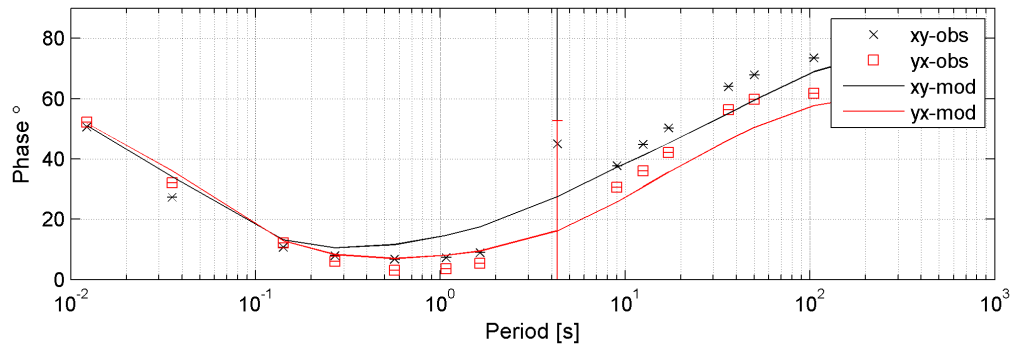
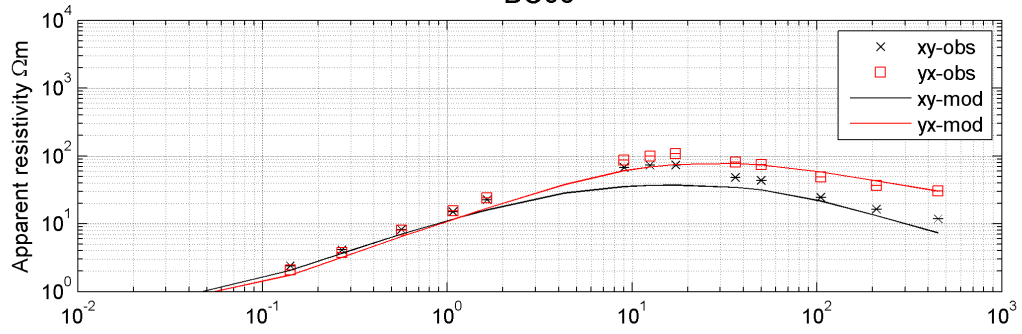


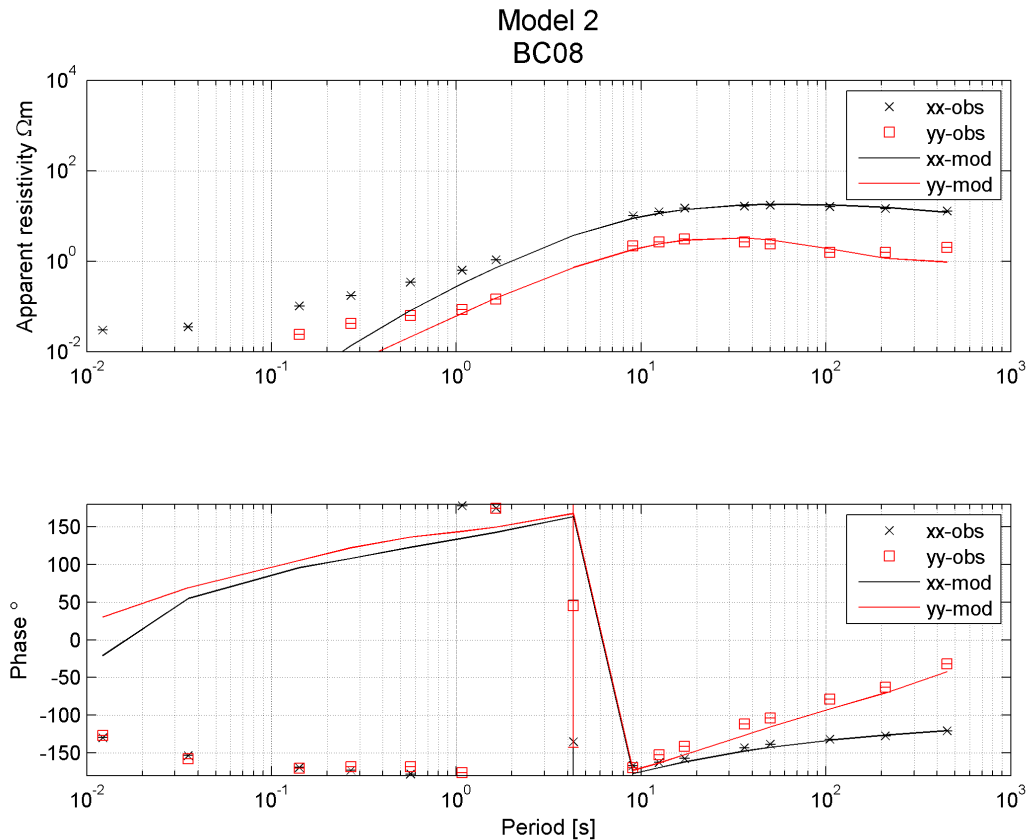
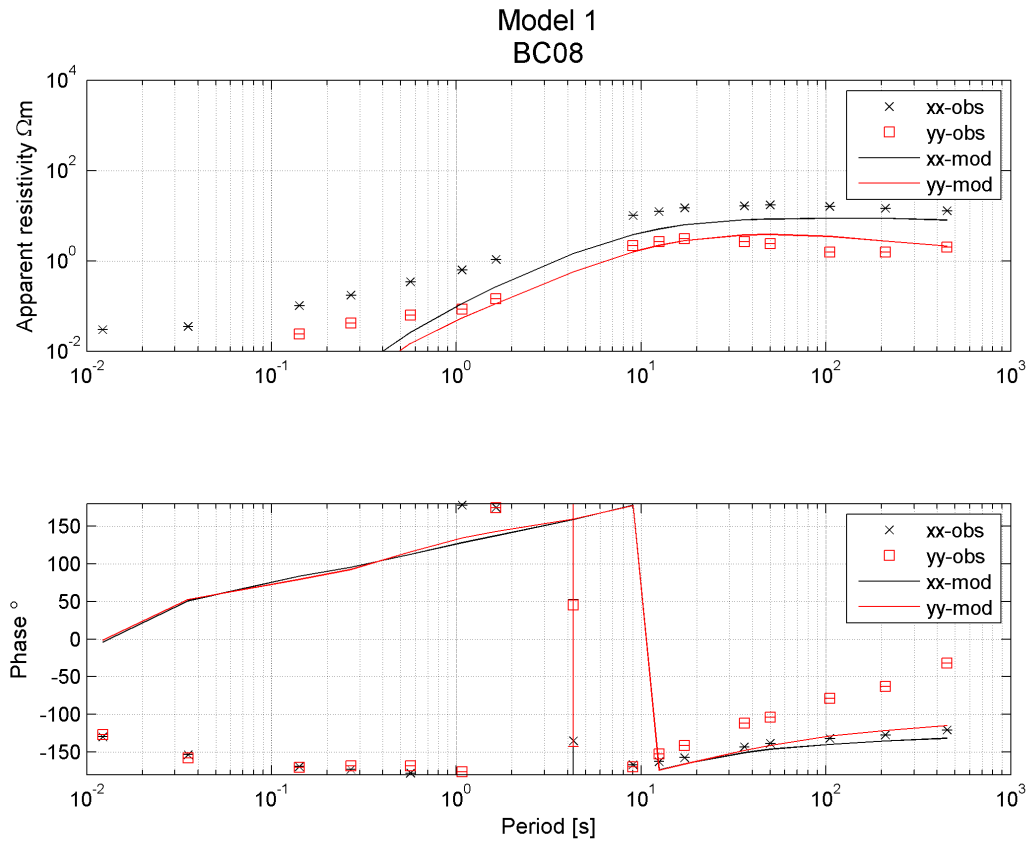


Model 1
BC08

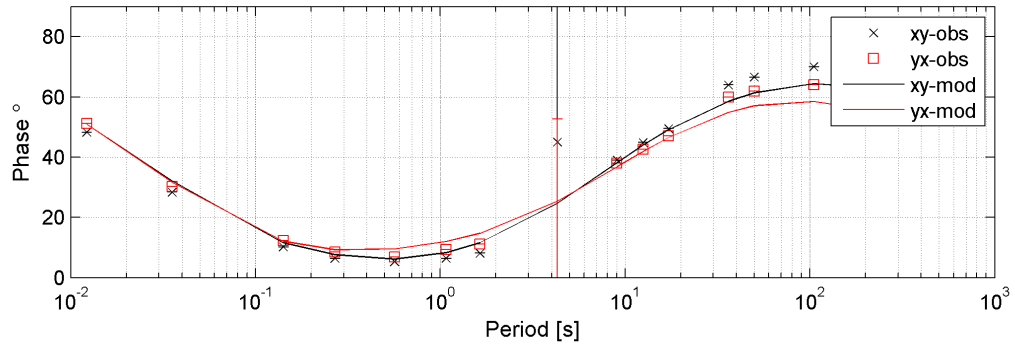
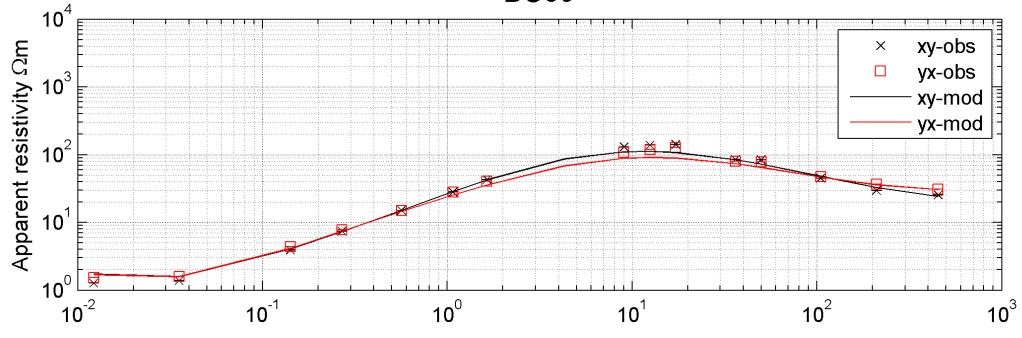


Model 2
BC08

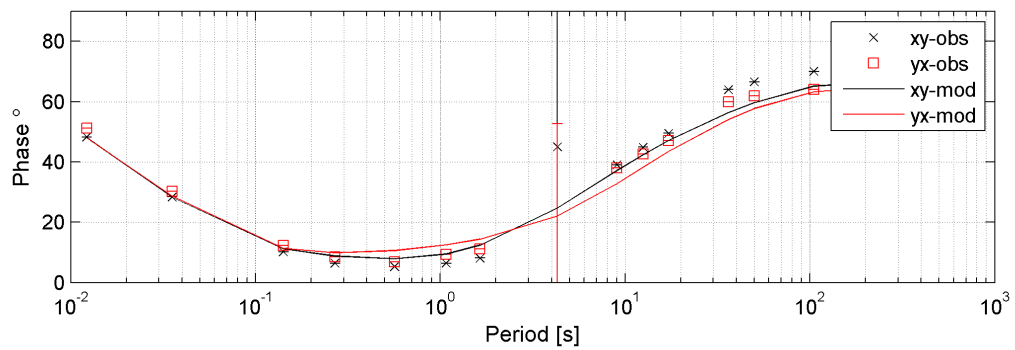
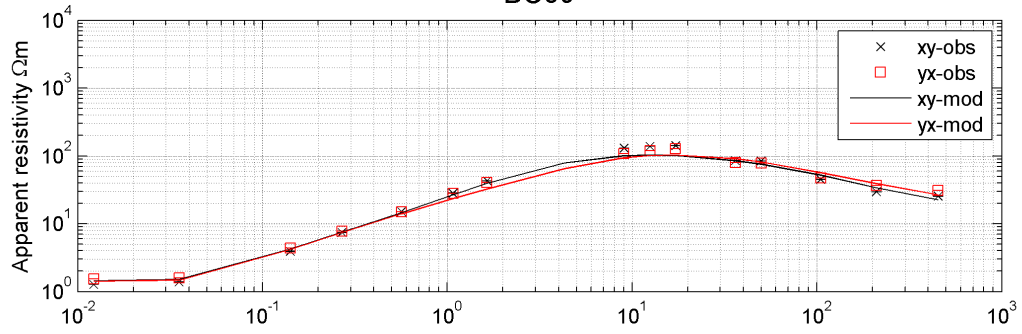


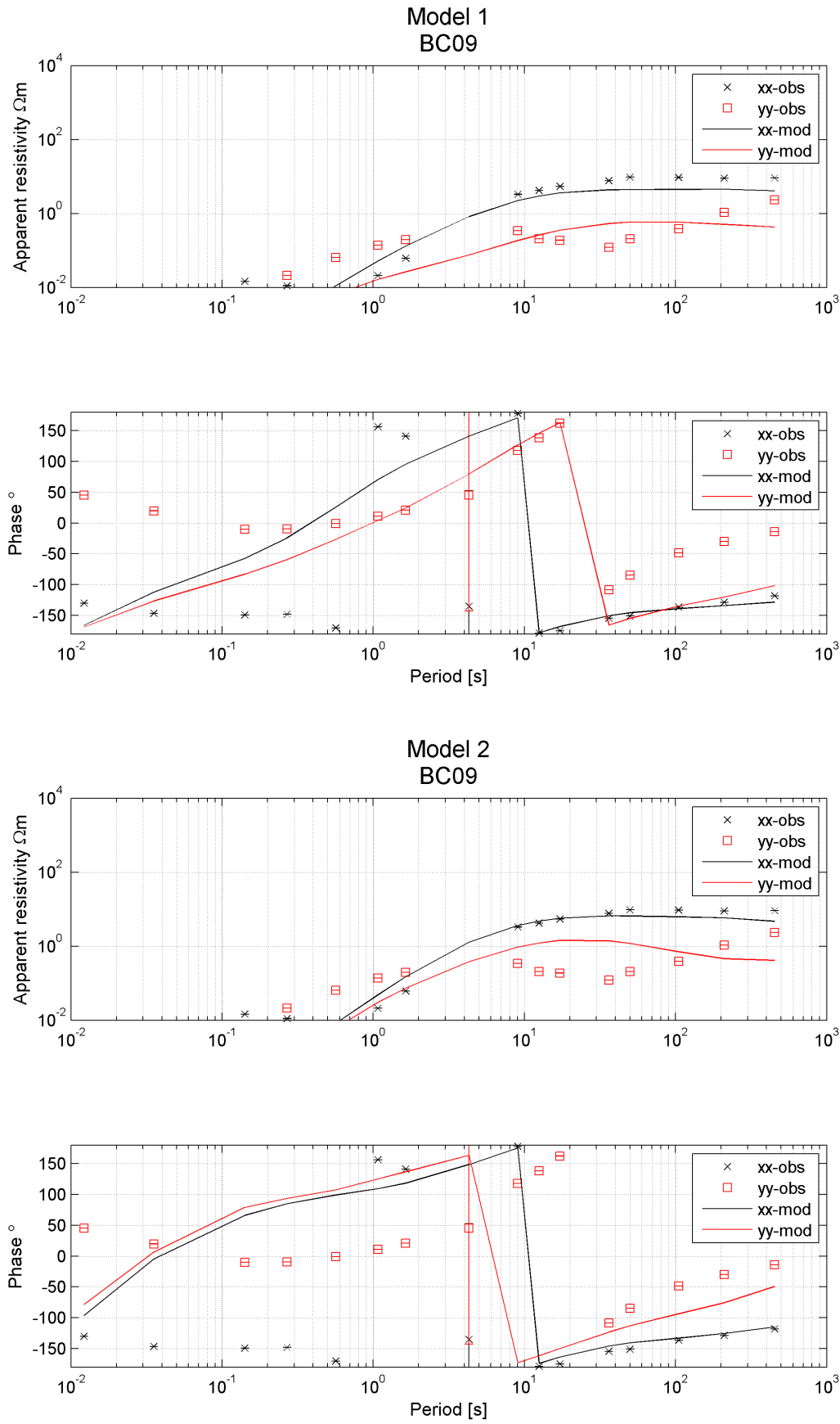


Model 1
BC09

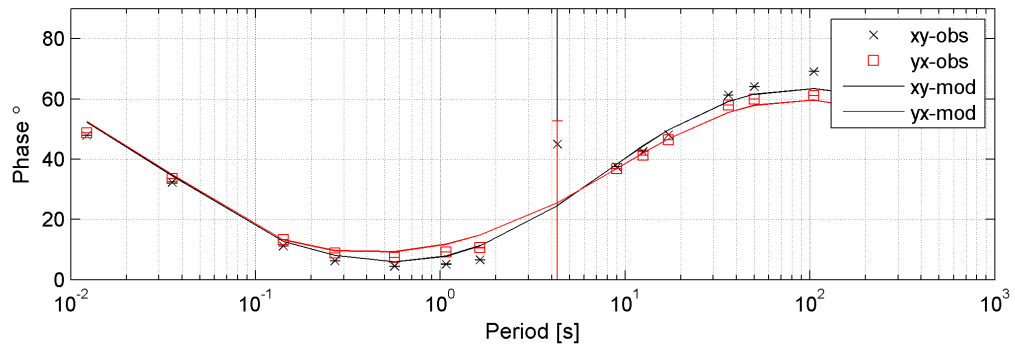
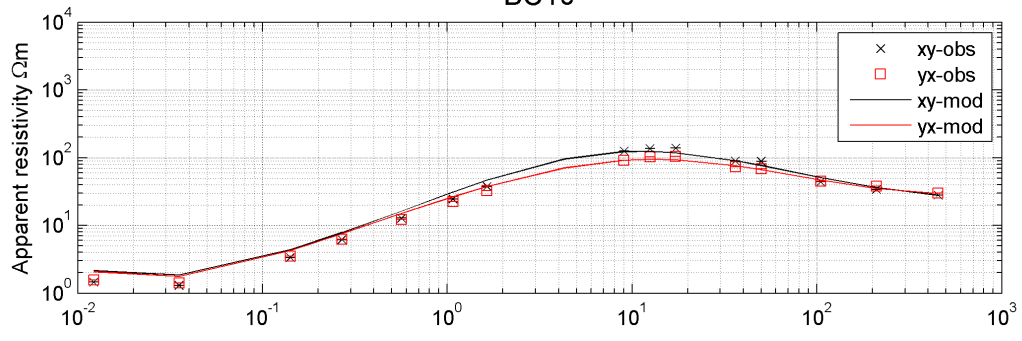


Model 2
BC09

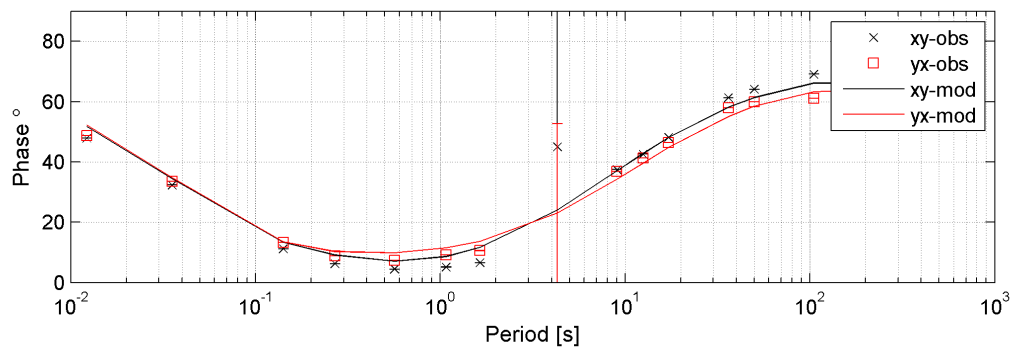
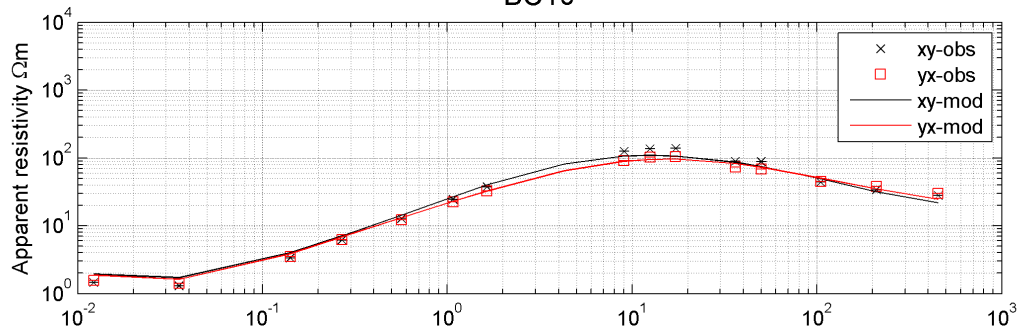


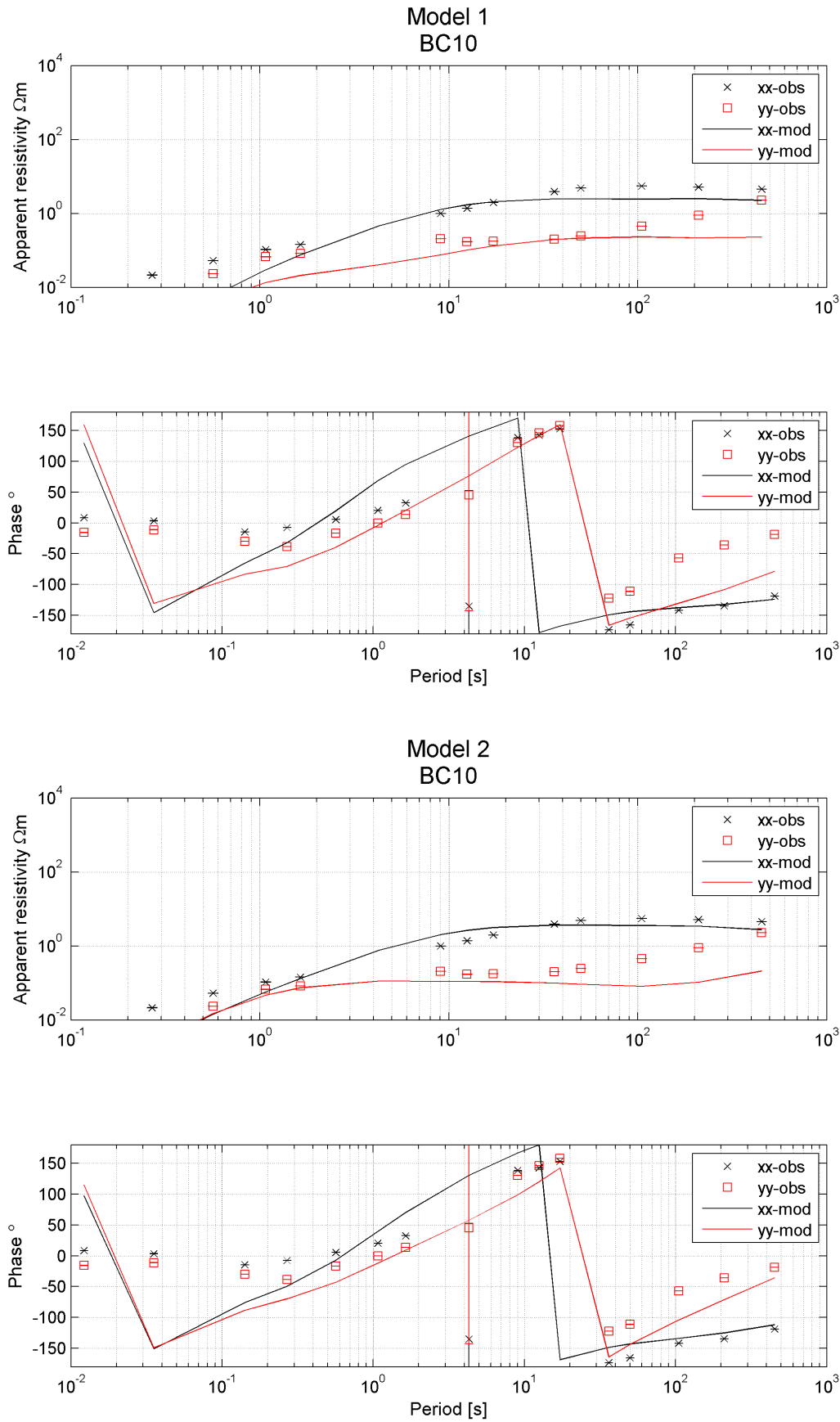


Model 1
BC10

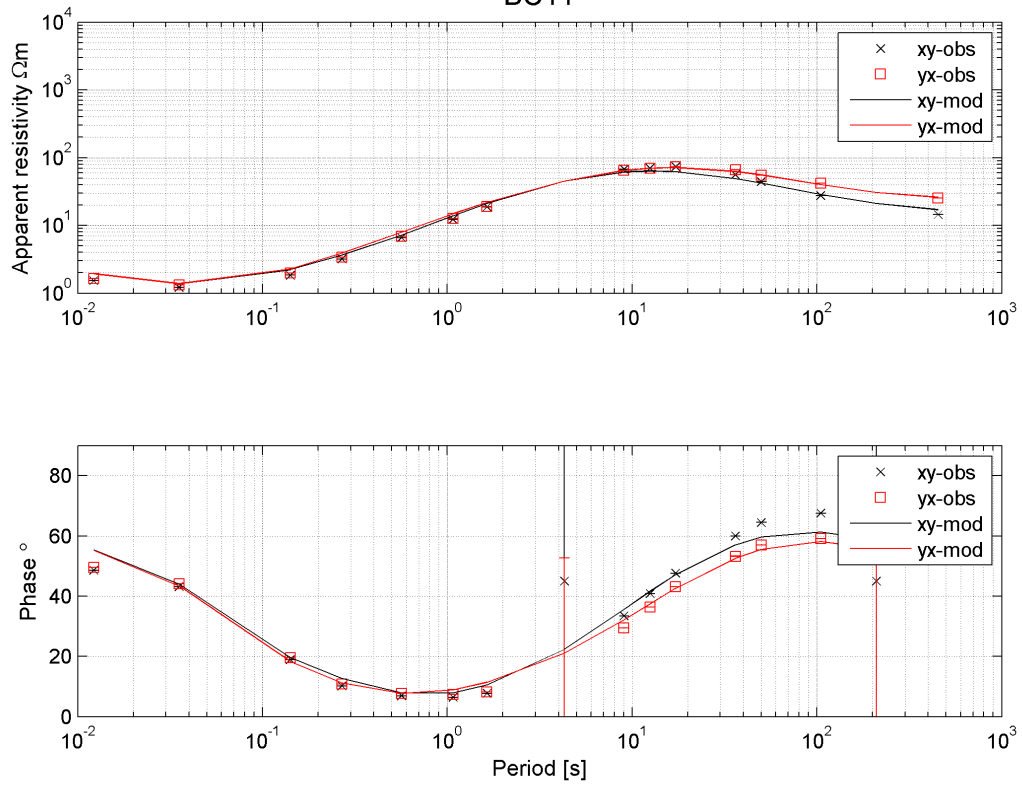


Model 2
BC10

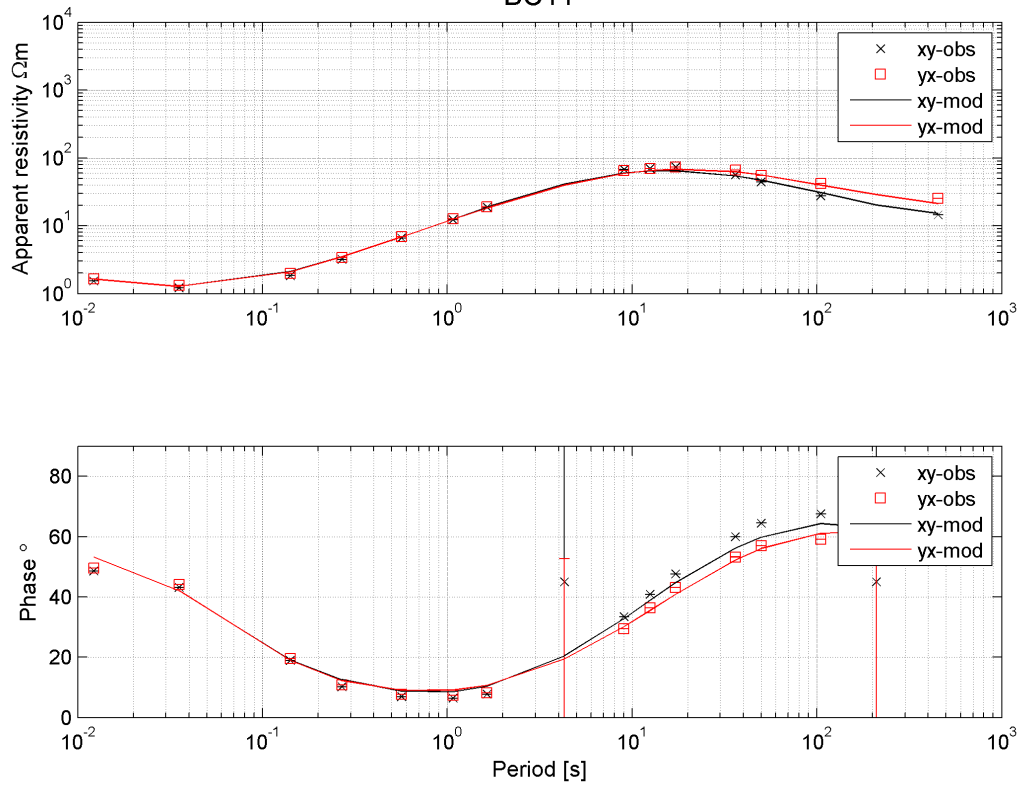


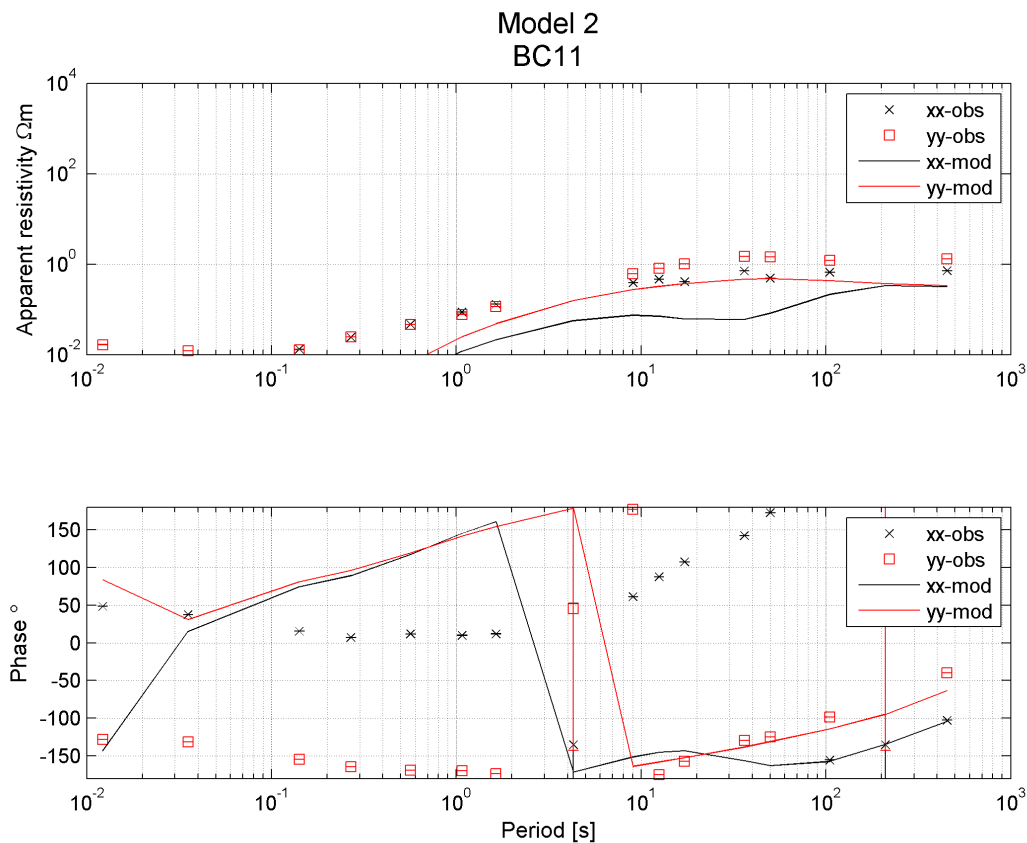
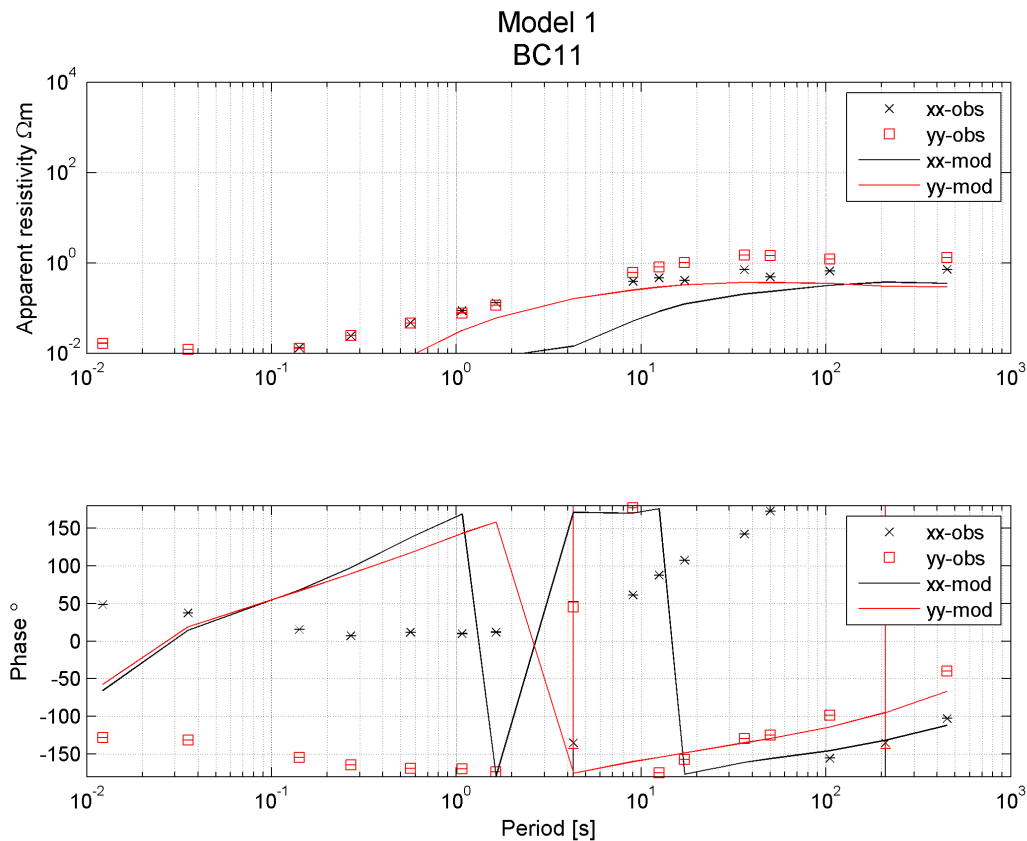


Model 1
BC11

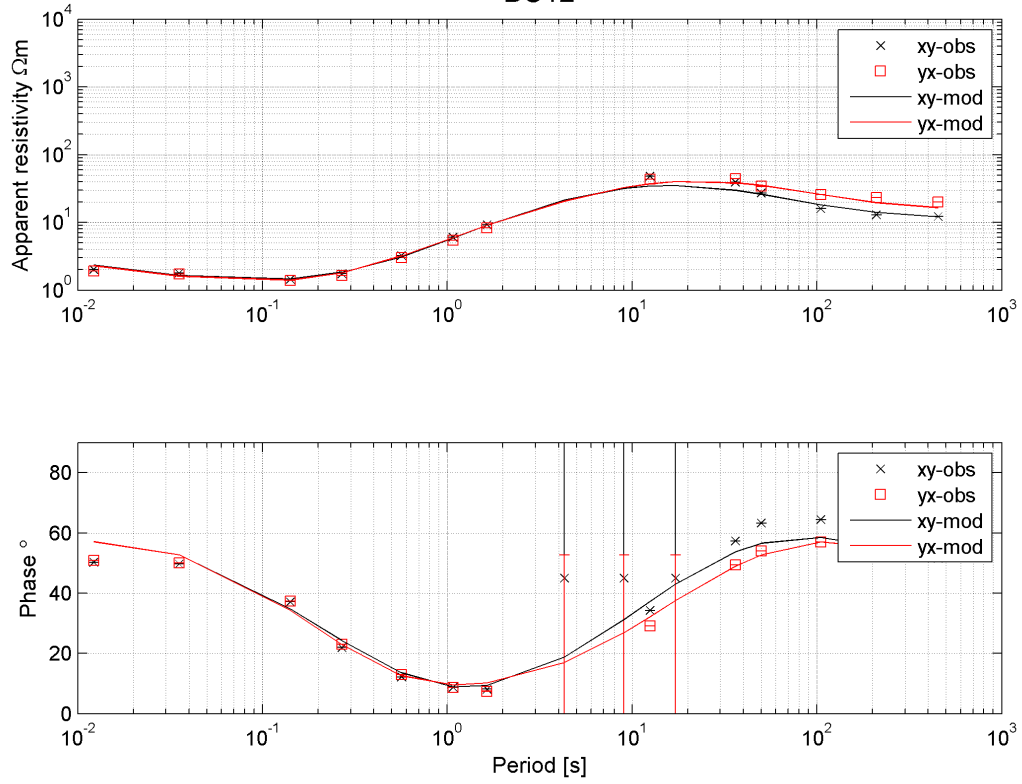


Model 2
BC11

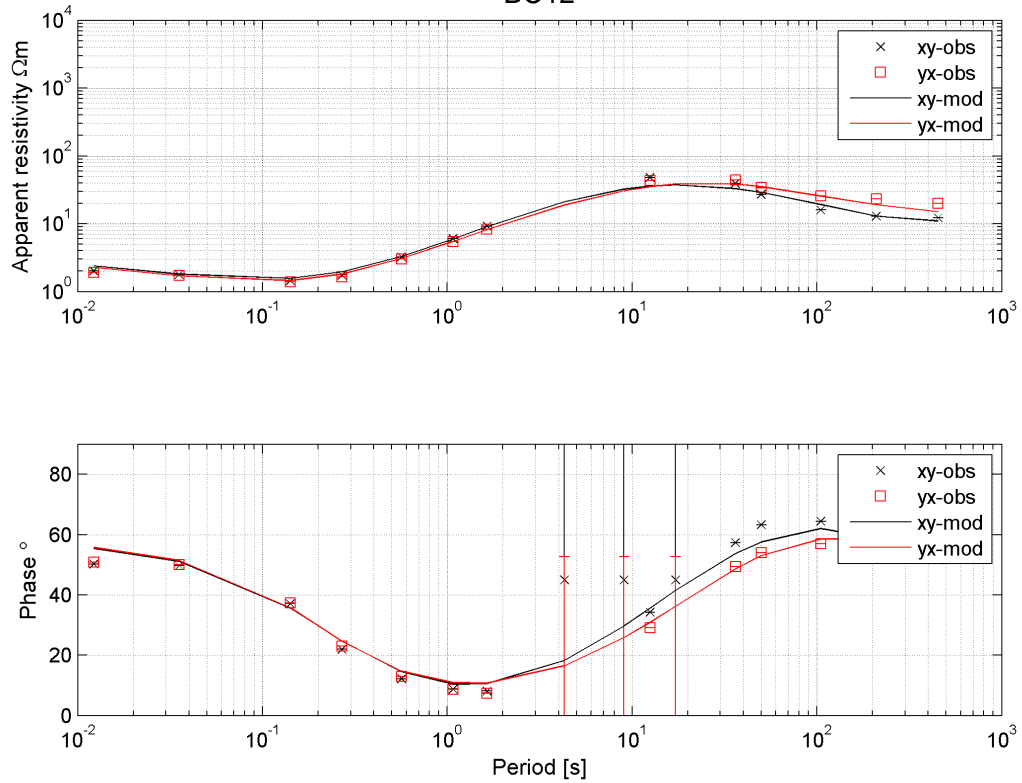


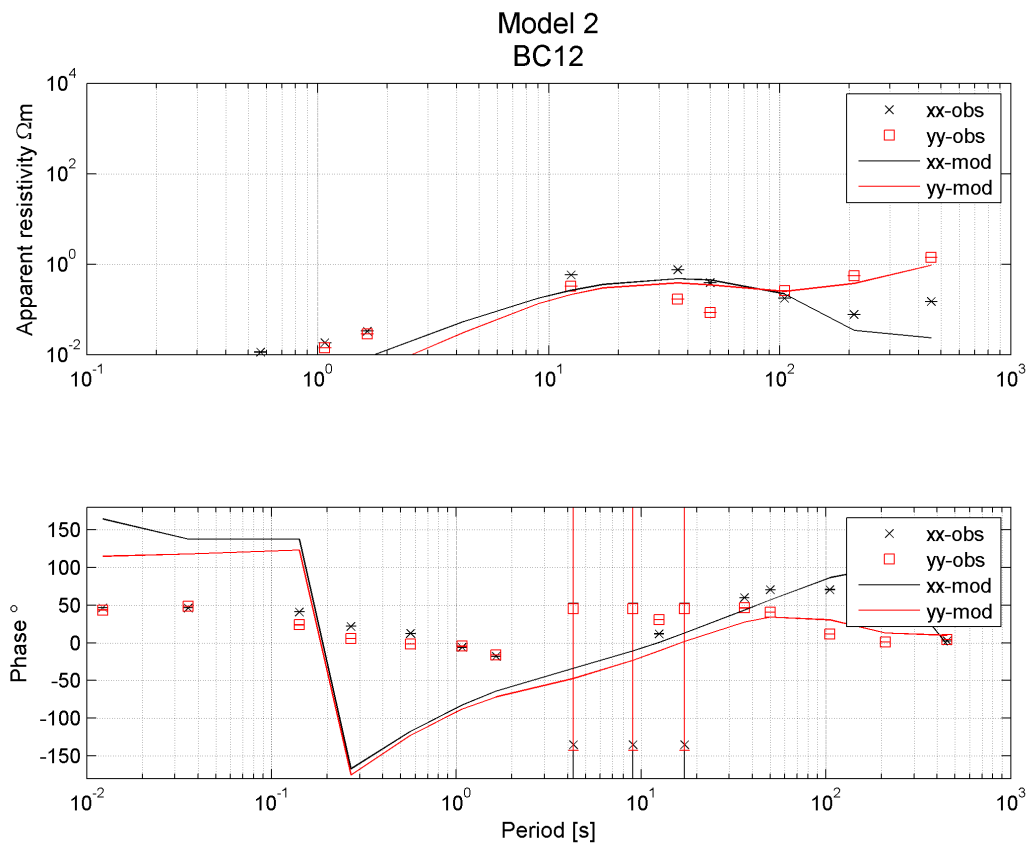
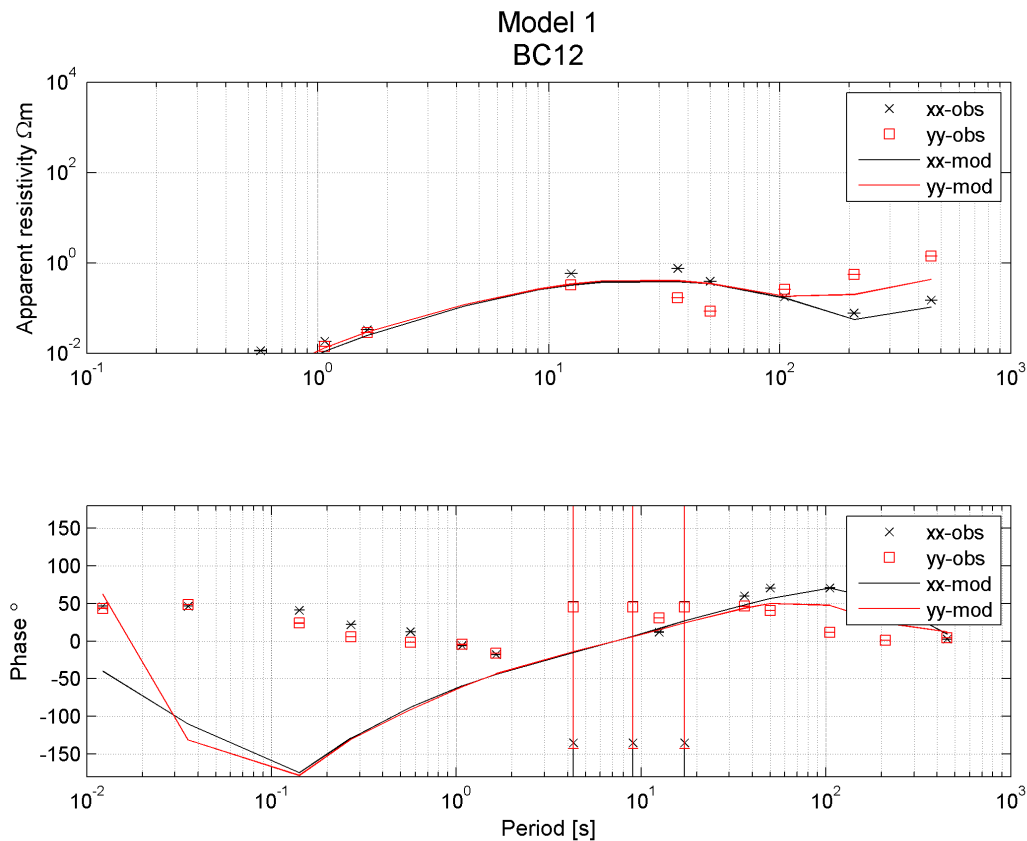


Model 1
BC12

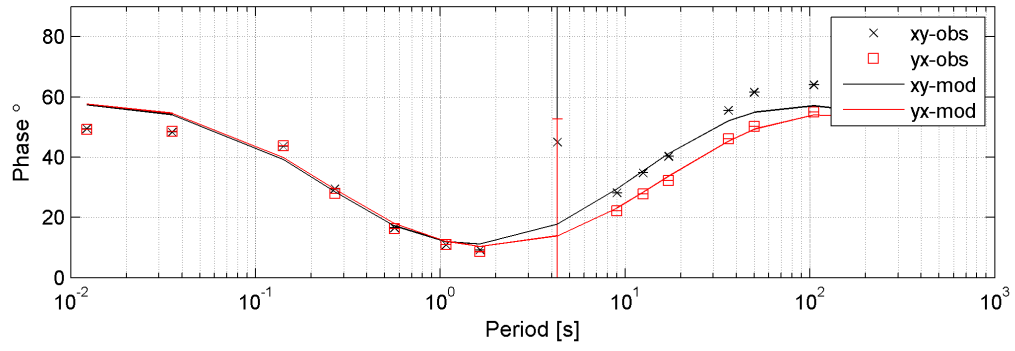
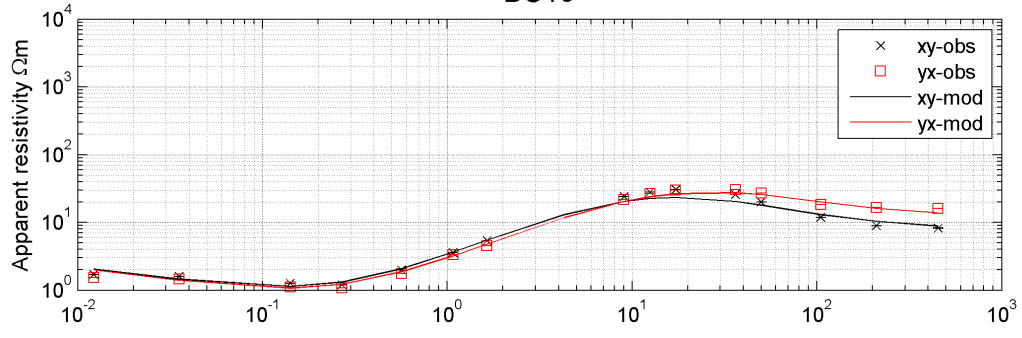


Model 2
BC12

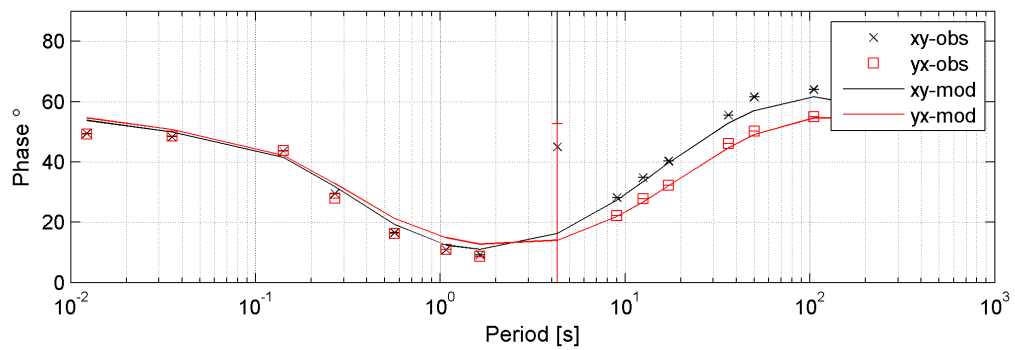
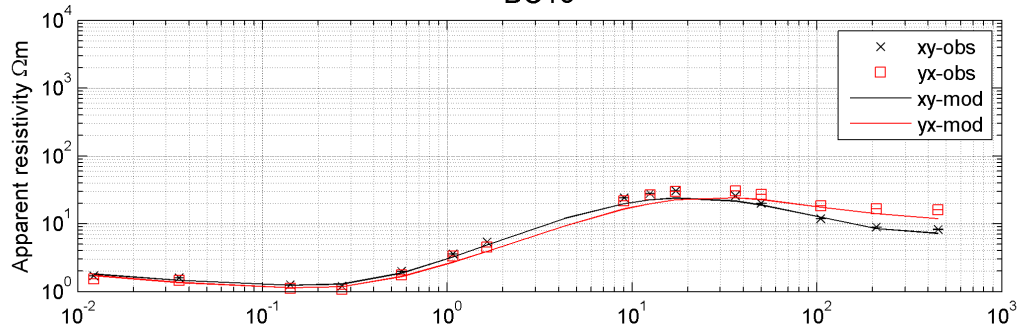


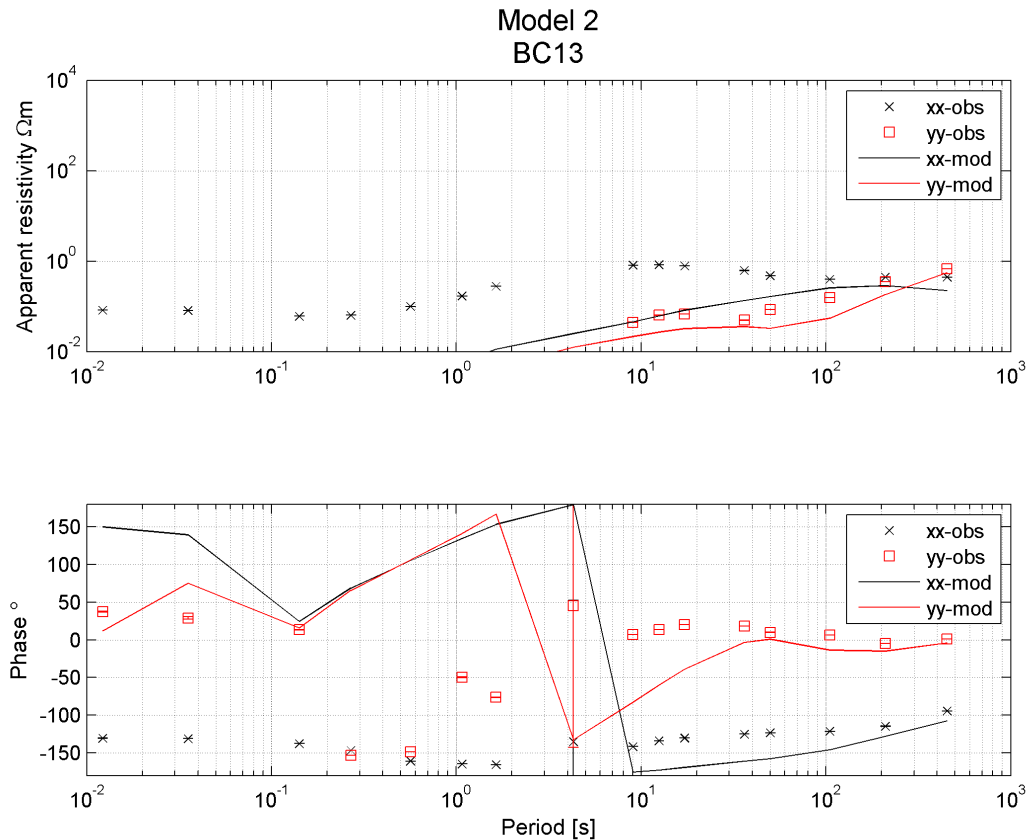
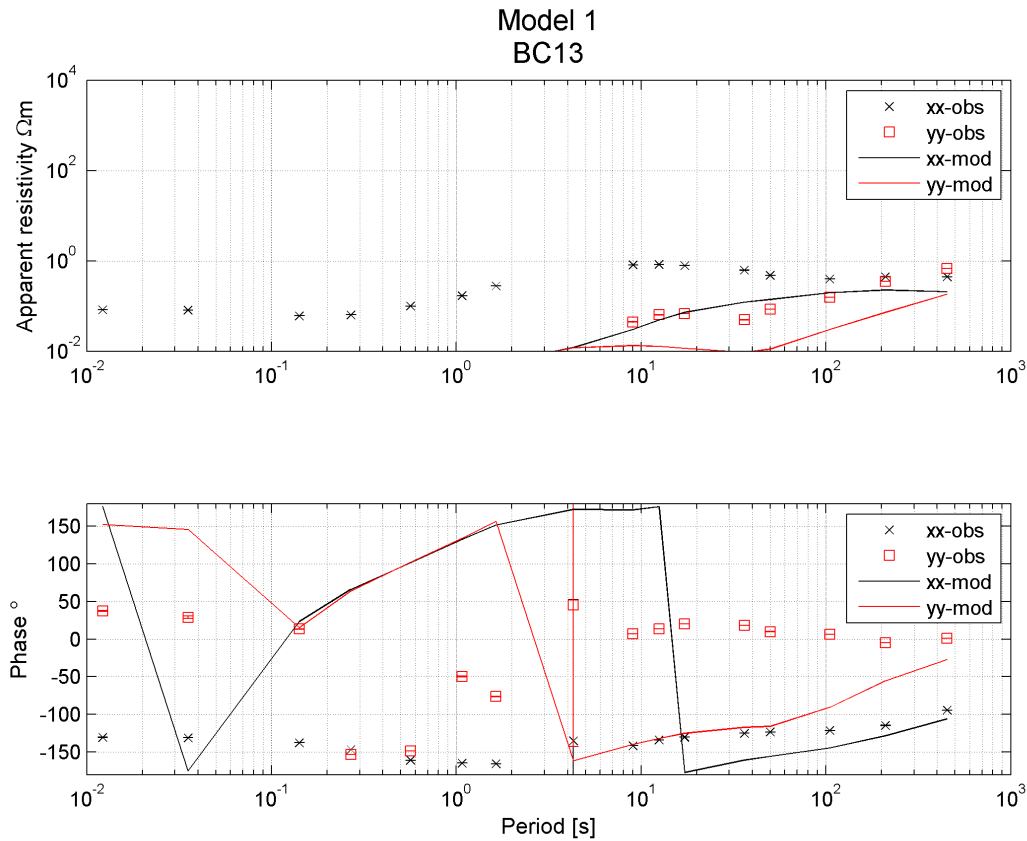


Model 1
BC13

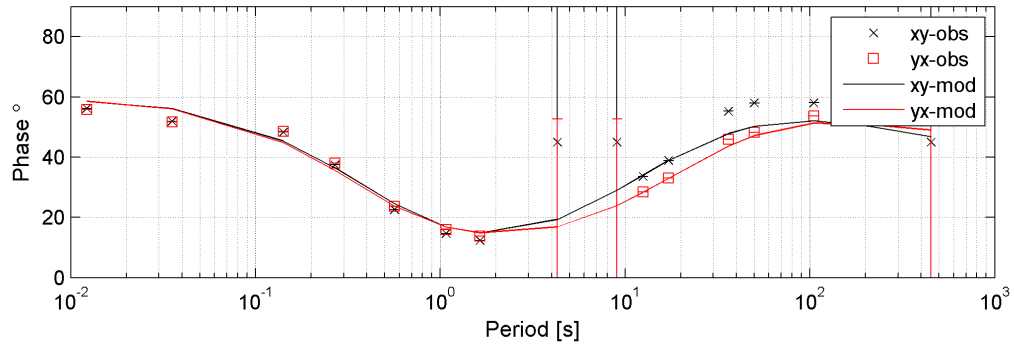
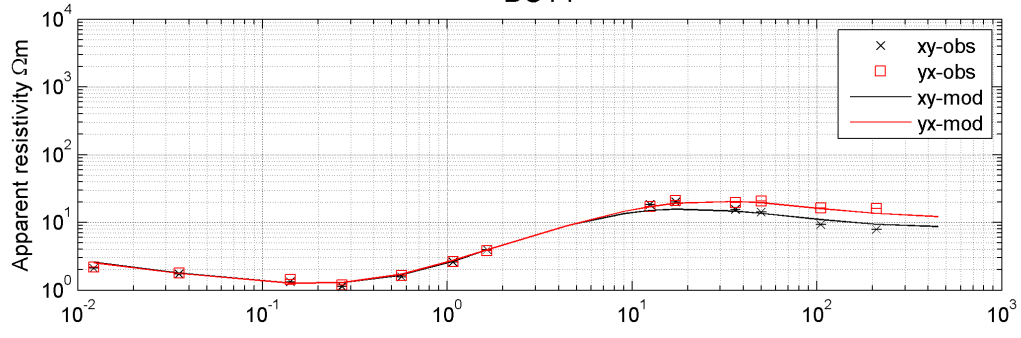


Model 2
BC13

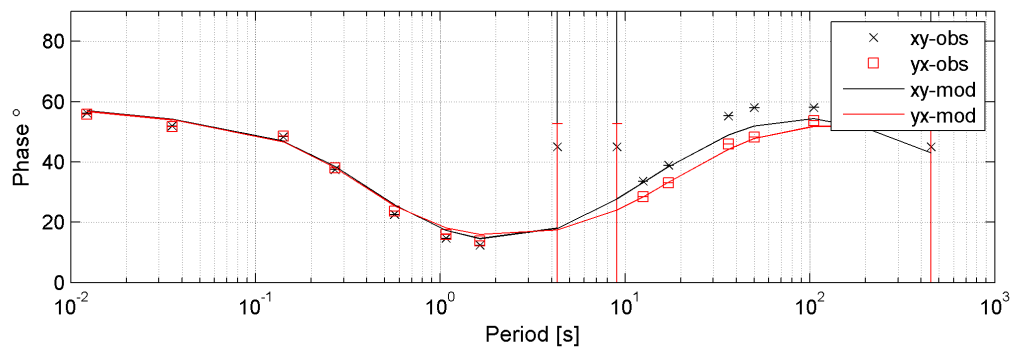
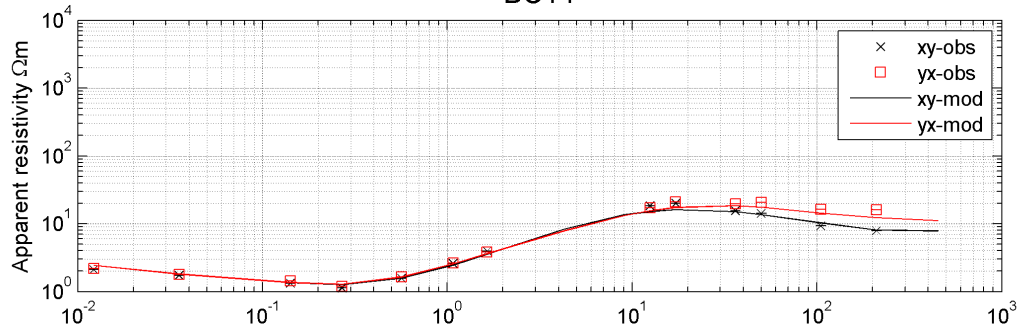


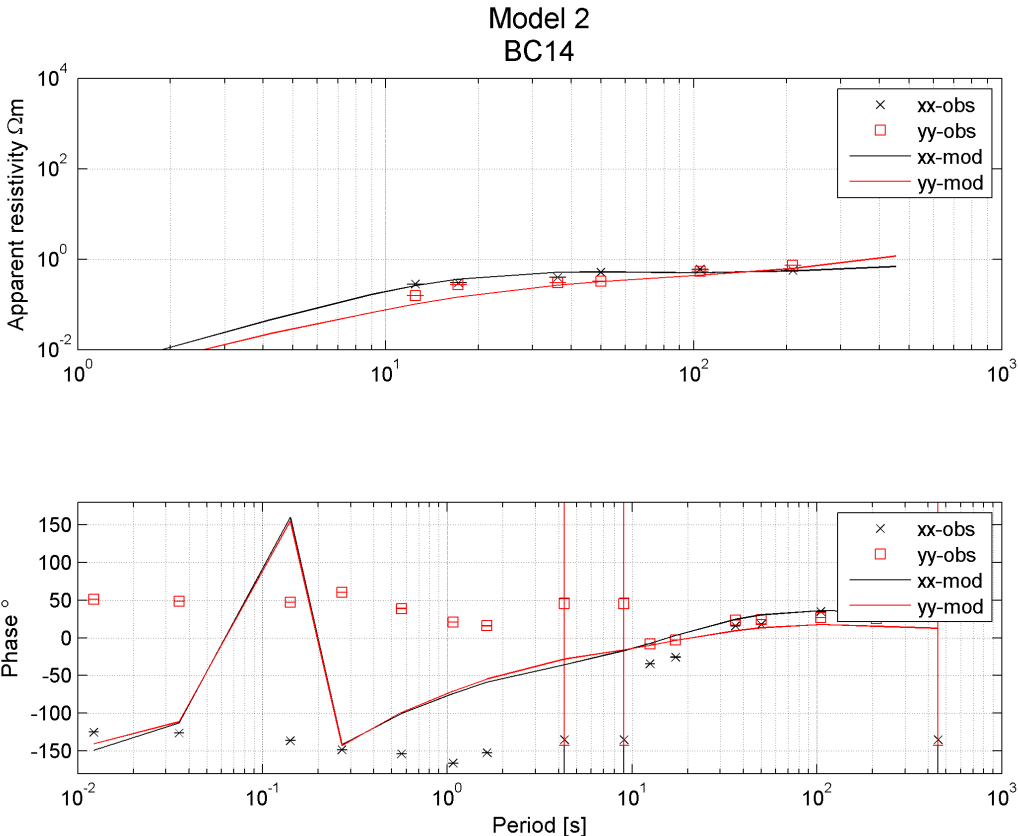
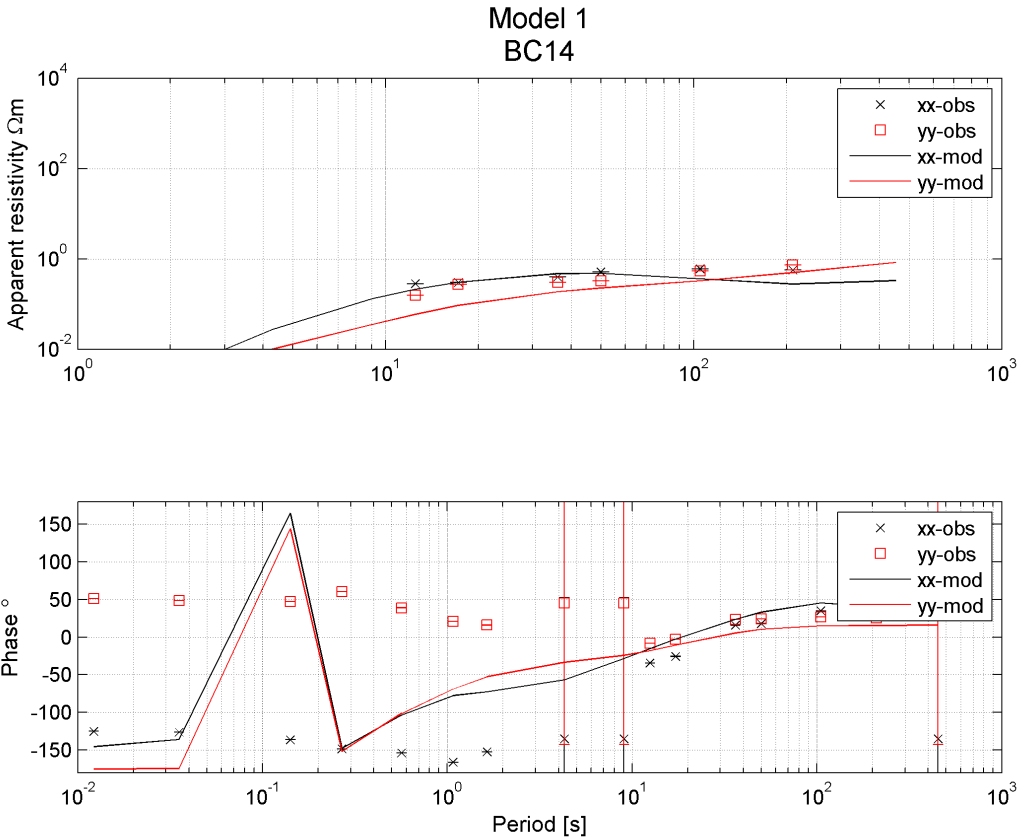


Model 1
BC14

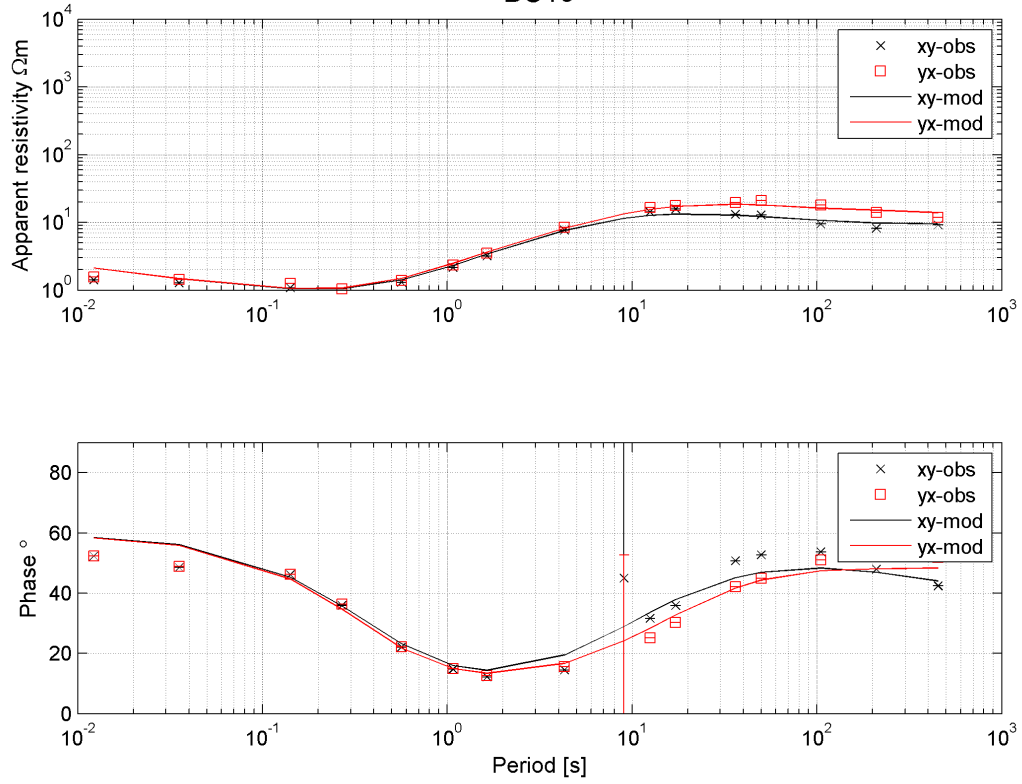


Model 2
BC14

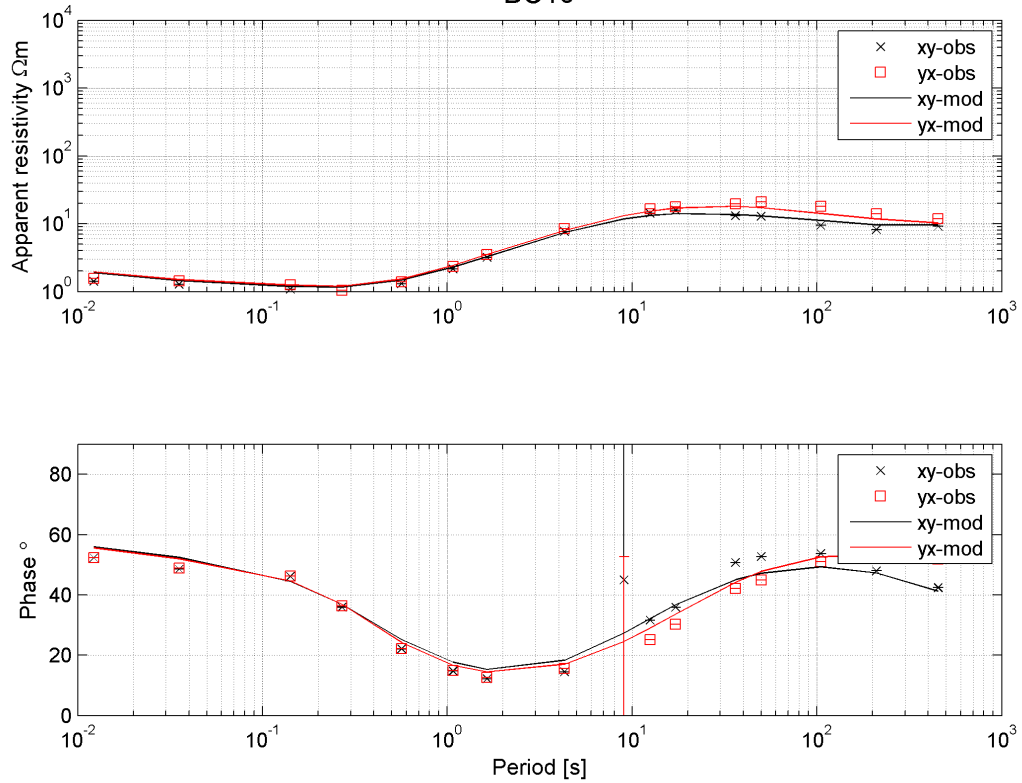


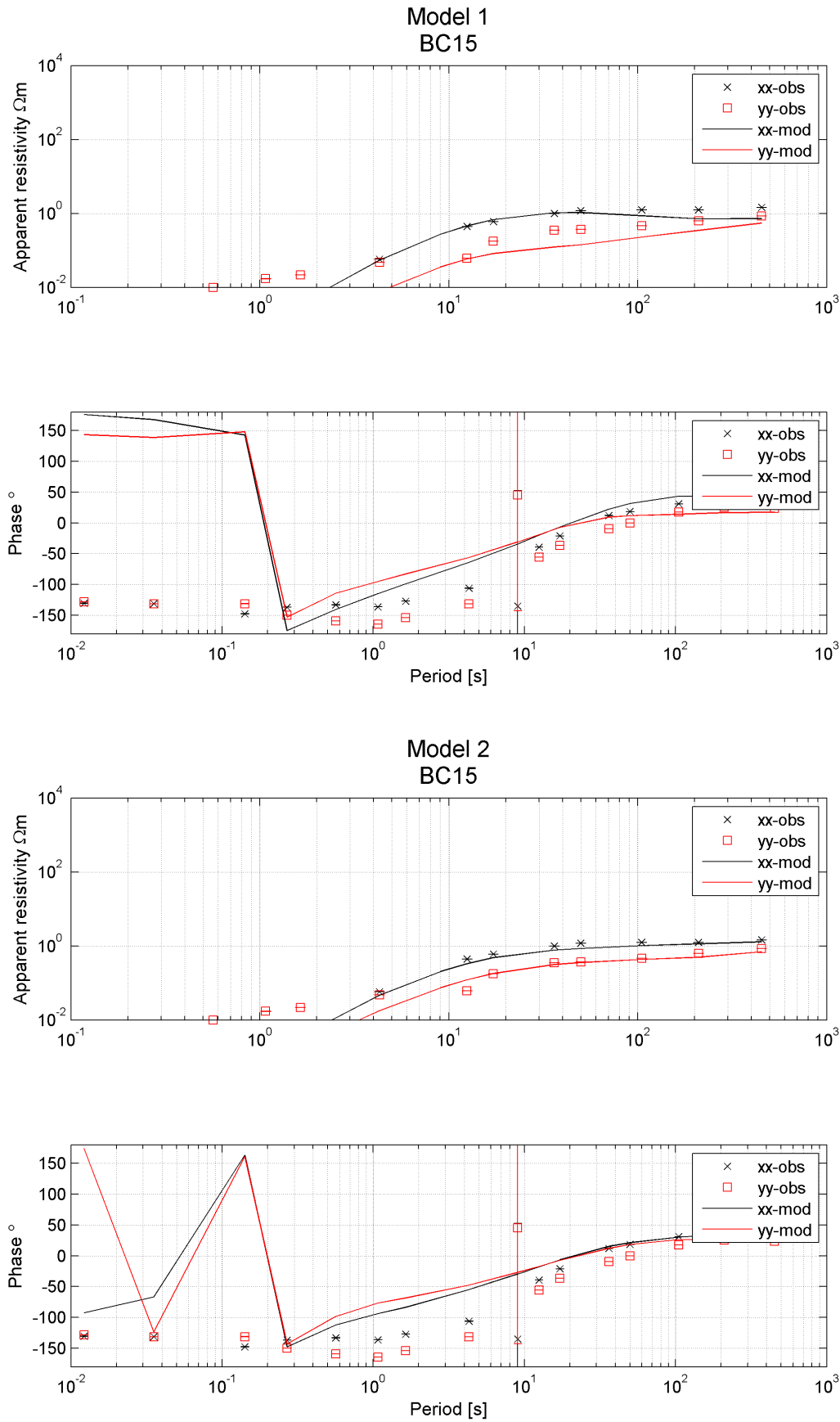


Model 1
BC15

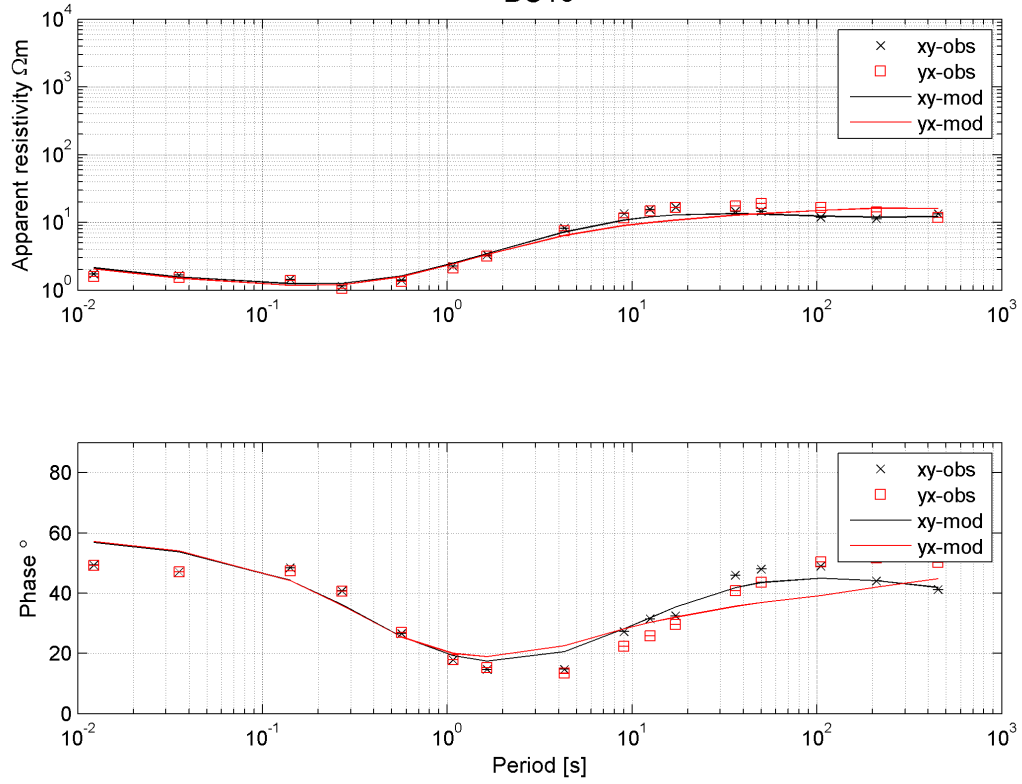


Model 2
BC15

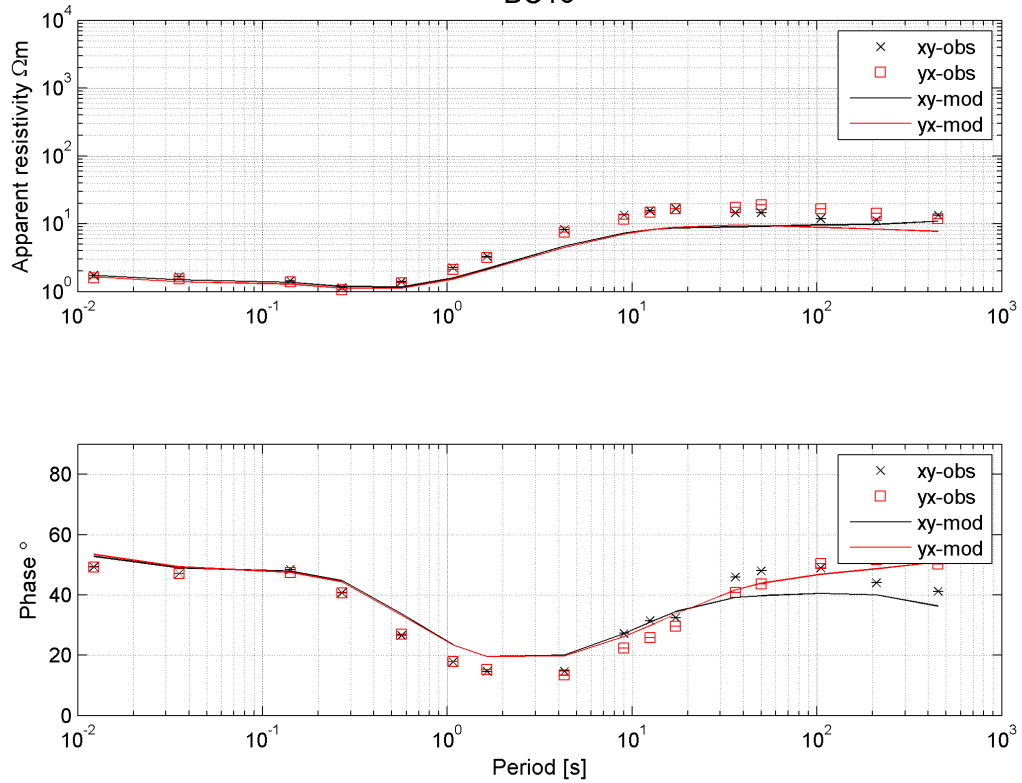


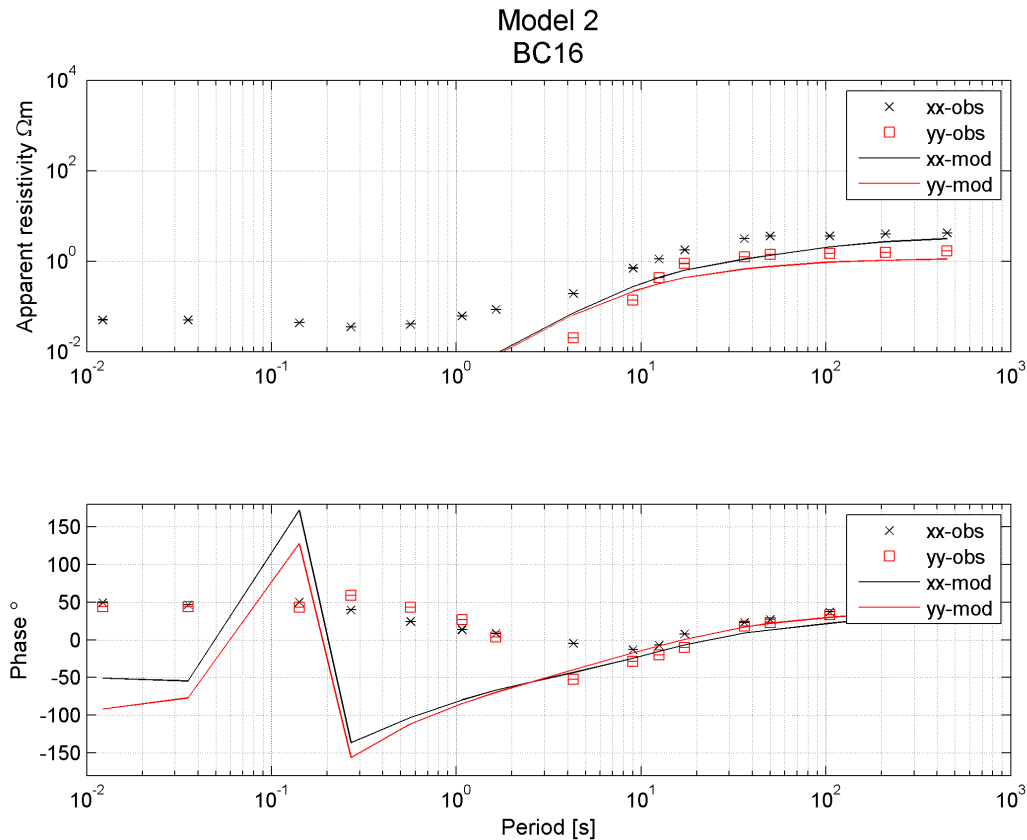
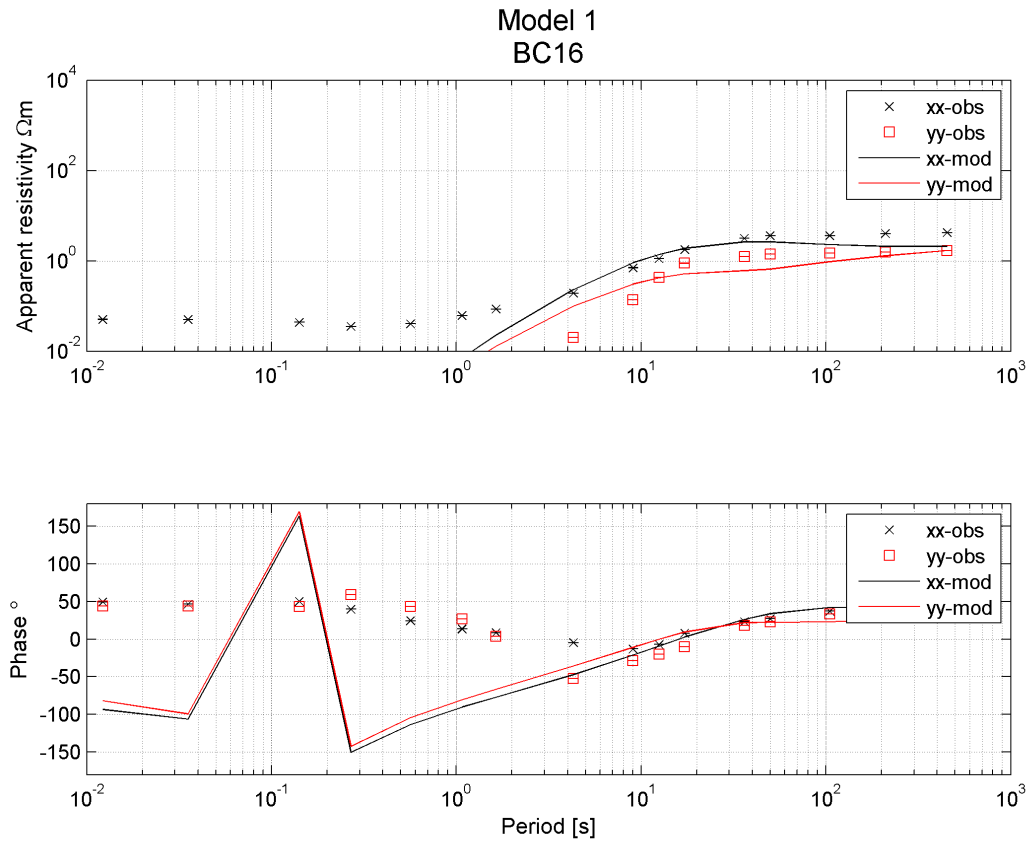


Model 1
BC16

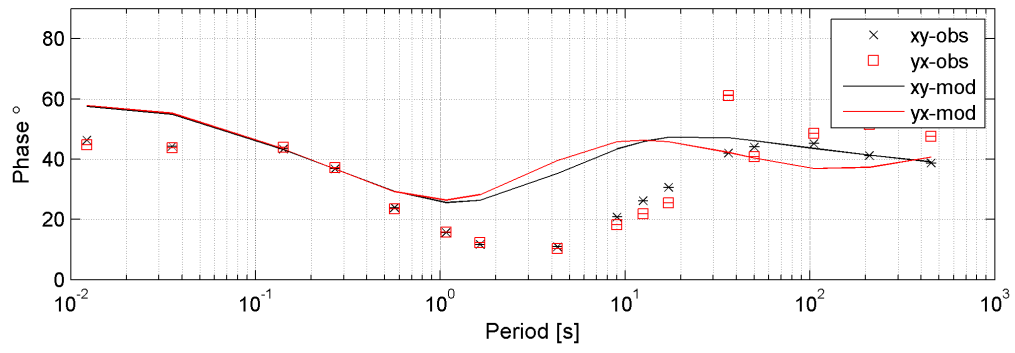
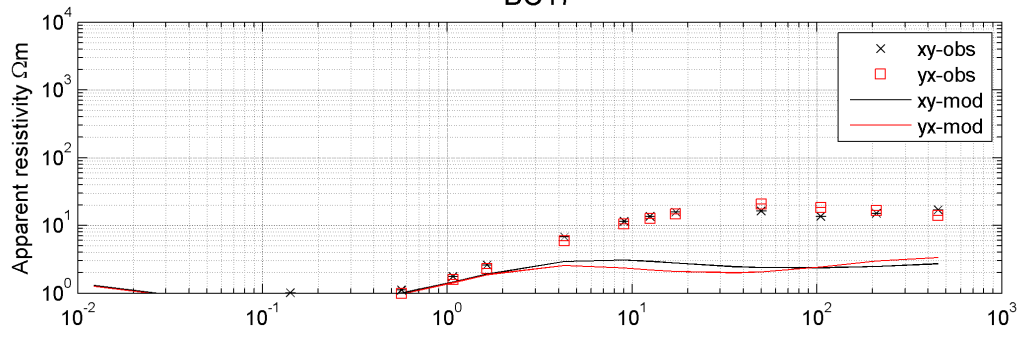


Model 2
BC16

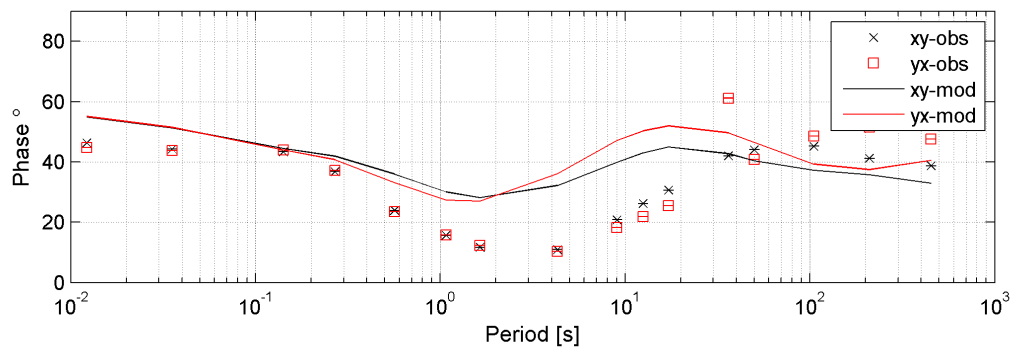
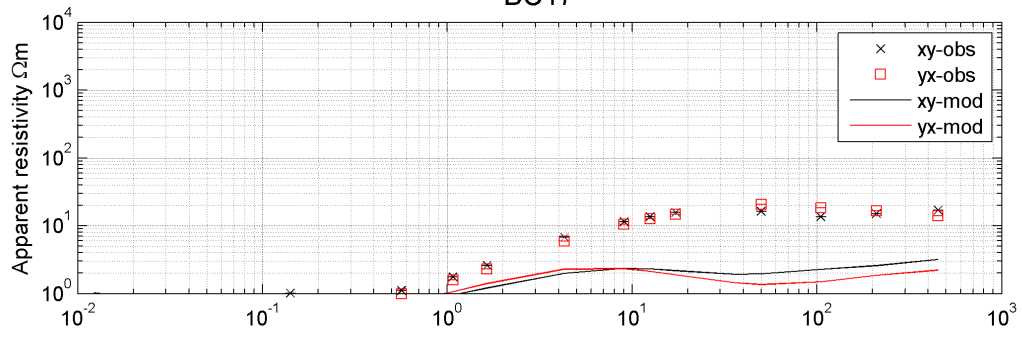


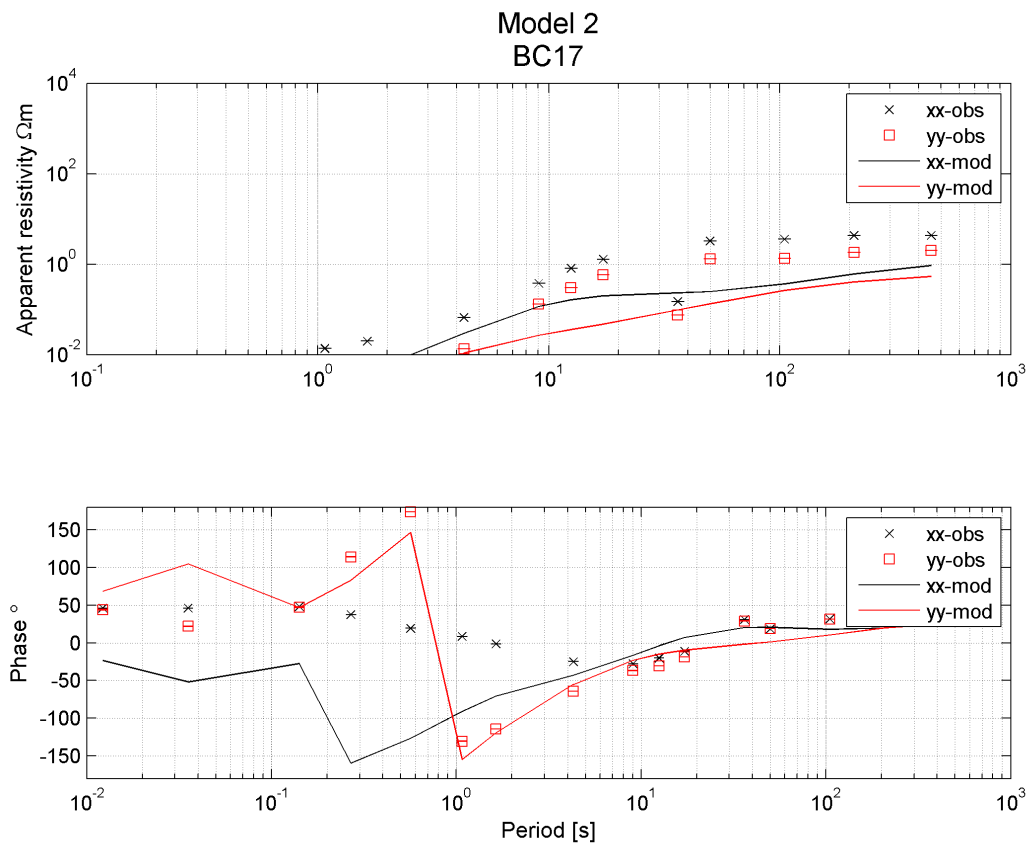
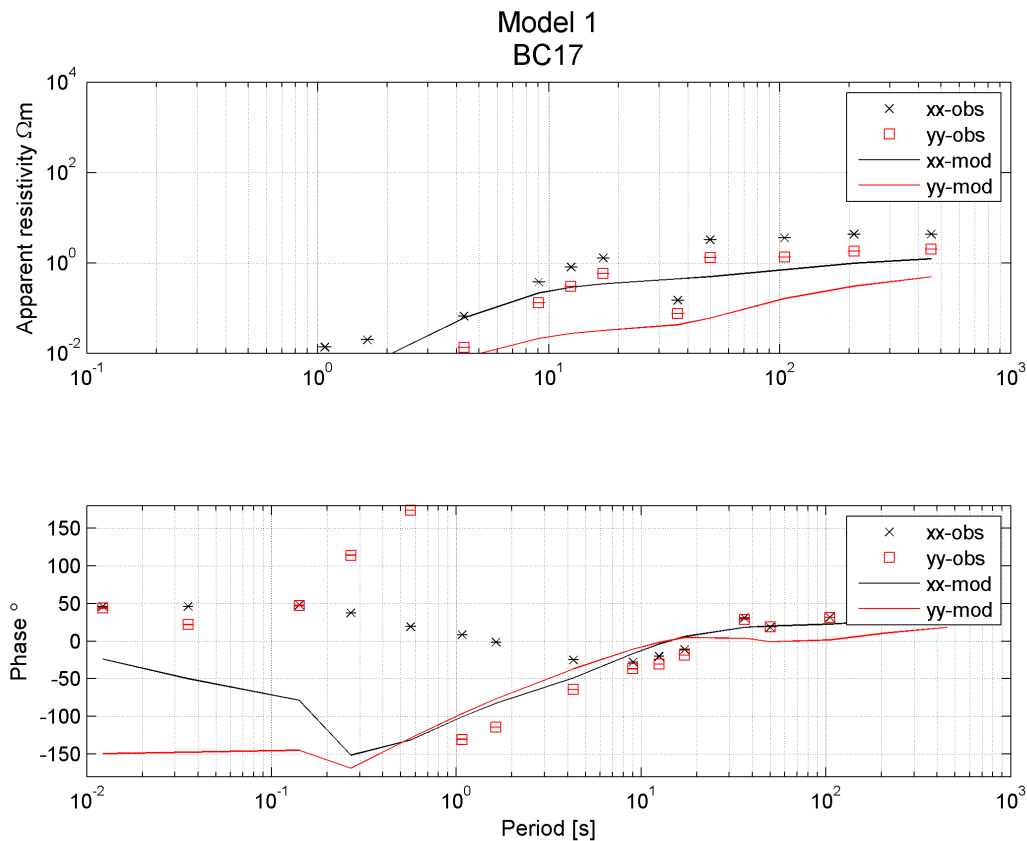


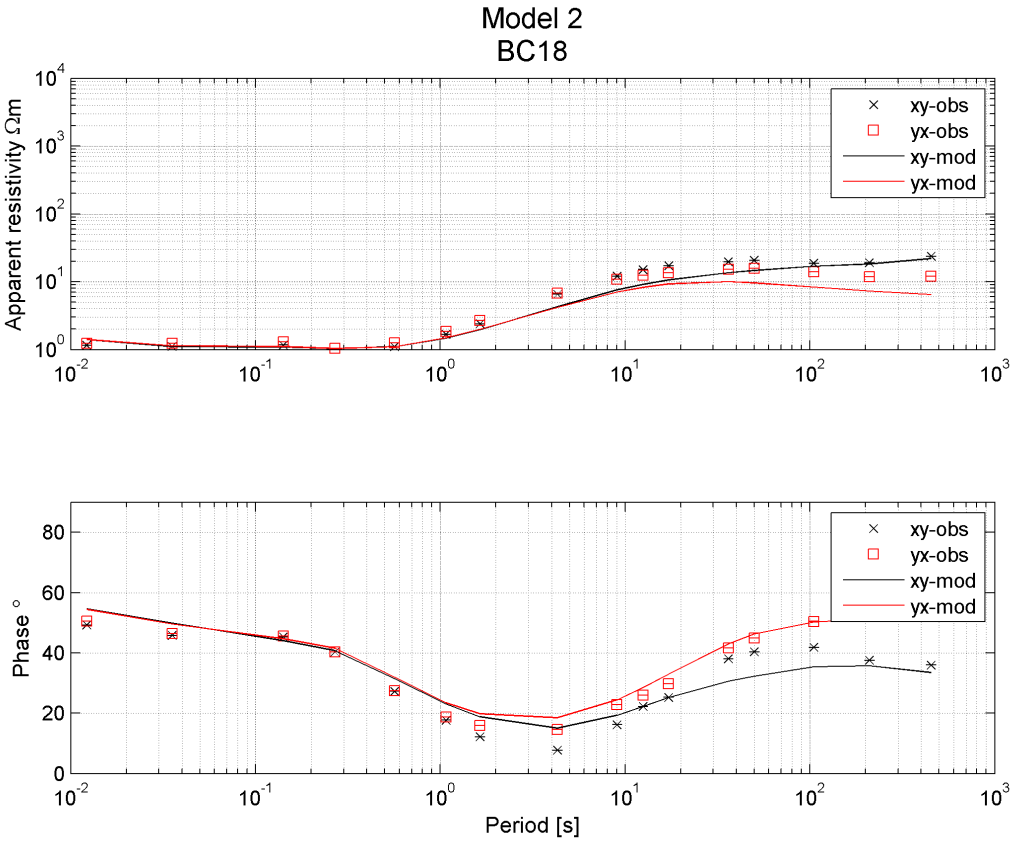
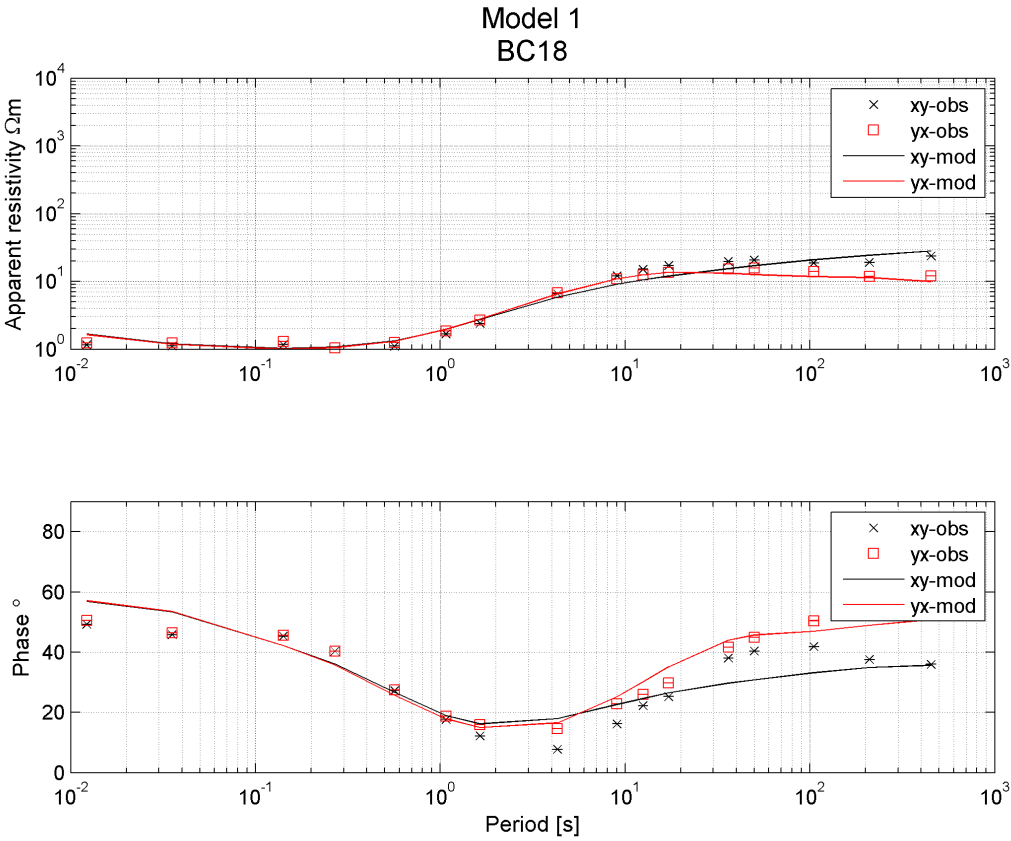
Model 1
BC17

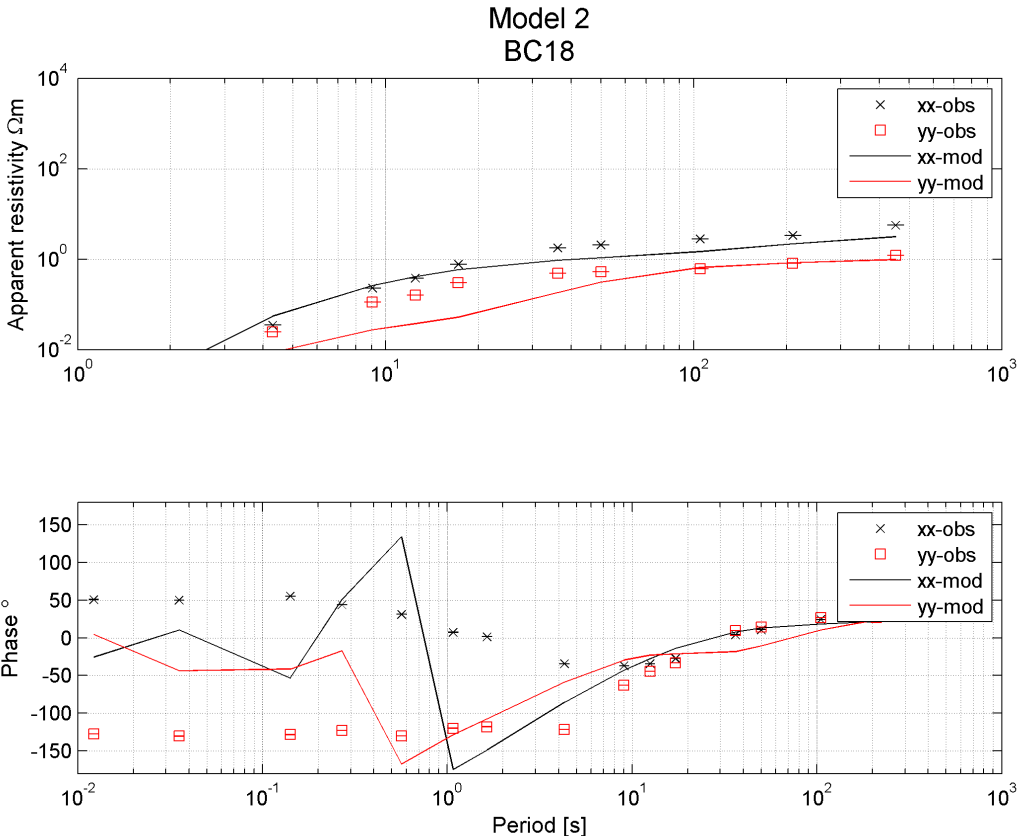
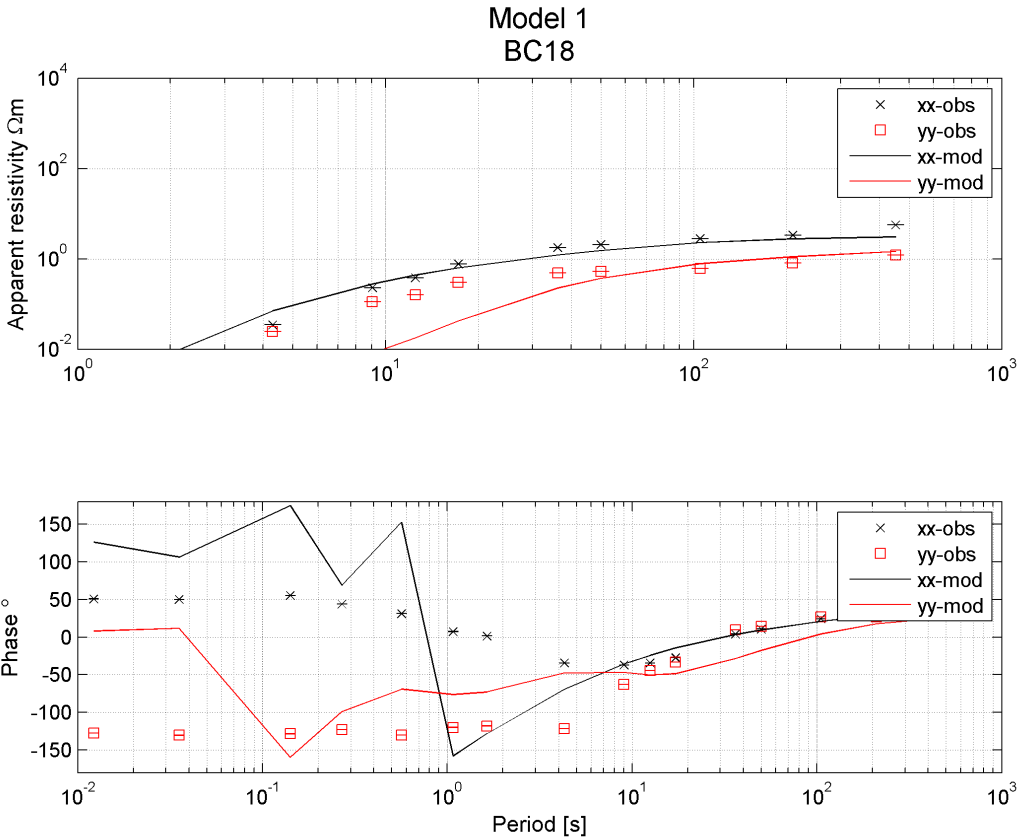


Model 2
BC17

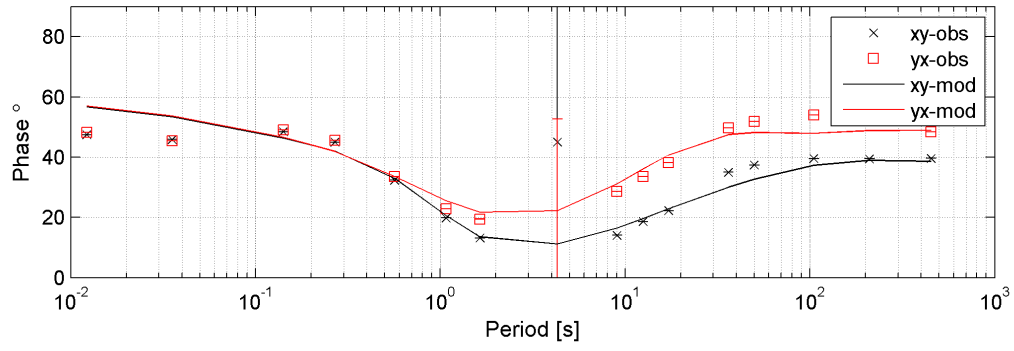
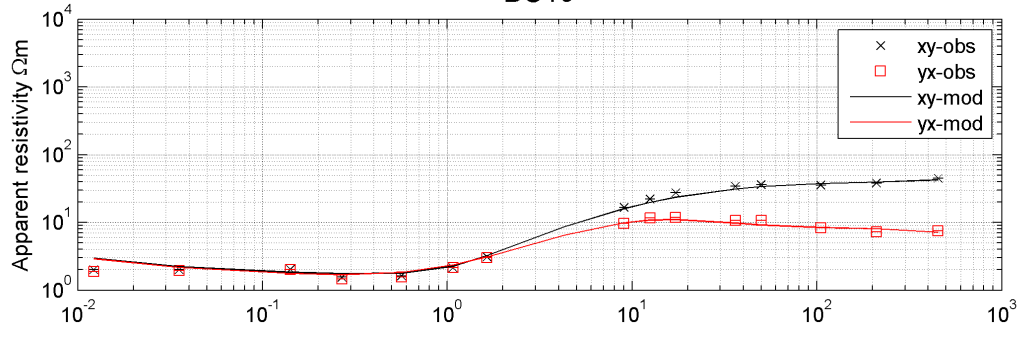




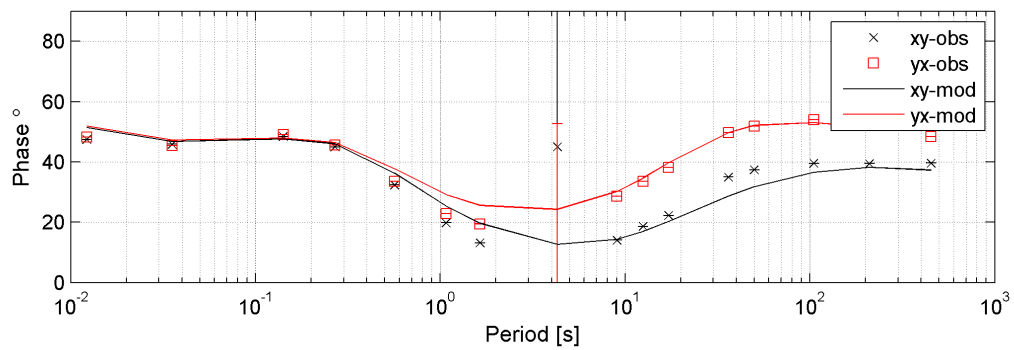
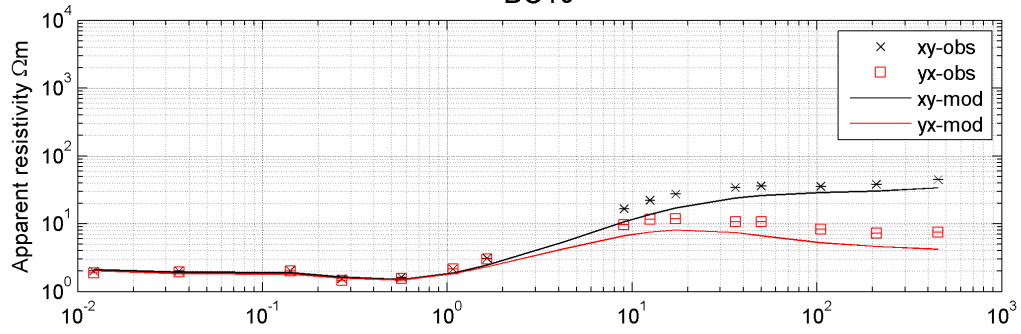


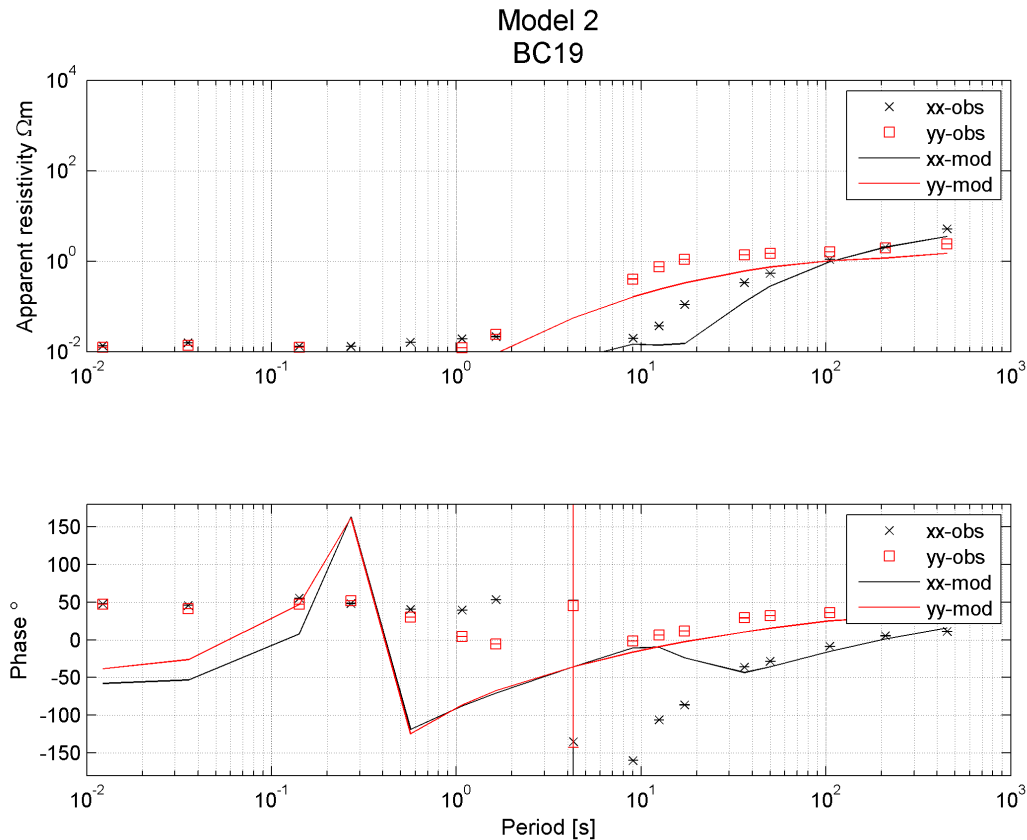
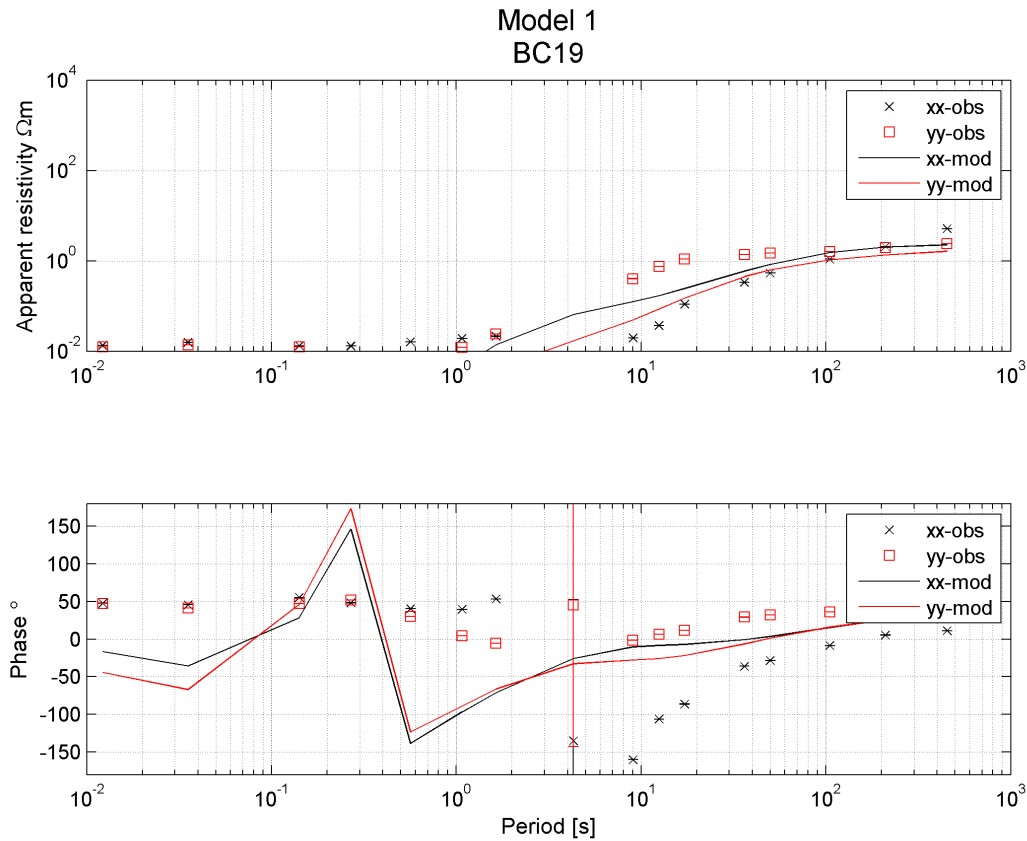


Model 1
BC19

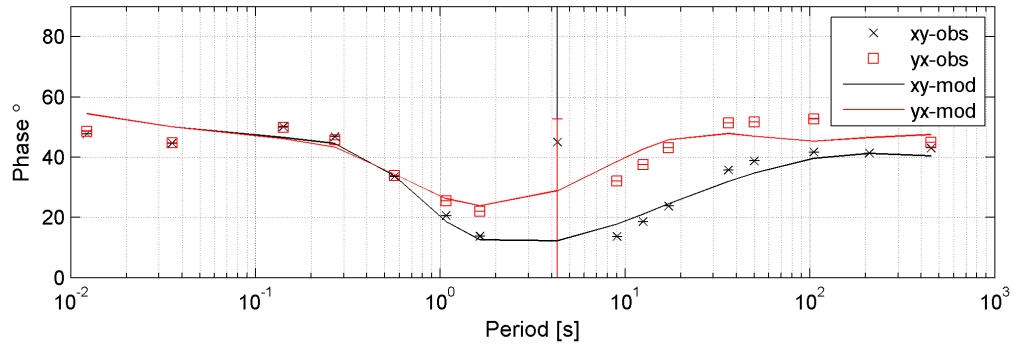
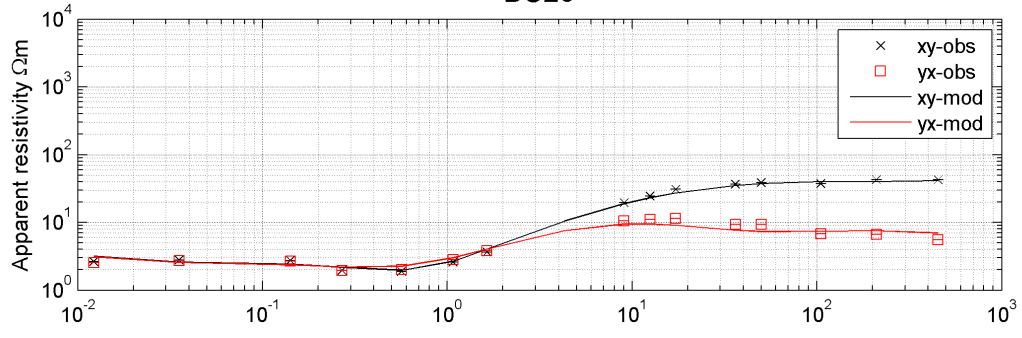


Model 2
BC19

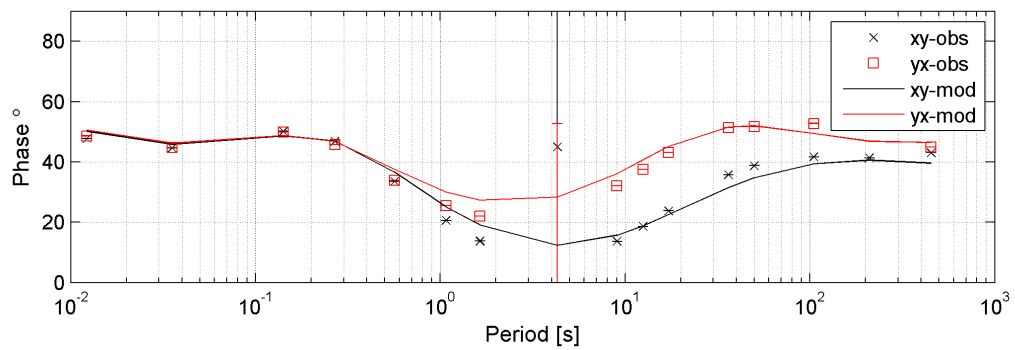
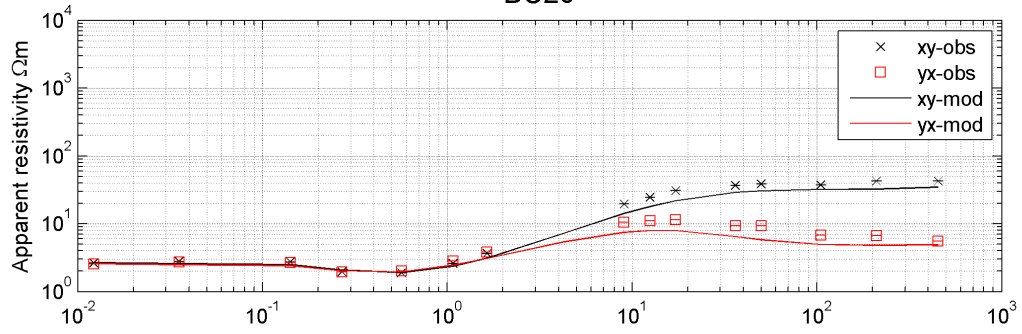


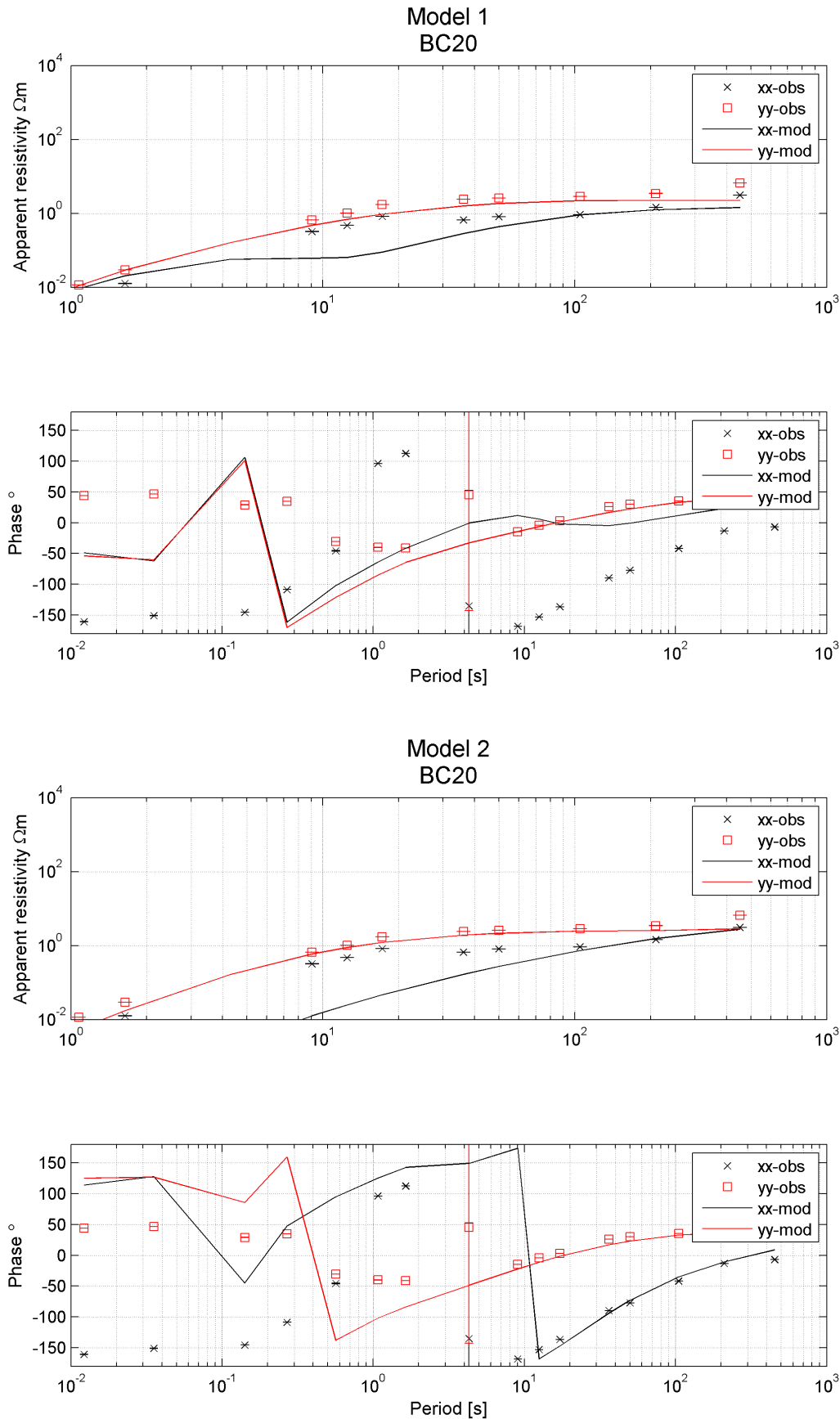


Model 1
BC20

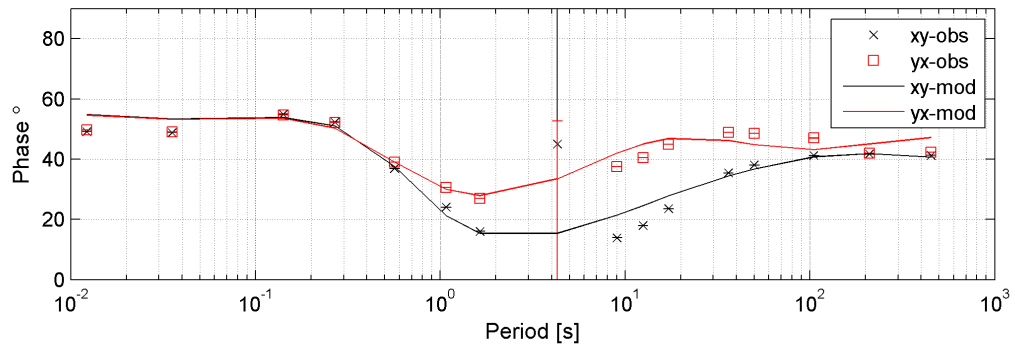
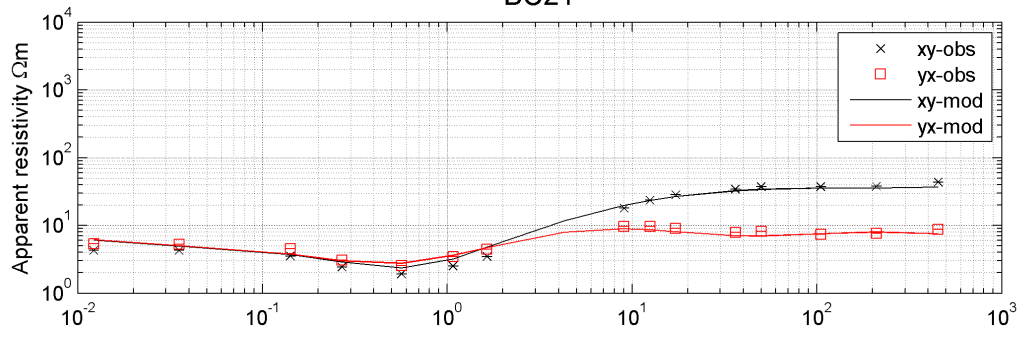


Model 2
BC20

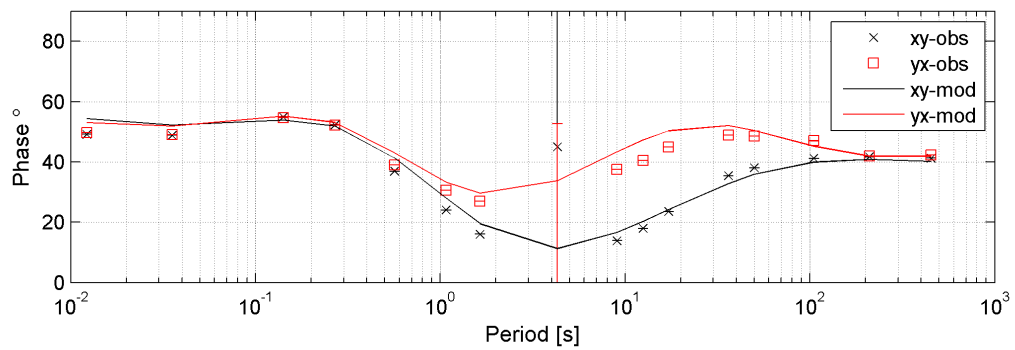
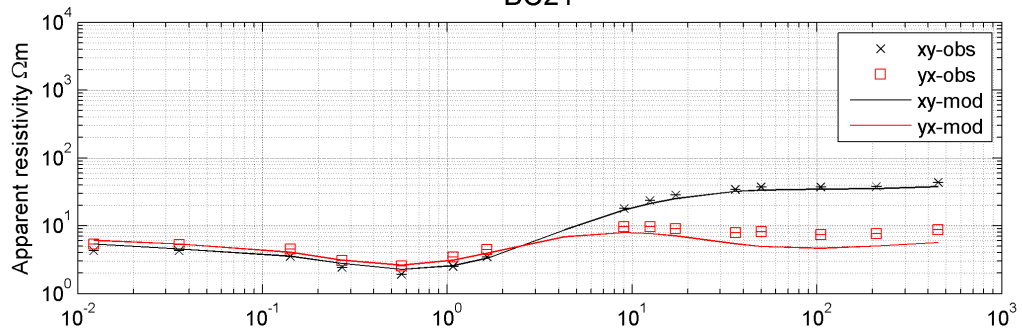


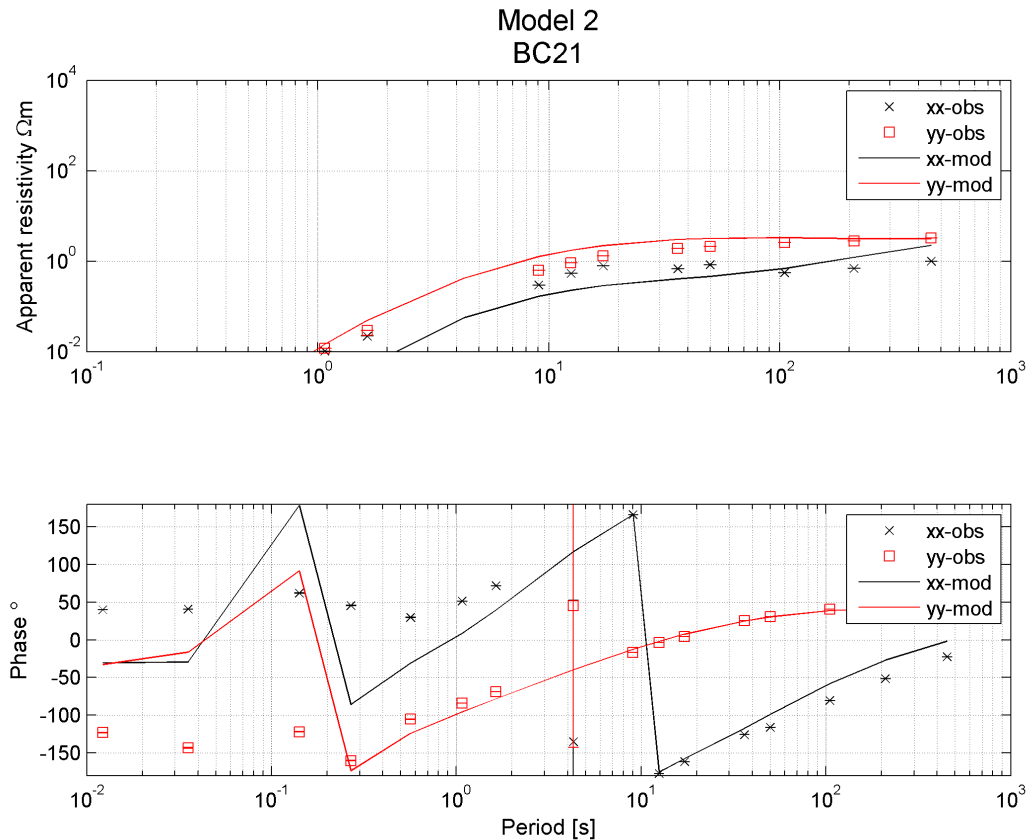
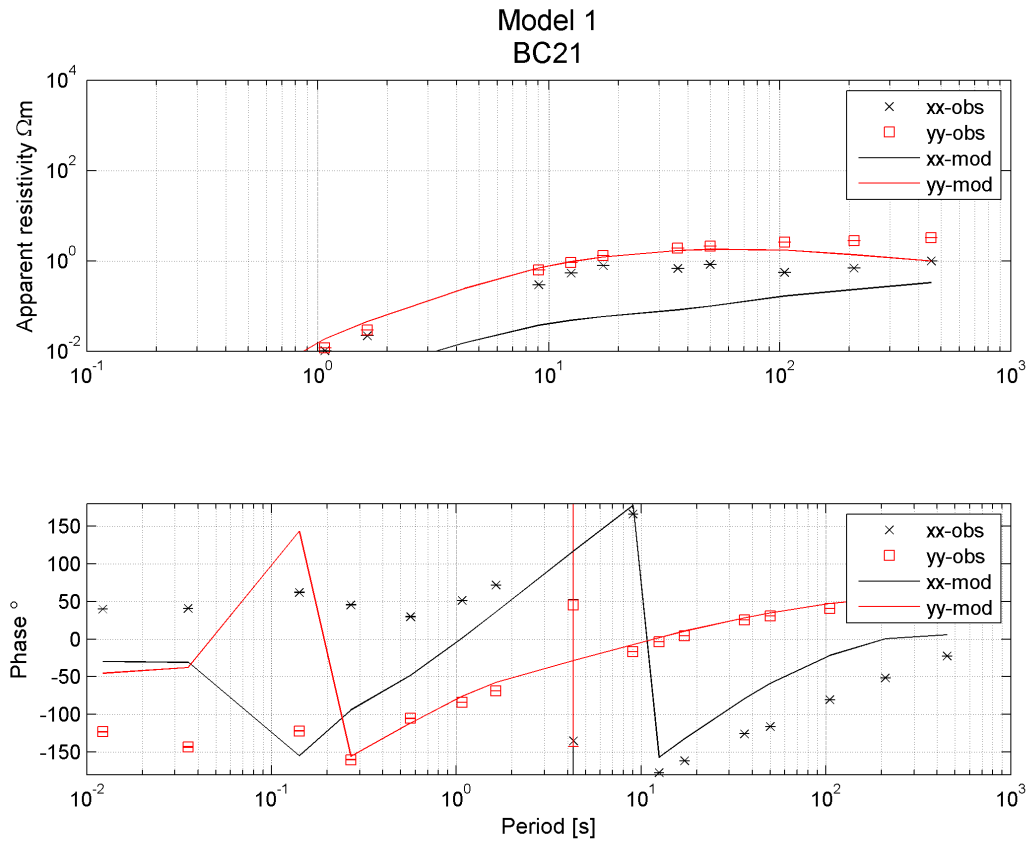


Model 1
BC21

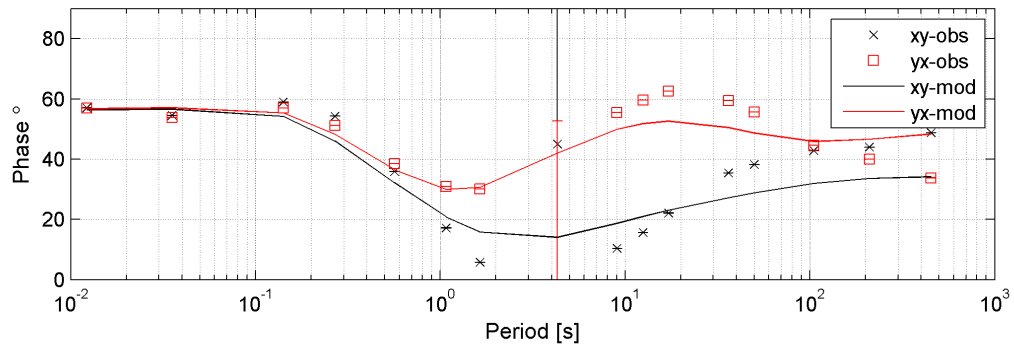
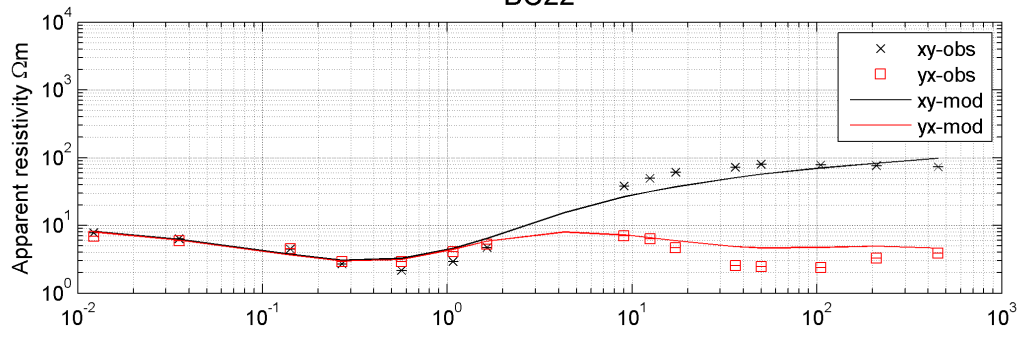


Model 2
BC21

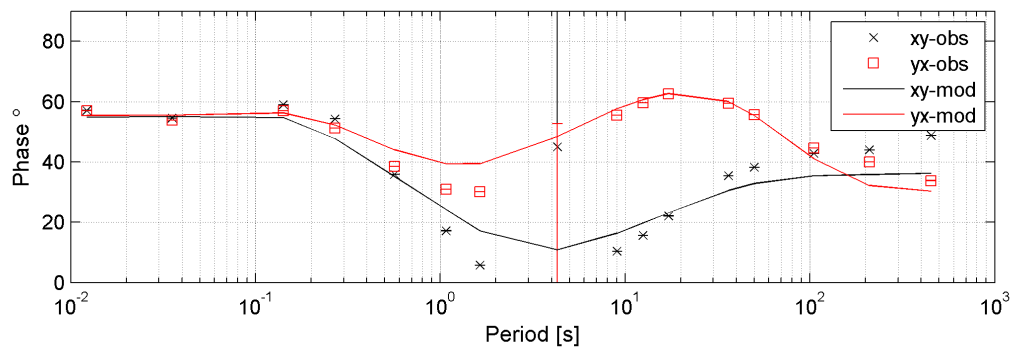
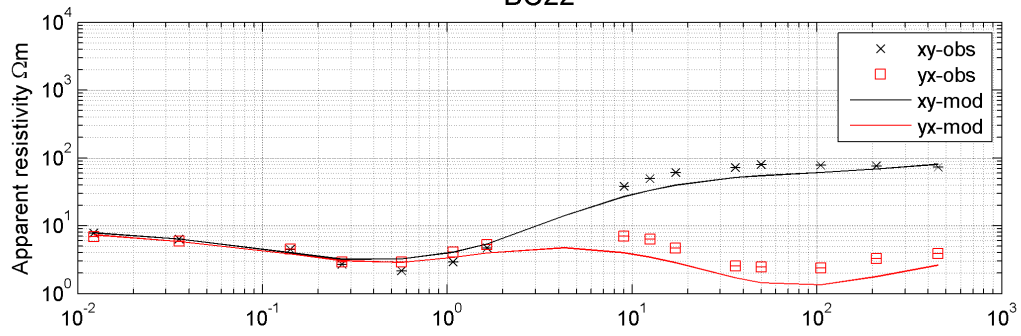


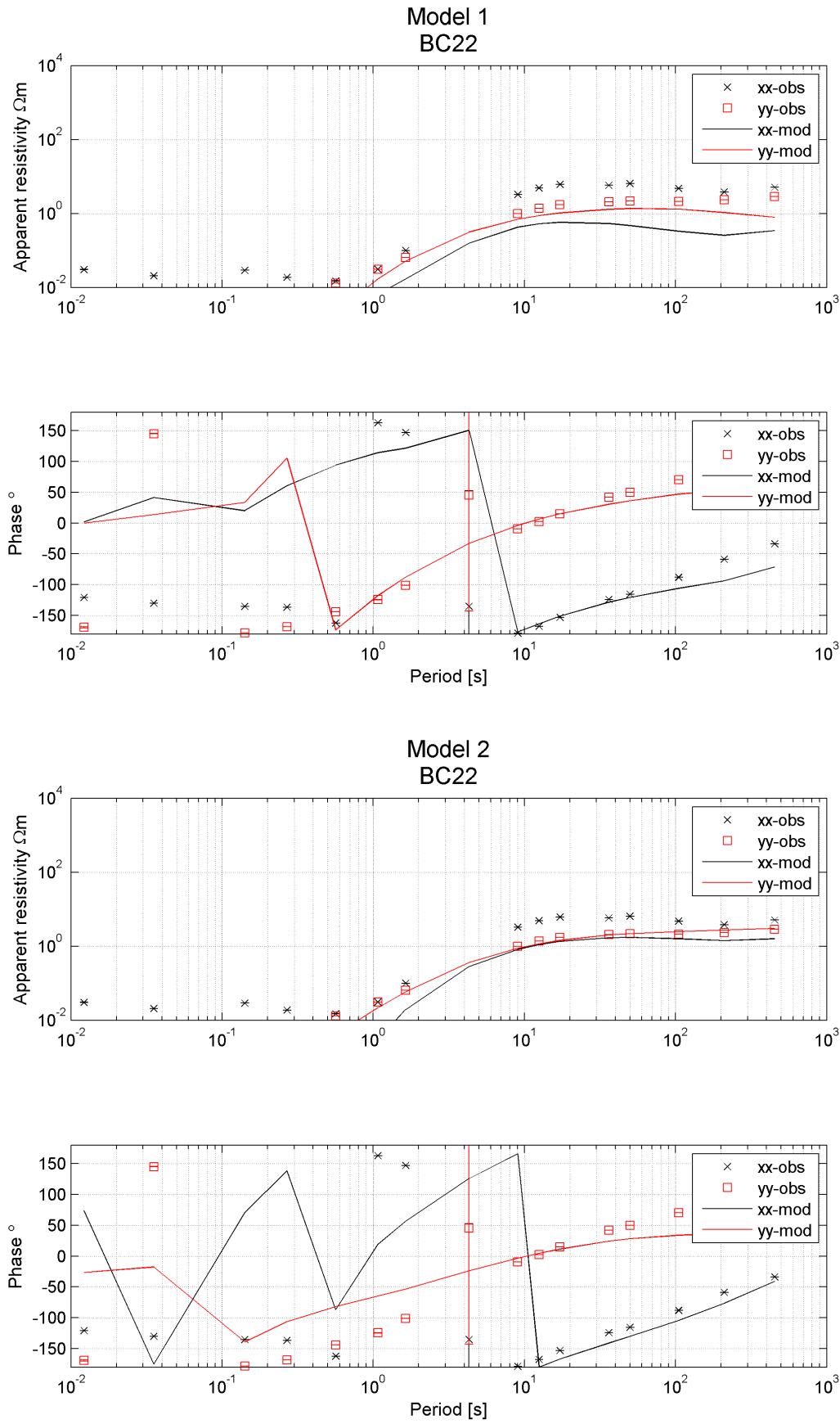


Model 1
BC22

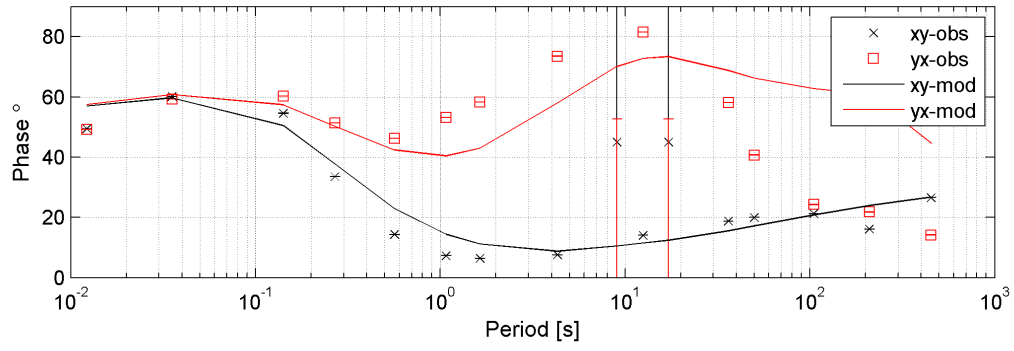
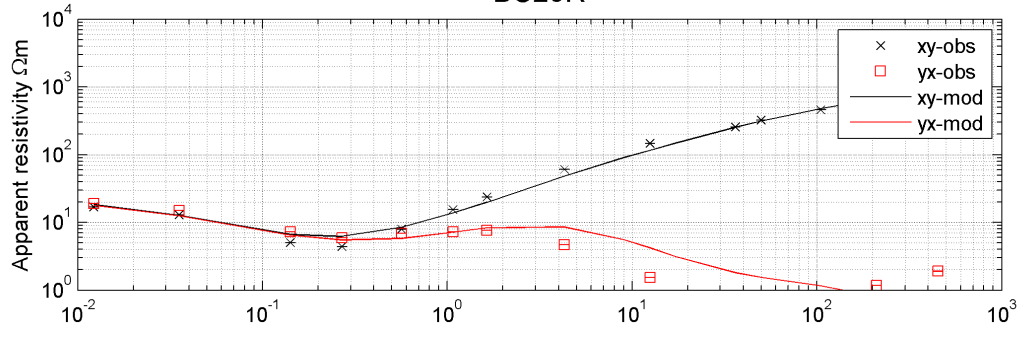


Model 2
BC22

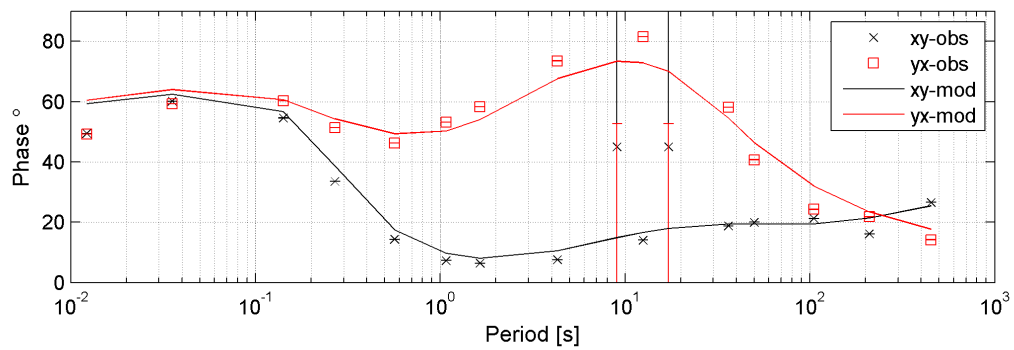
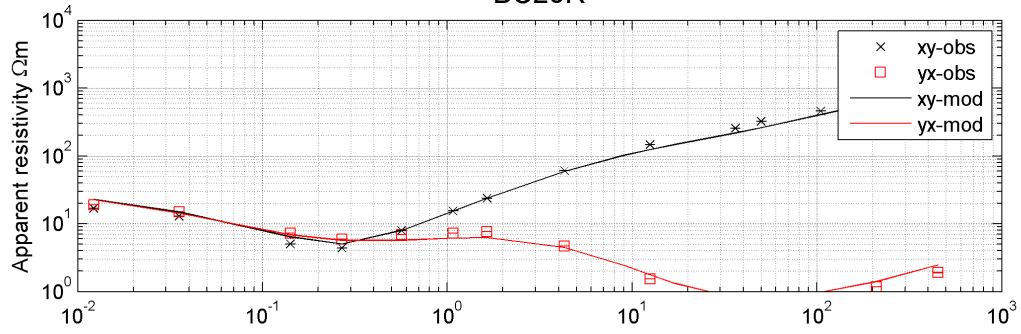


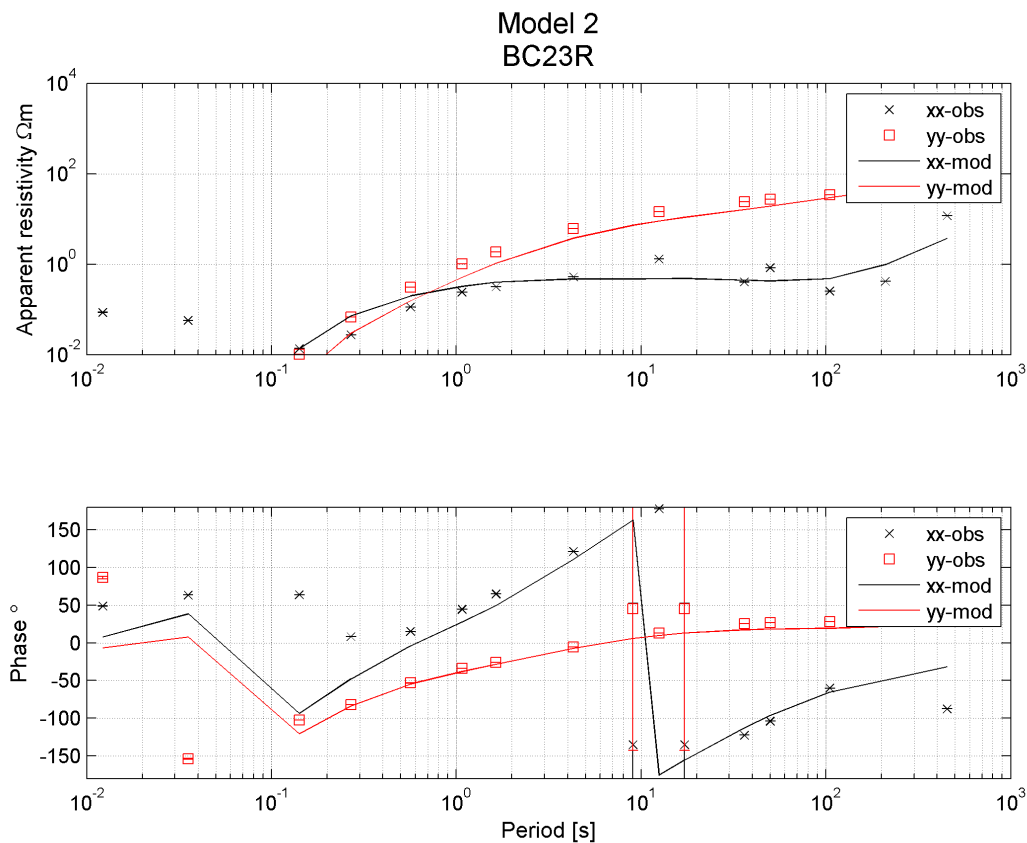
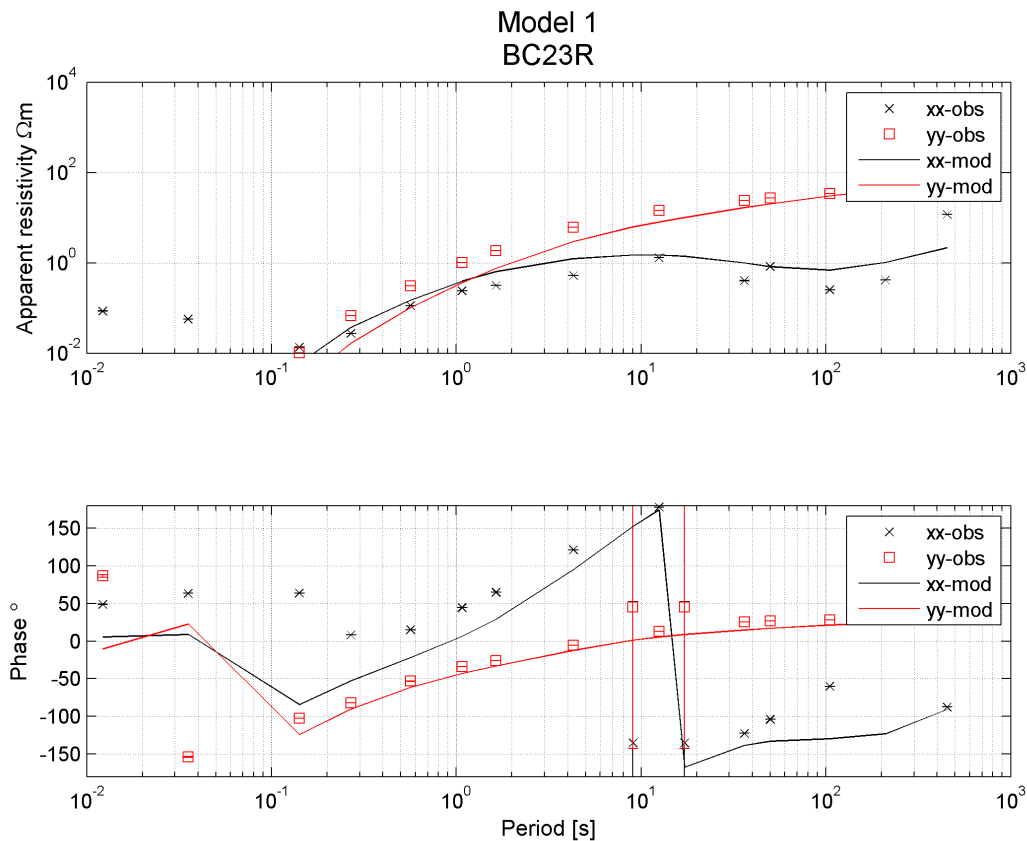


Model 1
BC23R

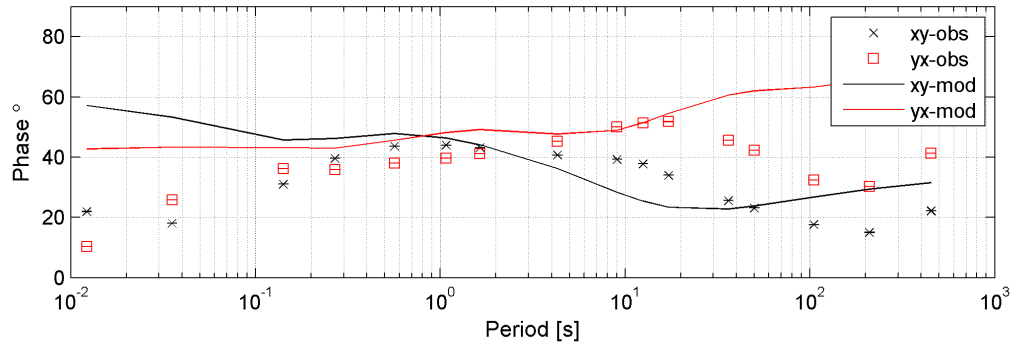
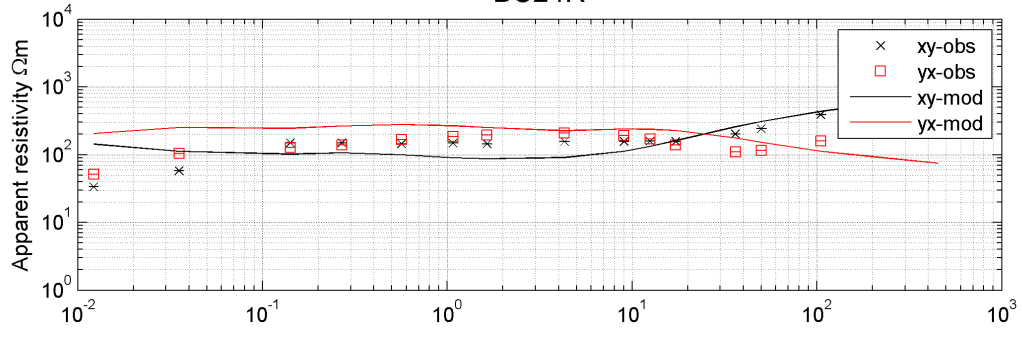


Model 2
BC23R





Model 1
BC24R



Model 2
BC24R

